Organizing Committee

Honorary Chair:
Prof. Si-Chen Lee, President, National Taiwan University, Taiwan

General Chair:
Prof. Satoshi Kawata, Executive director, Photonics Advanced Research Center, Osaka University, Japan
Prof. Ching-Fuh Lin, Chairman, Graduate Institute of Photonics and Optoelectronics, National Taiwan University, Taiwan

Conference Secretary:
Prof. Chih-I Wu, Vice Chairman , Graduate Institute of Photonics and Optoelectronics, National Taiwan University, Taiwan

Publicity:
Graduate Institute of Photonics and Optoelectronics,
National Taiwan University, Taiwan

Finance:
College of Electrical Engineering and Compute Science,
National Taiwan University, Taiwan
Osaka University, Japan
JSPS Asian CORE Program
Instrument Technology Research Center, Taiwan

Session Chairs:
1. Prof. Ching-Fuh Lin, Chairman, Graduate Institute of Photonics and Optoelectronics, National Taiwan University, Taiwan
2. Prof. Chau-Hwang Lee, Chairman, Institute of Biophotonics, National Yang-Ming University, Taiwan
3. Prof. Tien-Chang Lu, Associate Professor, Department of Photonics, National Chiao Tung University, Taiwan
4. Prof. Ta-Jen Yen, Associate Professor, Director of Student Activities, National Tsing Hua University, Taiwan
5. Prof. Pei-Chen Yu, Associate Professor, Department of Photonics, National Chiao Tung University, Taiwan
6. Prof. Hao-Chung Kuo, Professor, Department of Photonics, National Chiao Tung University, Taiwan
7. Dr. Pei-Kuen Wei, Associate Research Fellow, Research Center for Applied Sciences, Academia Sinica, Taiwan

日 程 表 Program

Day 1 〔January 11, 2012〕

09:30-09:45	報 到 Registration
10:00-10:15	開幕及致詞 Opening ceremony
10:15-11:00	**Nanophotonics and plasmonics** 演講人:日本大阪大學前瞻光電研究中心 Prof. Satoshi Kawata 河田 聡 教授 主持人:國立臺灣大學光電工程學研究所 林清富 所長
11:00-11:45	**Functionalized Arrays of Raman-Enhancing Nanoparticles for Capture and Culture-Free Analysis of Bacteria in Human Blood** 演講人:中央研究院原子與分子科學研究所 Prof. Yuh-Lin Wang 王玉麟 博士 主持人:國立臺灣大學光電工程學研究所 林清富 所長
11:45-13:30	午 餐 Lunch Break
13:30-13:50	**Enhanced Near-Field Interaction between Surface Plasmon Polaritons and Longitudinal Nanoacoustic Pulses** 演講人:臺大電機資訊學院 孫啟光 副院長 Prof. Chi-Kuang Sun 主持人:國立陽明大學生醫光電工程研究所 李超煌 所長
13:50-14:10	**Organic Thin-Film Solar Cells Utilizing Discotic Liquid Crystalline Phthalocyanine** 演講人:日本大阪大學 Prof. Akihiko Fujii 藤井 彰彥 副教授 主持人:國立陽明大學生醫光電工程研究所 李超煌 所長
14:10-14:30	**A few works in enhanced Raman scattering** 演講人:國立臺灣大學凝態科學研究中心 王俊凱 博士 Prof. Juen-Kai Wang 主持人:國立陽明大學生醫光電工程研究所 李超煌 所長
14:30-14:50	**Compact plasmonic resonators** 演講人:日本德島大學 Prof. Masanobu Haraguchi 原口 雅宣 教授 主持人:國立交通大學光電工程學系 盧廷昌 副教授
14:50-15:10	**Design, Synthesis and Biological Application of in Vivo Imaging Probes with Tunable Chemical Switches** 演講人:日本大阪大學 Prof. Kazuya Kikuchi 菊地 和也 教授 主持人:國立交通大學光電工程學系 盧廷昌 副教授
15:10-15:30	**Plasmonic Effects on the Optical Properties of Metal-Insulator-Metal Structures** 演講人:日本神戶大學 Prof. Shinji Hayashi 林 真至 教授 主持人:國立交通大學光電工程學系 盧廷昌 副教授

Day 2 〔January 12, 2012〕

09:30-09:45	報 到 Registration
10:00-10:20	**Lateral Superfocusingof Surface Plasmon Polariton in Symmetric Slab Plasmonic Waveguides** 演講人: 日本大阪大學 Prof. Junichi Takahara 高原 淳一 教授 主持人:國立清華大學材料科學工程學系 嚴大任 副教授 國立交通大學光電工程學系 余沛慈 副教授
10:20-10:40	The radiative lifetime dispersion and gain coefficient analysis of Silicon quantum dots-based optical waveguide amplifier 演講人:國立臺灣大學光電工程學研究所 林恭如 教授 Prof. Gong-Ru Lin 主持人:國立清華大學材料科學工程學系 嚴大任 副教授 國立交通大學光電工程學系 余沛慈 副教授
10:40-11:00	**Nanoplasmonic and electrochemical biosensors for medical diagnosis and cellular analyses** 演講人: 日本大阪大學 Prof. Eiichi Tamiya 民谷 栄一 教授 主持人:國立清華大學材料科學工程學系 嚴大任 副教授 國立交通大學光電工程學系 余沛慈 副教授
11:00-11:20	**Nanoscale Photon Management for Efficient Photovoltaic Energy Harvesting** 演講人：國立臺灣大學光電工程學研究所 何志浩 副教授 Prof. Jr-Hau He 主持人:國立清華大學材料科學工程學系 嚴大任 副教授 國立交通大學光電工程學系 余沛慈 副教授
11:20-11:40	**Nano-spectroscopy with plasmonic antennas** 演講人: 日本大阪大學 Prof. Prabhat Verma 教授 主持人:國立清華大學材料科學工程學系 嚴大任 副教授 國立交通大學光電工程學系 余沛慈 副教授
11:40-12:00	**Instrumentation for Healthcare and Better Life** 演講人：國研院儀科中心 陳峰志 副主任 Prof. Fong-Zhi Chen 主持人:國立清華大學材料科學工程學系 嚴大任 副教授 國立交通大學光電工程學系 余沛慈 副教授
12:00-14:00	午 餐 Lunch Break
14:00-14:20	**Polymeric Light Emitting Diodes and Transistors Utilizing Poly(alkylfluorene) Derivatives** 演講人:日本大阪大學 Prof. Yutaka Ohmori 大森 裕 教授 主持人:國立交通大學光電工程學系 郭浩中 教授 中研院應科中心力學專題中心 魏培坤 代理執行長
14:20-14:40	**Modeling and Analysis of Optical Transmission and Reflection of Double Nano-silt Metallic Gratings** 演講人：國立臺灣大學光電工程學研究所 黃鼎偉 助理教授 Prof. Ding-Wei Huang 主持人:國立交通大學光電工程學系 郭浩中 教授 中研院應科中心力學專題中心 魏培坤 代理執行長

15:30-15:45	休息時間 Coffee Break
15:45-17:30	Poster session
17:45-21:00	Evening banquet

End of Day 1

14:40-15:00	**Logic gate and shift register with magnetic quantum dots cellular automata** 演講人:日本大阪大學 Prof. Hikaru Nomura 野村 光 教授 主持人:國立交通大學光電工程學系 郭浩中 教授 中研院應科中心力學專題中心 魏培坤 代理執行長
15:00-15:20	**Metamaterials with Multiple Plasmonic Resonances towards Complex Optical Functionalities** 演講人：國立清華大學材料科學工程學系 嚴大任 副教授 Prof. Ta-Jen Yen 主持人:國立交通大學光電工程學系 郭浩中 教授 中研院應科中心力學專題中心 魏培坤 代理執行長
15:20-15:40	**Self-organized assembly of metal nanostructures for three-dimensional metamaterials** 演講人:日本理化學研究所高級助理研究員 Prof. Takuo Tanaka 田中 拓男 博士 主持人:國立交通大學光電工程學系 郭浩中 教授 中研院應科中心力學專題中心 魏培坤 代理執行長
15:40-16:00	**Microcavity Laser with Efficient Data Transmission** 演講人：國立臺灣大學光電工程學研究所 吳肇欣 助理教授 Prof. Chao-Hsin Wu 主持人:國立交通大學光電工程學系 郭浩中 教授 中研院應科中心力學專題中心 魏培坤 代理執行長
16:00-16:15	休息時間 Coffee Break
16:15-17:15	Panel discussion
17:15-17:30	Closing ceremony
17:45-21:00	Evening banquet

End of Day 2

Barry Lam Hall - 1F

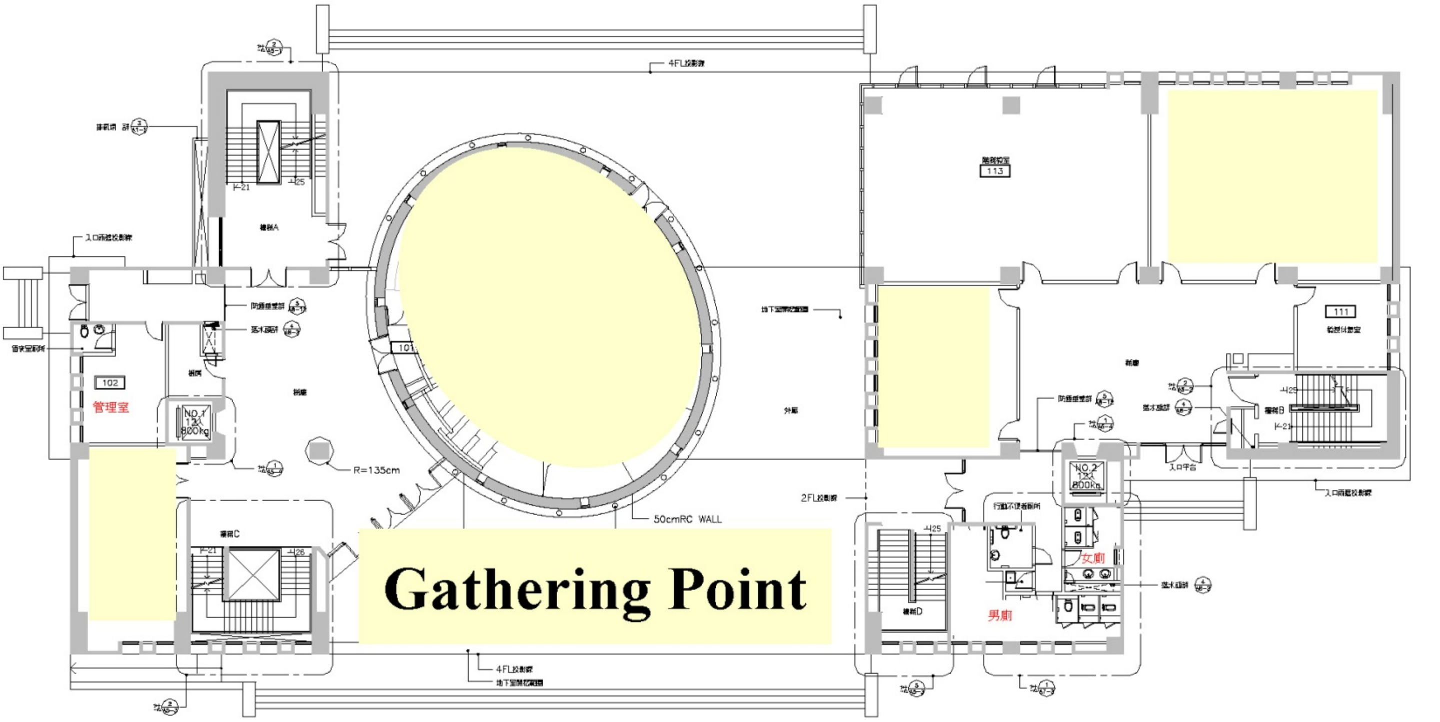

Barry Lam Hall - 2F

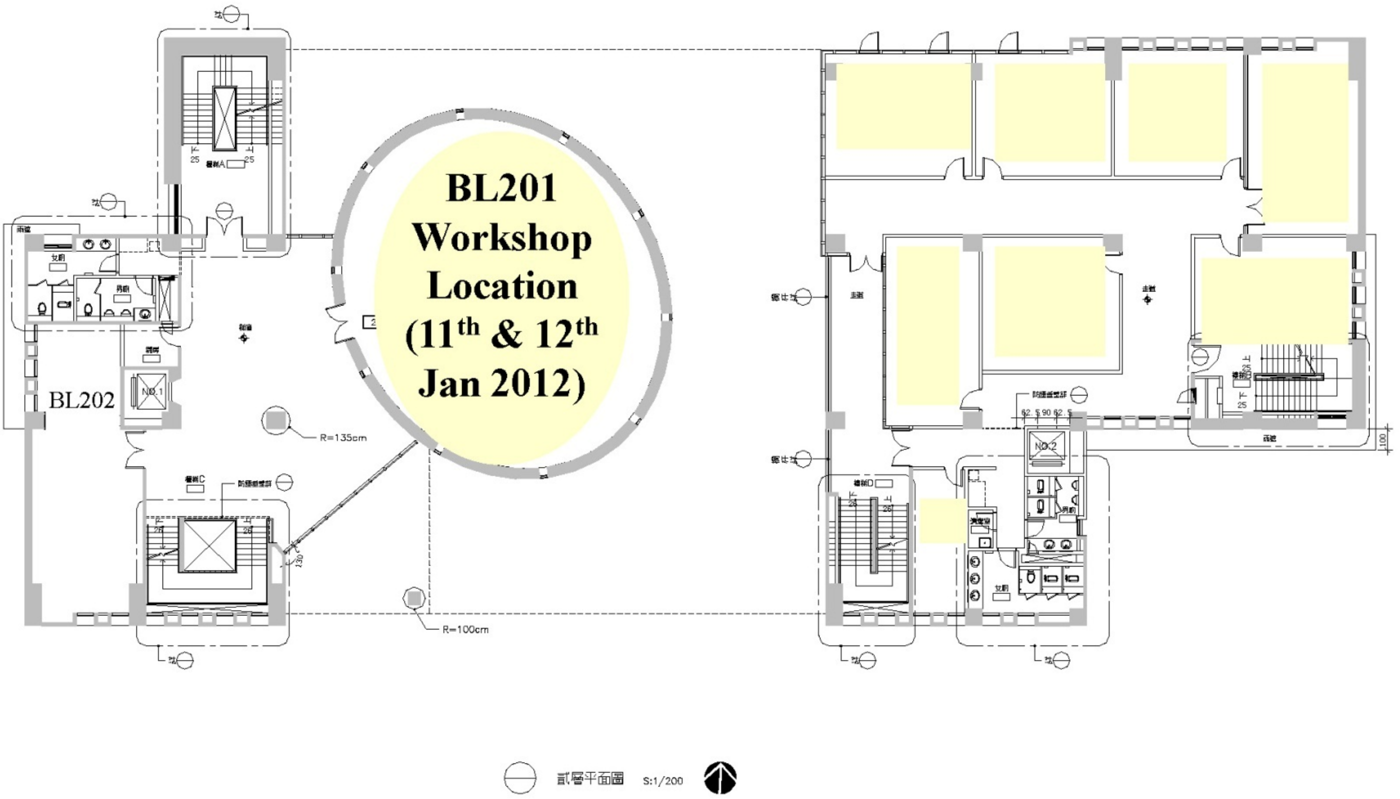

Barry Lam Hall - 3F

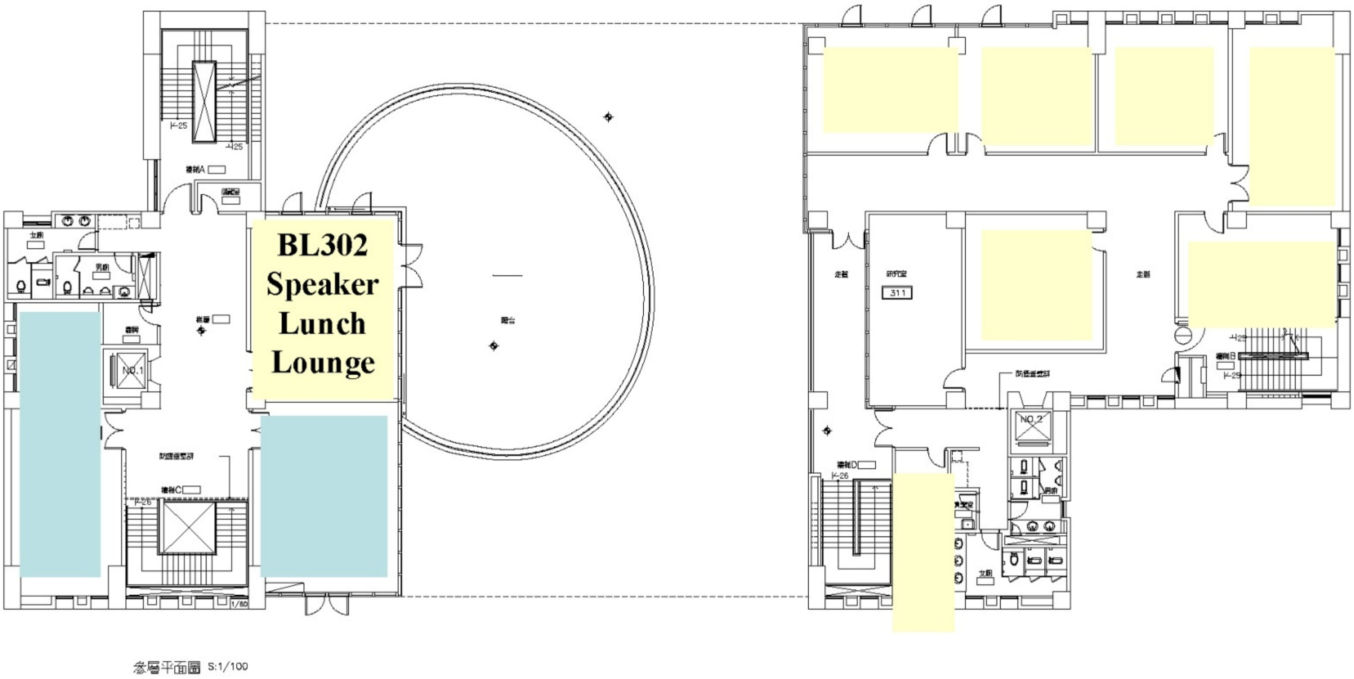

Barry Lam Hall - B1

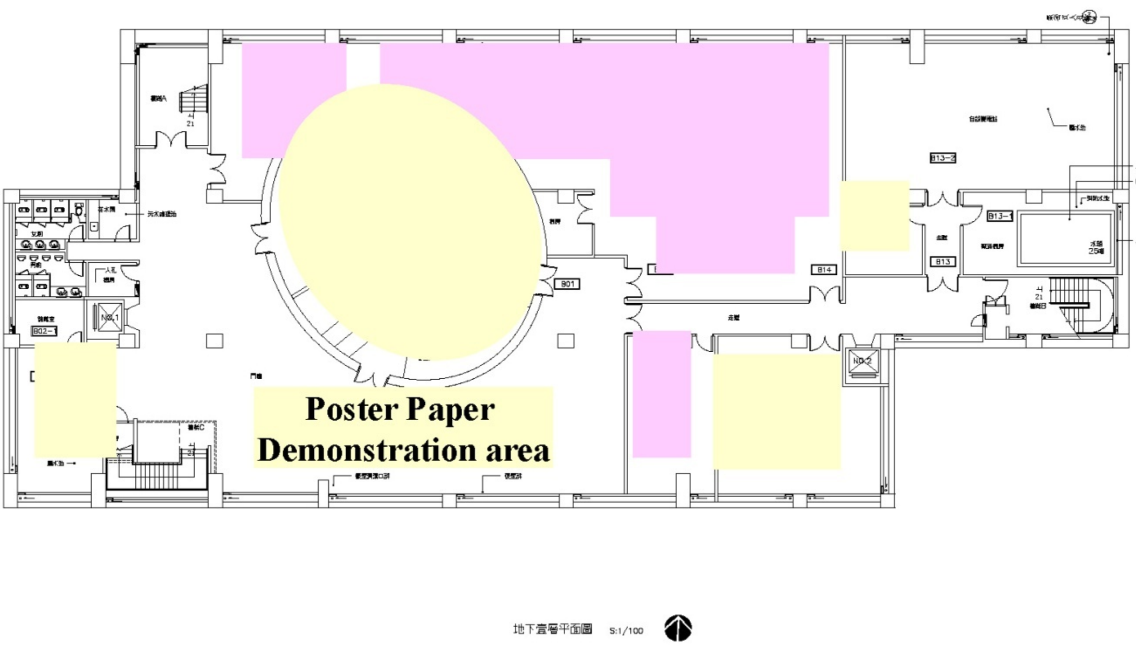

NTU MAIN CAMPUS MAP
國立臺灣大學
校總區地圖
2011/10/24
N
Barry Lam Hall〔博理館〕
Workshop Location
Leader Hotel Taipei〔立德台大尊賢會館〕
TEL: (02) 8369-2858
Web: http://www.leaderhotel.com/taipei/
Address:台北市大安區羅斯福路四段83號
往大安森林公園
To Da-an Park
往捷運古亭站
To GuTing Metro Station
往臺北車站
To Taipei Main Station
往世貿中心/捷運六張犁站
To World Trade Center / LiuZhangLi Metro Station
往捷運麟光站
To Linguang Metro Station
往新店
To XinDian
建國南路三段
JianGuo S. Rd. Sec. 3
新生南路三段
XinSheng S. Rd. Sec.3
辛亥路二段
XinHai Rd. Sec. 2
辛亥路三段
XinHai Rd. Sec. 3
羅斯福路四段
Roosevelt Rd. Sec.4
基隆路四段
KeeLung Rd. Sec.4
基隆路三段
KeeLung Rd. Sec.3
汀州路
TingZhou Rd.
思源街
SiYuan St.
長興街
ChangXing St.
芳蘭路
FangLan Rd.
椰林大道
Royal Palm Blvd.
醉月湖
Drunken Moon Lake
運動場
Sports Field
綜合體育館
Sports Center
圖書館
Main Library
傅鐘
Fu Bell
大學廣場
The University Promenade
捷運公館站
GongGuan Metro Station
銘傳國小
MingChuan Elementary School
水源市場
ShuiYuan Market
水源校區
ShuiYuan Campus
自來水園區
Taipei Water Park
臺灣科技大學
National Taiwan University of Science and Technology
台電
Tai Power
農業試驗場
Agricultural Experimental Farm
瑠公圳水源池
Liugongjun Pool
園藝分場
Horticultural Farm
尊賢館
Tsun Hsien Hall
博理館
Barry Lam Hall
鹿鳴廣場
Lu Ming Square
自行車拖吊保管場
Bicycle Pound
出入口(車輛可行駛)
Vehicle Exit
出入口(僅供行人與自行車通過)
Pedestrian/ Bicycle Exit
0 25 50 100 150 200 250 300 350 400 450 500 公尺

Nanophotonics and plasmonics

Satoshi Kawata

Photonics Center and Department of Applied Physics, Osaka University, and Nanophotonics Laboratory, RIKEN, Japan
Email: Kawata@skawata.com

Photonics at nano-scale has given new dimensions to several aspects of nanoscience, such as nano-imaging, nano-analysis, nano-manipulation, and nano-function of several kinds of materials ranging from semiconductors to biomolecules. The interaction volume between light and sample is classically restricted by diffraction limit of light, which is about half of the wavelength of probing light. We have crossed this classical barrier in several nanophotonics technologies, such as in fabrication, in analysis and in imaging of samples at nanoscale, and have shown how light can be manipulated to interact with materials in a volume much smaller than the diffraction limits. In particular, we use surface plasmons localized on the surface of nanostructured metal. I will review the sceince of nanophotonics and the mechanism and functions of plasmonics for going beyond the limit in conventional photonics.

(1) S. Kawata, H-B. Sun, T. Tanaka, K. Takada, Nature, 417, 697, 2001.
(2) S. Kawata, Y. Inouye, P. Verma, Nature Photonics, 3, 388, 2009
(3) S. Kawata, A. Ono, P. Verma, Nature Photonics, 2, 438, 2008,
(4) T. Yano, P. Verma, Y. Saito, T. Ichimura, Nature Photonics, 3, 473,, 2009.
(5) T. Okamoto, J. Simonen, S. Kawata, Phys. Rev. B. 77, 115425, 2008.
(6) M. Ozaki, J. Kato, S. Kawata, Science, 332, 218, 2011.
(7) J. Ando, K. Fujita, N. Smitu, S. Kawata, Nano Letters, 11, 5344, 2011.
(8) M. Okada, N. Smith, M. Sodeoka, A. Palonpon, H. Endo, S. Kawata, K. Fujita, PNAS, in press, 2012.

Functionalized Arrays of Raman-Enhancing Nanoparticles for Capture and Culture-Free Analysis of Bacteria in Human Blood

Yuh-Lin Wang[1,2*], Ting-Yu Liu[1,3], Kun-Tong Tsai[1,4], Huai-Hsien Wang[1,2], Yu Chen[1], Yu-Hsuan Chen[1],

Yuan-Chun Chao[1], Hsuan-Hao Chang[1], Chi-Hung Lin[5], Juen-Kai Wang[1,6], and

1. *Institute of Atomic and Molecular Sciences, Academia Sinica P.O. Box 23-166, Taipei 10617, Taiwan*
2. *Department of Physics, National Taiwan University, Taipei, Taiwan*
3. *Institute of Polymer Science and Engineering, National Taiwan University, Taipei, Taiwan*
4. *Institute of Photonics and Optoelectronics, and Department of Electrical Engineering, National Taiwan University, Taipei, Taiwan*
5. *Institute of Microbiology and Immunology, School of Life Science, National Yang-Ming University, Taipei, Taiwan*
6. *Center for Condensed Matter Sciences, National Taiwan University, Taipei, Taiwan*

Detecting bacteria in clinical samples without the time-consuming culture process is most desired for rapid diagnosis. Such a culture-free detection needs to capture and analyze bacteria from a body fluid usually containing complicate constituents. Here we show that vancomycin (Van) coating of a special substrate with arrays of Ag-nanoparticles, which can provide label-free analysis of bacteria via surface enhanced Raman spectroscopy (SERS), leads to 1000 folds increase in its capability to capture bacteria without introducing significant spectral interference. Bacteria spiked in human blood can be concentrated onto a microscopic Van-coated area while blood cells are excluded. Furthermore, A Van-coated substrate provides distinctly different SERS spectra of Van-susceptible and Van-resistant *Enterococcus*, indicating its potential use for drug-resistance test. Our results represent a critical step towards the creation of SERS-based multifunctional biochips for rapid culture/label-free detection and drug-resistant testing of microorganisms in clinical samples.

(1). Liu, T. Y.; Tsai, K. T.; Wang, H. H.; Chen, Y.; Chen, Y. S.; Chao, Y. C.; Chang, H. H.; Lin, C. H.; Wang, J. K.; Wang, Y. L. Nat. Commun. **2011**, 2, 538.

Enhanced Near-Field Interaction between Surface Plasmon Polaritons and Longitudinal Nanoacoustic Pulses

Szu-Chi Yang,* Hui-Hsin Hsiao,* Hung-Ping Chen,* Pei-Kuen Wei,[§] Hung-Chun Chang,* and Chi-Kuang Sun*[§]

**Graduate Institute of Photonics and Optoelectronics, National Taiwan University, Taipei 106, Taiwan*
[§] Research Center for Applied Sciences, Academia Sinica, Taipei 115, Taiwan
Email: sun@ntu.edu.tw

In this paper we report that longitudinal nanoacoustic pulses[1] can efficiently modulate the coupling between surface plasmon polariton (SPP) and cavity mode (CM) field in nanogratings with a high frequency bandwidth. This finding was performed on gold nanogratings on top of a GaN crystal by combining a near-field scanning optical microscope (NSOM) with a femtosecond nanoultrasonic system. Our results indicate that the propagating longitudinal nanoacoustic pulses change the refractive index of GaN crystal and therefore modulate the near-field behavior of the cavity mode and the SPP mode in gold nanogratings. Due to the environmentally sensitivity of SPP, nanoacoustic pulses with a strain on the order of 10^{-4} can efficiently cause 45% extraordinary transmission modulation. Our finding suggests that temporal modulation with a 11.6 GHz bandwidth can be achieved by acousto-induced coupling change between CM and SPP mode, with a high potential for future spatial and high speed control of the SPP properties.

(1). Lin, K.-H.; Lai, C.-M.; Pan, C.-C.; Chyi, J.-I.; Shi, J.-W.; Sun, S.-Z.; Chang, C.-F.; Sun, C.-K. *Nature Nanotechnology* **2007**, *2*, 704-708.

Organic Thin-Film Solar Cells Utilizing Discotic Liquid Crystalline Phthalocyanine

Akihiko Fujii[1], **Kaoru Fukumura**[1], **Tetsuro Hori**[1], **Dao Quang Duy**[1], **Tetsuya Masuda**[1], **Takeshi Hayashi**[1], **Hiroyuki Yoshida**[1], **Fabien Nekelson**[1,2], **Yo Shimizu**[2], **and Masanori Ozaki**[1]

[1]*Graduate School of Engineering, Osaka University, Osaka 565-0871, Japan*
[2]*National Institute of Advanced Industrial Science and Technology, Osaka 563-8577, Japan*

Liquid crystalline organic semiconductor is one of the promising materials for electronic device applications, because of the potentially high carrier mobility comparable to that of a-Si (0.1 cm^2/Vs). Previously, we reported alkylphthalocyanine homologue exhibiting ambipolar characteristics with high drift mobility in both columnar mesogenic and crystalline phases.[1,2] Organic thin-film solar cells based on a bulk hetero-junction utilizing a non-peripherally alkyl-substituted phthalocyanine, such as, 1,4,8,11,15,18,22,25-octahexylphthalocyanine ($C6PcH_2$), must have a potential to achieve the high performance.

$C6PcH_2$ is a low-molecular-weight organic semiconductor and has high solubility for typical organic solvents due to the long substituents. $C6PcH_2$ exhibits liquid crystalline phase, such as, hexagonal disordered columnar mesophase between 161 and 170 °C. The blend uniform thin film with the $C6PcH_2$ and 1-(3-methoxy-carbonyl)-propyl-1-1-phenyl-(6,6)C61 (PCBM) could be fabricated by a spin-coating method. Solar cells with $C6PcH_2$:PCBM bulk hetero-junction active layer have demonstrated a high external quantum efficiency above 70% in the Q-band absorption region of $C6PcH_2$ and a high energy conversion efficiency of 3.1%.[3-5]

The photovoltaic properties of the solar cell with bulk heterojunction of $C6PcH_2$ and PCBM demonstrated the strong dependence of active layer thickness, and the optimized active layer thickness was clarified to be 120 nm. By inserting MoO_3 hole transport buffer layer between the positive electrode and active layer, the FF and energy conversion efficiency were improved to be 0.50 and 3.2%, respectively. The tandem organic thin-film solar cell has also been studied by utilizing active layer materials of $C6PcH_2$ and poly(3-hexylthiophene) and the interlayer of LiF/Al/MoO_3 structure, and a high V_{oc} of 1.27 V has been achieved.[4]

$C6PcH_2$ is available as a dopant for conventional organic thin-film solar cells with an bulk hetero-junction active layer composed of poly(3-hexylthiophene) (P3HT) and PCBM. The improvement of long-wavelength sensitivity in P3HT:PCBM bulk hetero-junction solar cells by doping $C6PcH_2$ has been succeeded.[6]

(1). Y. Miyake, Y. Shiraiwa, K. Okada, H. Monobe, T. Hori, N. Yamasaki, H. Yoshida, M. J. Cook, A. Fujii, M. Ozaki and Y. Shimizu, *Appl. Phys. Express*, **2011**, *4*, 021604.

(2). Y. Shimizu, Y. Miyake, H. Yoshida, H. Monobe, M. J. Cook, A. Fujii and M. Ozaki, *Mol. Cryst. & Liq. Cryst.*, **2011**, *549*, 127-132.

(3). T. Hori, Y. Miyake, N. Yamasaki, H. Yoshida, A. Fujii, Y. Shimizu and M. Ozaki, *Appl. Phys. Express*, **2010**, *3*, 101602.

(4). T. Hori, N. Fukuoka, T. Masuda, Y. Miyake, H.Yoshida, A. Fujii, Y. Shimizu and M. Ozaki, *Solar Energy Materials and Solar Cells*, **2011**, *95*, 3087-3092.

(5). T. Hori, T. Masuda, N. Fukuoka, Y. Miyake, T. Hayashi, T. Kamikado, H.Yoshida, A. Fujii, Y. Shimizu and M. Ozaki, to be published in *Organic Electronics*.

(6). T. Hori, Y. Miyake, T. Masuda, T. Hayashi, K. Fukumura, H.Yoshida, A. Fujii, Y. Shimizu and M. Ozaki, to be published in *Journal of Photonics for Energy*.

A few works in enhanced Raman scattering

Juen-Kai Wang

Center for Condensed Matter Sciences, National Taiwan University and Institute of Atomic and Molecular Sciences, Academia Sinica, Taipei 106, Taiwan
Email: jkwang@ntu.edu.tw

Surface-enhanced Raman scattering (SERS) has been attractive in past three decades, because it provides potential to detect chemical and biological traces. In particular, a type of SERS-active substrate with uniformly large and highly reproducible Raman-enhancing power has been developed by growing Ag nanoparticles on arrays of anodic aluminum oxide nanochannels to take advantage of the 'hot-junctions' created by plasmon coupling at sub-10 nm interparticle gaps.[1] With such substrate, SERS of various types of bacteria have been acquired and the response of bacteria to antibiotics has been examined.[2,3] Such successful demonstration greatly relies on the understanding and controlling the two enhancement mechanisms (electromagnetic and chemical enhancements). In this talk, a simple quasi-static dipole coupling model is presented to interpret far-field optical properties of such substrate;[4,5] a high-precision calculation confers near-field traits of these hot junctions.[6] In addition, based on concurrent measurements of enhanced Raman scattering and photoluminescence, an approach is proposed to determine the enhancement factors of both mechanisms[7] and a molecular ruler is demonstrated.[8] Finally, the electron-mediated chemical enhancement mechanism is investigated on inorganic semiconductors.[9] These studies represent our continual endeavors in scrutinizing the fundamental aspects of enhanced Raman scattering.

(1). Wang, H.-H. et al. *Adv. Mater.* **2006**, *18*, 491.
(2). Liu, T.-T. et al. *PLoS ONE* **2009**, *4*, e5470.
(3). Liu, T.-Y. et al. *Nature Commun.* **2011**, *2*, 538.
(4). Birin, S. et al. *Opt. Express* **2008**, *16*, 15312.
(5). Chan, S. H. et al. *Phys. Sol. Stat. RRL* **2010**, *4*, 259.
(6). Lin, B.-Y. et al. *Opt. Express* **2009**, *17*, 14211.
(7). Dvoynenko, M. M.; Wang, J.-K. Opt. Lett. **2007**, *32*, 3552.
(8). Dvoynenko, M. M. et al. Opt. Lett. **2010**, *35*, 3808.
(9). Liu, C. Y. et al. *Appl. Phys. Lett.* **2010**, *96*, 033109.

Self-organized assembly of metal nanostructures for three-dimensional metamaterials

Takuo Tanaka

[1]RIKEN Metamaterials Laboratory, 2-1 Hirosawa, Wako, Saitama 351-0198 JAPAN

[2] Hokkaido University, Research Institute for Electronic Science

Email: t-tanaka@riken.jp

Metamaterial is an artificially designed material that consists of metal resonator array. Designing resonator array structure so that it is smaller than the wavelength of the light, metamaterials work as a homogeneous material whose electromagnetic properties inherited from its structure. By engineering such materials, we can design and control their magnetic permeability even in the optical frequency region in which all materials in nature lose magnetic response and their relative permeability is fixed at unity. Although many research results about metamaterials have been reported one after another, producing three-dimensional metamaterials is still difficult, thus there is no demonstration of complete 3D metamaterials.

Metamaterial's controllability of magnetic permeability is originated from tiny resonators embedded in a medium (Figure 1). We have investigated the design principle of 3D metamaterials that works in the visible light region[1-3]. The shape of each resonator is metal ring with several cuts, which is termed as split ring resonator (SRR), and its feature size of each resonator is in the range of 1/4 ~ 1/10 of target wavelength. Numerous numbers of such resonators should be embedded in a host medium. To meet these severe structural requirements, we devised a bottom-up approach that forms metal nanoparticle ring structure with the aid of external magnetic field. When an external magnetic field is applied to a mixture of paramagnetic beads and gold microspheres dispersed in ferrofluid, paramagnetic beads instantly align their magnetic moment to the direction of the external magnetic field, and gold microspheres gather around an equator of paramagnetic beads to form a ring structure as shown in Figure 2. This gold ring structure is identical to SRR. Using this self-organizing feature, we realize a three-dimensional metamaterial structure just by applying an external magnetic field. Moreover, the assembled ring structures are immediately disassembled, when an external magnetic field is eliminated. We can apply this feature for realizing an active metamaterial just by switching on/off an external magnetic field.

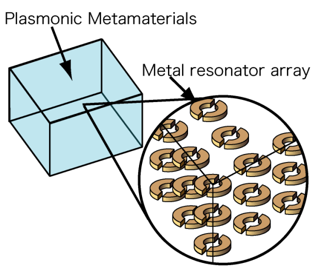

Fig. 1 Metamaterials

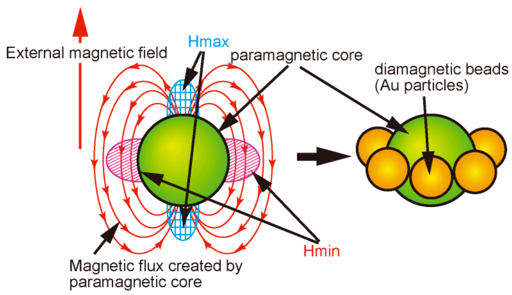

Fig. 2 Magnetic assembly of metal ring structures

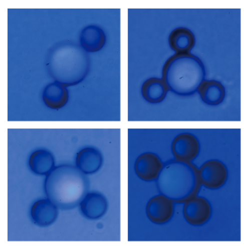

Fig. 3 Experimental results

(1) A. Ishikawa, T. Tanaka, and S. Kawata, Phys. Rev. Lett. **95**, 237401 (2005).

(2) A. Ishikawa and T. Tanaka, Opt. Commun. **258**, pp. 300-305 (2006).

(3) A. Ishikawa, T. Tanaka, and S. Kawata, J. Opt. Soc. Am. B **24**, 3, pp. 510-515 (2007).

Design, Synthesis and Biological Application of in Vivo Imaging Probes with Tunable Chemical Switches

__Kazuya Kikuchi__

Graduate School of Engineering, Osaka University, Suita 565-0871, Japan
Email: kkikuchi@mls.eng.osaka-u.ac.jp

One of the great challenges in the post-genome era is to clarify the biological significance of intracellular molecules directly in living cells. If we can visualize a molecule in action, it is possible to acquire biological information, which is unavailable if we deal with cell homogenates. One possible approach is to design and synthesize chemical probes that can convert biological information to optical output.

Protein fluorescent labeling provides an attractive approach to study the localization and function of proteins in living cells. Recently, a specific pair of a protein tag and its ligand has been utilized to visualize a protein of interest (POI). In this method, a POI is fused with a protein tag and the tag is labeled with the ligand connected to a fluorescent molecule. The advantage of this protein labeling system is that a variety of fluorescent molecules are potentially available as labeling reagents, and that the protein tag is conditionally labeled with its fluorescent ligand. However, in the existing labeling systems, there are some problems with the size of a protein tag, the specificity of the labeling or fluorogenicity of labeling reagents. Protein tags for labeling proteins of interest (POIs) with small molecule based probes have become important technique as practical alternatives to the fluorescent proteins (FPs) for live cell imaging. We have designed a protein labeling system that allows fluorophores to be linked to POI. The protein tag (BL-tag) is a mutant class A β-lactamase (TEM-1) modified to be covalently bound to the designed specific labeling probes and the labeling probes is consisted with a β-lactam ring (ampicillin, cephalosporin) attached to various fluorophores. A fluorogenetic labeling system can be designed using the unique property of cephalosporin, which release leaving group by subsequent reaction after opening the lactam ring. For further sophisticated application, multicolor imaging was done by adopting the colorful fluorophores.[1,2,3]

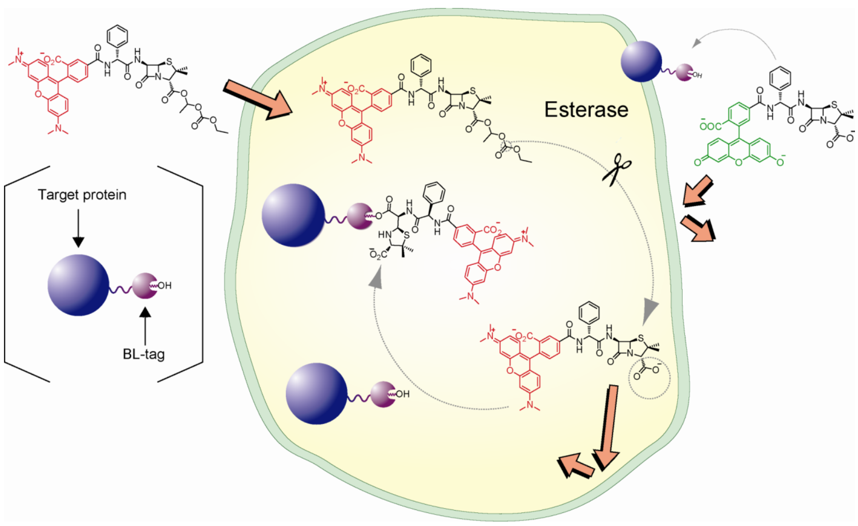

(1). Mizukami, S.; Watanabe, S.; Akimoto, Y.; Kikuchi, K. *J. Am. Chem. Soc.* **2012**, *134*, in press.
(2). Mizukami, S.; Yamamoto, T.; Yoshimura, A.; Watanabe, S.; Kikuchi, K. *Angew. Chem. Int. Ed.* **2011**, *50,* 8750-8752.
(3). Mizukami, S.; Watanabe, S.; Hori, Y.; Kikuchi, K. *J. Am. Chem. Soc.***2009**, *131*, 5016-5017.

Plasmonic Effects on the Optical Properties of Metal-Insulator-Metal Structures

Shinji Hayashi

Department of Electrical and Electronic Engineering, Graduate School of Engineering, Kobe University, 657-8501 Rokko, Nada, Kobe, Japan
Email: hayashi@eedept.kobe-u.ac.jp

Recently, structures consisting of an insulator layer sandwiched by metal layers, i.e., metal-insulator-metal (MIM) structures, have attracted much interest because of their peculiar optical properties. When the insulator layer is thin enough, coupling of the surface plasmon polariton (SPP) modes at the two interfaces results in the symmetric and antisymmetric SPP mode. Figure 1 shows the dispersion curves of these SPP modes (TM modes) as well as the TE_0 mode for a Ag (infinite)/MgF_2 (135 nm thick)/Ag (infinite) structure. It should be noted that the dispersion curve of the symmetric mode is extended to the radiative region and consequently, this mode can interact with external light outside the MIM structure, provided that the metal layer is thin enough. The coupled SPP and TE_0 modes govern the optical properties of the MIM structures and lead to unique optical responses.

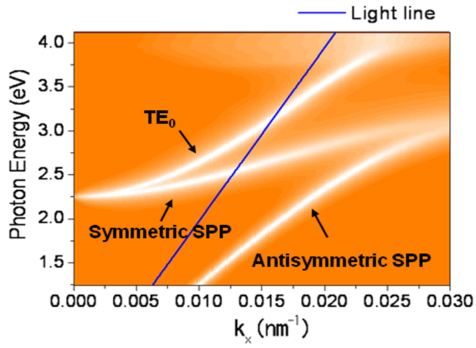

Fig.1 Dispersion curves of electromagnetic modes supported by an MIM structure

As an example, anomalous optical transmission through Ag (40 nm thick)/MgF_2 (varying thickness)/Ag (40 nm thick)/glass substrate structures is presented in Fig. 2. The transmittance of a 80-nm-thick Ag film deposited on a glass substrate is normally very low. However, the MIM structure with Ag films having the same total thickness exhibits sharp transmission peaks with high transmittance values. Furthermore, the peak wavelength can be tuned by changing the thickness of the insulator layer. Detailed analyses reveal that the light transmission through MIM is mediated by the symmetric SPP and TE_0 modes.

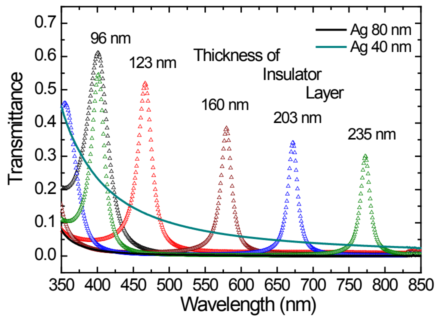

Fig.2 Anomalous light transmission through MIM structures for various insulator thicknesses.

In this contribution, we discuss the optical properties of MIM structures in which dye molecules are embedded in the insulator layers. Experimental and theoretical results on the following topics are presented:

1) Light emission from embedded dye molecules mediated by the SPP modes [1].
2) Strong coupling of excitons in dye molecules with the symmetric SPP and TE_0 modes.

Novel optical properties arising from the combination of the MIM structures and the dye molecules may find potential applications, for example, in light emitting devices and sensing devices.

[1]. S. Hayashi, A. Maekawa, Suk Chan Kim, and M. Fujii, "Mechanism of Enhanced Light Emission from an Emitting Layer Embedded in Metal-Insulator-Metal Structures", Phys. Rev. B, Vol. 82, 035441, pp. 1-6 (2010) .

Lateral Superfocusing of Surface Plasmon Polariton in Symmetric Slab Plasmonic Waveguides

Junichi Takahara[1,2] **and Masashi Miyata**[3]

1Photonics Advanced Research Center, Osaka University, Suita, Osaka, Japan
2Graduate School of Engineering, Osaka University, Suita, Osaka, Japan
3Graduate School of Engineering Science, Osaka University, Toyonaka, Osaka, Japan
Email: takahara@ap.eng.osaka-u.ac.jp

A plasmonic waveguide (PWG) is a metal optical waveguide that utilizes surface plasmon polariton (SPP) propagating at a metal-dielectric interface. The optical beam radius of SPP around a nano metal rod can be shurunk to the nanometer order beyond the diffraction limit of light [1-3]. We have reported lateral confinement, superfocusing and selective excitation of SRSP in metal gap PWGs [4-6].

Many types of PWG have been studied during 2000s [3]. A symmetric slab PWG (a thin metal film with finite width) is the most typical structure among planar PWGs. Though propagation modes in a slab PWG have been studied by Berini, their interests are mainly focused to long-range SPP mode (LRSP) towards active plasmonics [7,8]. For applications to nano-optical integrated circuits, further studies are needed for strongly confined mode called “short-range SPP mode (SRSP)” in planar type of PWG. In this presentation, we report recent progress of our study about tapered- and nano-symmetric slab PWGs.

Figure 1 shows FDTD simulated results for propagation of SPP in tapered symmetric slab PWG: LRSP or SRSP can be excited selectively by phase control method between two incident beams [6]. In the case of SRSP, mode field is guided along the edge of the slab and concentrated into the tip of the slab as shown in Fig. 1(b); this is superfocusing effect. On the other hand, LRSP shows (diffraction limited) broad focusing spot as shown in Fig. 1(a). Figure 2 shows experimental results for the silver slab PWG embedded in SiO_2. We will show numerical mode analysis in the slab PWG in detail and discuss the experimental results.

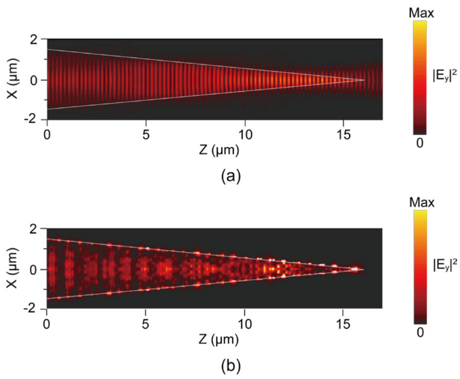

Fig. 1 Simulated electric field intensity in tapered slab PWGs: (a) selective excitation of LRSP and (b) SRSP.

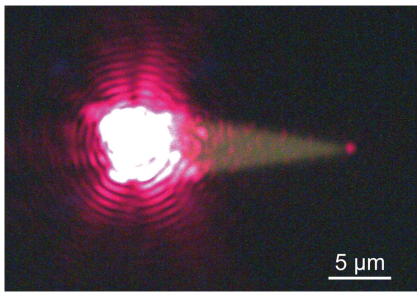

Fig. 2 Far field image from the tapered silver slab PWG embedded in SiO_2.

(1). J. Takahara, S. Yamagishi, H. Taki, A. Morimoto, T. Kobayashi: Opt. Lett., **1997,** 22, 475.
(2). J. Takahara and T. Kobayashi: Optics & Photonics News, **2004,** Vol.15, No.10, 54.
(3). J. Takahara: Plasmonic Nanoguides and Circuits, Ch.2, ed. S.I.Bozhevolnyi (PanStanford Publishing, **2009**) .
(4). F. Kusunoki, T. Yotsuya, J. Takahara and T. Kobayashi: Appl. Phys. Lett., **2005**, 86, 211101.
(5). J. Takahara and F. Kusunoki: IEICE Trans. Electron. E90-C, **2007**, 1, 87.
(6). K. Yamamoto, K. Kurihara, J. Takahara and A. Otomo: MRS Symp.Proc., **2009**, 1182-EE13-05, 55.
(7). P. Berini: Opt. Lett.: **1999**, 24, 15, 1011.
(8). P. Berini and I.De Leon: Nature Photonics, **2012**, 6, 16.

The radiative lifetime dispersion and gain coefficient analysis of Silicon quantum dots-based optical waveguide amplifier

Gong-Ru Lin* **and Chung-Lun Wu**

Graduate Institute of Photonics and Optoelectronics, and Department of Electrical Engineering, National Taiwan University, Taipei 106, Taiwan

Email: grlin@ntu.edu.tw

Si quantum dot (Si-QD) has emerged for active optical devices during past decades. Based on the quantum confinement effect, the energy gap of Si-QDs can be easily detuned (from 1.1 to ~3.3 eV) and the radiative recombination rate can be enhanced via the control on Si-QD size. Nonetheless, the coarse confinement on the Si-QD size inevitably leads to a dispersive distribution on characteristic parameters of the Si QDs. In this work, the Si-QD based multi-color strip-loaded waveguide amplifiers are characterized. The size distribution of the Si-QDs and its correlation with the luminescent lifetime dispersion are investigated by analyzing time-resolved photoluminescence (TRPL) with a pumped pulsewidth of 5 ns at 405 nm. The gain coefficient and emission cross-section area of Si-QD are determined by utilizing variable strip length (VSL) and maximum gain-length product analyses. The Si-QDs are synthesized by PECVD. The Si-rich SiO_x films with different composition ratios (defined as $R=N_O/N_{Si}$) can be obtained with varying fluence ratio of $[SiH_4]/[N_2O]$ and RF plasma power. After annealing, the Si-QDs with versatile sizes and distributions self-assemble in SiO_x films with different composition ratios can be obtained, in which three composition ratios (blue-ASE with R= 1.52 and $D_{Si\text{-}QD}$= 1.7 nm, yellow-ASE with R=1.42 and $D_{Si\text{-}QD}$= 2.8 nm, and red-ASE with R=1.24 and $D_{Si\text{-}QD}$= 4.4 nm) are discussed.

The PL peak wavelength and corresponding linewidth of Si-QDs luminescence for blue/yellow/red-ASE samples are 428/38, 649/147, and 764/127 nm. With the decrease on average size of Si-QDs from 4.4 to 1.7 nm, the PL color blue-shifts from red to blue due to the Si-QD size dependent quantum confinement effect. The simulation with combining finite potential-well approximation and the Fermi-golden rule are utilized to simulate the energy gap, electron-hole wave-function overlap, and zero-phonon assisted recombination rate of Si-QDs. Based on the finite potential well approximation, the bandgap diagram of Si-QD embedded in SiO_2 matrix has been demonstrated, and the relation between optical bandgap (E_g) and Si-QDs diameter (d) is deduced as $E_g(d)=1.12+5.83/d^{1.78}$ (eV). In comparison with larger Si-QD, the smaller Si-QD with blue emission is mainly attributed to enhanced probability of electron-hole pair wave-function overlap, in which the zero-phonon assisted recombination rate is greatly improved to result in the higher luminescence intensity. The full spectral TRPL fitted by the modified stretch exponential decay function is decomposed by three exponential decay functions including Si-QDs, NOV defect, and E'δ decaying mechanisms. The stretch exponential decay function for Si-QD related decay trace is described as $I(t) = I_{Si\text{-}QD}\exp(-t/\tau)^{\beta}$ with β denoting as the dispersion factor and $I_{Si\text{-}QDs}$ the intensity of Si-QD luminescence. The size distribution induced lifetime and dispersion factor of blue/yellow/red samples are 0.14μs/0.73, 0.97μs/0.39, and 6.3μs/0.62, respectively. The broadened PL linewidth indicates that the size distribution of Si-QDs in yellow-ASE sample is much broader than other cases, which also exhibits a larger dispersion on luminescent lifetime to cause the lowest dispersion factor. The gain coefficients of blue/yellow/red-ASE sample measured by VSL method are 157/62/85.6 cm^{-1}, respectively. By using the maximum gain-length product and TRPL analysis, the Si-QDs emission cross-section area of blue/yellow/red-ASE samples is $1.37\times10^{-14}/6.84\times10^{-16}/\ 0.64\times10^{-16}$ cm^2, respectively. The high-gain blue-ASE sample exhibits a shorter saturation length of 0.25 mm with the highest loss coefficient due to scattering loss by Si-QDs of the highest density. In addition, the gain saturation of the Si-QD based strip-loaded waveguide is discussed.

Nanoplasmonic and electrochemical biosensors formedical diagnosis and cellular analyses

Eiichi Tamiya

Department of Applied Physics
Osaka University

Nanostructured metals have been studied for the localized surface plasmon resonance (LSPR) and electrochemical biosensors. Photonic plasmon spectra are caused by the refractive index variations that result from the binding of molecules to the metal nanostructures. There are optically detectable parameters in biophotonics and biosensor devices. We have studied three types of nanostructures, gold-capped nanostructure connecting with the core of silica nanoparticle capped by deposited gold film, gold-deposited porous anodic alumina layer chip and gold nanoparticles onto silicon oxide /silicon interferrometric multilayer as our original works. The bio-sensing of these nanostructures have been examined by monitoring the biomolecular interactions in various flexible formats. Antibody-antigen and DNA hybridization reactions were performed to detect various biomarkers, with the detection limit of picogram levels. The multi array format was constructed by a core-shell structured nanoparticle layer, which provided 300 spots on the sensing surface. A microfluidic biochip based on PDMS was useful for real-time analysis, rapid detection. DNA amplification process (PCR) and monoclonal antibody production from hybridoma cell library can be monitored. Electrochemistry measurements connecting to core-shell structure nanoparticle were successfully exploited in a simultaneous detectable scheme. The binding of melittin to lipid membrane was measured using localized surface plasmon resonance, and the permeability of the lipid membrane was then assessed electrochemically as a function of melittin with the purpose of seeking a novel, sensitive detection system for peptide toxins.Surface Enhanced Raman Scattering (SERS) was also discussed with gold and silver nanoparticles interacting with bio-molecules. Gold nanoparticles were successfully delivered into single cells. Spatiotemporal measurements of SERS fingerprints suggested the dynamic molecular interactions and transformations taking place at different locations with time in cardiomyocytes.

References

Anal. Chem.82 (4) 1221 (2010)Anal.Chem.,82 (4), 1349 (2010)Anal.Bioanal.Chem. 396, 2575 (2010) ACSNano. 3(2) 446 (2009) Anal.Chem. 80(6) 1859 (2008) Anal. Biochemistry379(1) 1 (2008) Anal.Chim. Acta 614 (2) 182 (2008) Talanta, 74 (4) 1038 (2008) Anal.Chem. 79(5) 1855 (2007) Anal. Chem.79(2) 782 (2007)Anal.Chem.78, 6465 (2006)PLoS ONE, 6(8) e22801 (2011)

Nanoscale Photon Management for Efficient Photovoltaic Energy Harvesting

Jr-Hau He

Institute of Photonics and Optoelectronics & Department of Electrical Engineering, National Taiwan University, Taipei 106, Taiwan
Email: jhhe@ntu.edu.tw

It is of current interest to develop the antireflection (AR) coatings with nanowire arrays (NWAs) since the ability to suppress the reflection over a broad range of wavelengths and incident angles plays an important role in the performance of optoelectronic devices, such as photodetectors, light-emitting diodes, optical components, or photovoltaic systems. Superior AR characteristics of NWAs, including polarization-insensitivity, omnidirectionality, and broadband working ranges are demonstrated in this study. These advantages are mainly attributed to the subwavelength dimensions of the NWAs, which make the nanostructures behave like an effective homogeneous medium with continuous gradient of refraction index, significantly reducing the reflection through destructive interferences. The relation between the geometrical configurations of NWAs and the AR characteristics is discussed. We also demonstrated their applications in solar cells. This report paves the way to optimize the nanostructured optoelectronic devices with efficient light management by controlling structure profile of nanostructures.

Nano-spectroscopy with plasmonic antennas

Prabhat Verma*

Department of Applied Physics, Osaka University, Suita, Japan
Email: verma@ap.eng.osaka-u.ac.jp

Optical spectroscopy in the visible region is a very important approach, not only to characterizing various kind of samples, but also to understand many basic physical or chemical properties of these sample. This is because most of the naturally existing samples that we interact with in day-to-day life have electronic and vibrational energies that are similar to the energies carried by visible light (from near-UV to near-IR). Therefore, visible light can interact efficiently with the intrinsic properties of the sample, and spectroscopy in visible range can fetch rich information about the sample. However, interaction of light with matter is usually a weak phenomenon. For example, when a sample is illuminated with a particular light source, only one in a million photons undergoes Raman scattering. This is particularly important for nanomaterials with extremely small sample volumes, where the strength of optical scattering becomes very weak. Hence, in order to observe scattering from nanomaterials, one of the important requirements is to enhance the scattering, so that even weak scattering can become observable under usual experimental conditions.

Another issue in spectroscopy at nanoscale is that the wave nature of light prevents it to get focused in a space smaller than half of its wavelength, a phenomenon known as the diffraction limit. Therefore, visible light cannot be focused into a space smaller than about 200~300 nm. This size is much larger than most of the nanomaterials that one would like to study. Therefore, another important requirement for optical nano-spectroscopy is to confine the light field into nanoscale, so that one may obtain nano-sized spatial resolution. Both enhancement and confinement of light field can be achieved by utilizing plasmonic antennas, which are nothing but metallic nanostructures with specific shapes and sizes. Here, we will discuss about optimization of the antenna for better confinement and enhancement of light, and will show some results of enhanced and confined spectroscopy at nanoscale. We will also show some examples of optical imaging through plasmonic antennas, where we can achieve very high spatial resolution, far beyond the diffraction limit.

(1). Saito, Y.; Ohashi, Y.; Verma, P. *Int. J. Optics.* **2012**, *(in Press)*.
(2). Verma, P.; Ichimura, T.; Yano, T.; Saito, Y.; Kawata, S. *Laser & Photonics Rev.* **2010**, *4*, 548.
(3). Yano, T.; Verma, P.; Saito, Y.; Ichimura, T.; Kawata, S. *Nature Photon.* **2009**, *3*, 473.
(4). Kawata, S.; Inouye, Y.; Verma, P. *Nature Photon.* **2009**, *3*, 388.

TBD

Polymeric Light Emitting Diodes and Transistors Utilizing Poly(alkylfluorene) Derivatives

Yutaka Ohmori* and Hirotake Kajii

Graduate School of Engineering, Osaka University, Suita, Osaka 565-0871, Japan
Email: ohmori@oled.eei.eng.osaka-u.ac.jp

Polymeric materials are one of promising materials for organic electronics devices fabricated by printing technology. Among polymeric materials, poly(9,9-dialkylfluorene) (PFO) is one of soluble conducting polymers for polymeric light-emitting diodes (PLEDs) and organic field-effect transistors (OFETs), which exhibit high fluorescence quantum yield, high electron and hole mobility and good thermal stability. Layered PLEDs were fabricated by solution process in order to enhance the emission characteristics, especially, emission intensity and emission efficiency. The PLEDs have been discussed as an electro-optical conversion device for optical signal transmission. Top gated-type ambipolar organic field effect transistors utilizing polyfluorene derivatives were fabricated, and their ambipolar and the light emission characteristics have been discussed.

Molecular structures of polymeric materials, poly(9,9-dioctylfluorene) (PFO), poly(9,9-dioctylfluorene-co-benzothiadiazole) (F8BT), poly(9,9-dioctylfluorene-co-N-(4-butylphenyl)-diphenylamine) (TFB)) and device structures (OLED, OFET) are shown in Fig. 1. A yellow-green emission was observed from a multi-layer PLED based on F8BT, whose device structure is shown in Fig. 1(d). 10-nm-thick TFB was inserted as an interlayer. The luminance of the PLED with TFB increased in the forward bias direction above a threshold voltage of about 2 V. The emission intensity reached as high as 57,000 cd/m^2 at 9 V. It showed a peak efficiency of 6.7 cd/A, an improvement of more than 16 times in their performance, compared with the device without TFB interlayer. In order to obtain a high frequency operation of the PLED, the device size as small as 0.3 mm^2 was used. Direct operation of 100 MHz was realized[1)] at an applied pulsed voltage of 16 V. The device is applicable for optical signal transmission[2)].

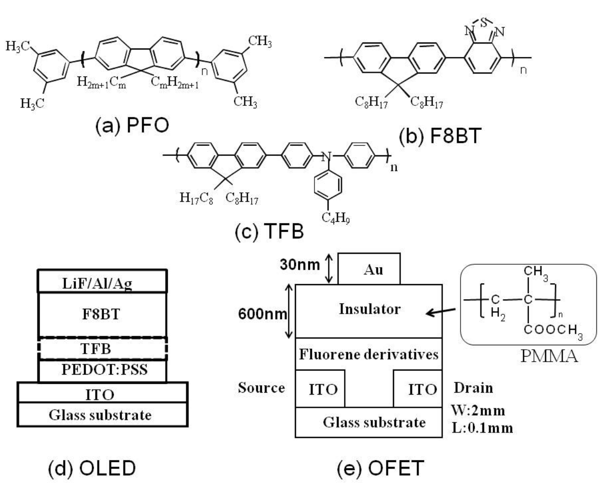

Fig. 1

Ambipolar characteristics of solution processed top-gate type OFETs with ITO source/drain electrode utilizing polyfluorene derivatives are demonstrated. All OFETs with poly(alkylfluorene) derivatives exhibited ambipolar characteristics. The field-effect hole and electron mobility of PFO device were estimated as $\mu_h = 0.7 \times 10^{-3}$ cm^2/Vs and $\mu_e = 1.2 \times 10^{-3}$ cm^2/Vs, respectively. The field effect mobility of F8BT device estimated as $\mu_h = 0.8 \times 10^{-3}$ cm^2 /Vs and $\mu_e = 0.4 \times 10^{-3}$ cm^2 /Vs, respectively. The ambipolar OFETs with PFO, F8BT and F8BT:F8 exhibited the blue, yellow green and white EL emissions by varying the gate voltages, respectively. Top gate-type poly(alkylfluorene) based OFETs with ITO drain/source electrodes have been demonstrated as light-emitting transistors[3)].

(1). Kajii, H.; T. Kojima, T.; Ohmori, Y. *IEICE Trans. Electron.* **2011**, *94-C*, 190-192.
(2). Ohmori, Y.; Kajii, H. *Proceedings of IEEE* **2009**, *97*, 1627-1636.
(3). Kajii, H; Koiwai, K.; Hirose, Y.; Ohmori, Y. *Organic Electronics* **2010**, *11*, 509-513.

Modeling and Analysis of Optical Transmission and Reflection of Double Nano-silt Metallic Gratings

Sun-Jung Lin and Ding-Wei Huang*

Graduate Institute of Photonics & Optoelectronics, National Taiwan University, Taipei 10617, Taiwan
Email: dwhuang@cc.ee.ntu.edu.tw

Double nano-slit metallic gratings are one-dimensional periodic structures which have two nano-slits within each grating period. The characteristics of optical transmission and reflection as the light is incident onto the double nano-slit metallic gratings will be dominated by the properties of each nano-slit and the optical coupling between of the nano-slits. In this thesis, an analytical model of the optical transmission and reflection properties for the light incidence onto nano-slit metallic gratings was derived. The metal nano-slit region of double nano-slit metallic gratings is similar to the five-layer planar structure of staggered metal and dielectric materials, which has two surface plasmon modes. Thus, when the light is incident onto the double nano-slit metallic gratings, two surface plasmon modes may be excited in the metal nano-slit region. The modal characteristic equation of the metal-dielectric staggered five-layer planar structure was also derived and the solution to the modal characteristic equation yields the effective refractive indices of the two surface plasmon modes which can be used to describe the propagation characteristics of these two surface plasmon modes in the metal slit region. The Fabry-Pérot interference may occur as the two surface plasmon modes bounces back and forth independently along the metal nano-slits due to the abrupt reflective index change at the top and bottom interfaces. In case of resonance, dips in the reflectivity spectrum and peaks in the transmittance spectrum will appear. The orthogonality of the two surface plasmon modes as well as the boundary condition were then used to derived the analytical model of the optical transmission and reflection of the double nano-slit metallic gratings. The results obtained by using the analytical model are in good agreement with those by using rigorous coupled wave analysis (RCWA). Although the analytical model is not completely accurate, it allows us to obtain new physical insight into the behavior of the surface plasmon modes in the double nano-slit metallic gratings and to calculate the numerical solutions with a considerably reduced computation time.

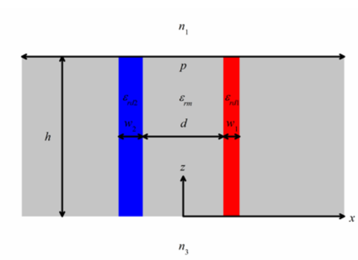

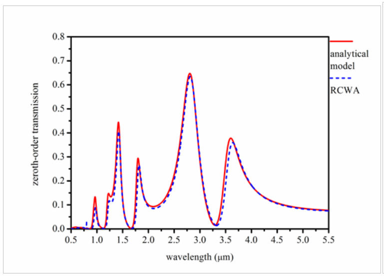

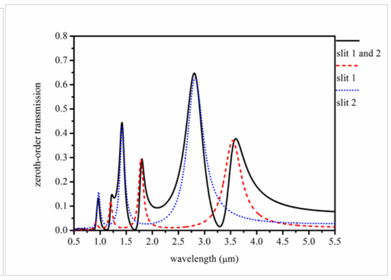

(1). F. J. Garcia-Vidal, and L. Martin-Moreno, "Transmission and focusing of light in one-dimensional periodically nanostructured metals," Phys. Rev. B 66, 155412 (2002).
(2). Sun-Jung Lin, Modeling and Analysis of Optical Transmission and Reflection of Double Nano-silt Metallic Gratings, Master Thesis for Graduate Institute of Photonics and Optoelectronics, National Taiwan University, 2011

Logic gate and shift register with magnetic quantum dots cellular automata

Hikaru Nomura, **Mayu Komura**, **Masashi Kusukawa**,
Soichiro Miura, **Yukihiro Imanaga**, **and Ryoichi Nakatani**

Department of Materials Science and Engineering
Graduate School of Engineering, Osaka University, 2-1 Yamada-oka, Suita, Osaka, JapanEmail:
nomura@mat.eng.osaka-u.ac.jp

A magnetic quantum dots cellular automata (MQCA)[2] composed of nano-magnet can perform data transfer and logical operation by a magneto-static interaction. MQCA has advantages of high integration density, fast operation and non-volatility. Combination of the photonics and the MQCA will open the way to fabricate fast and low power logic devices without using conventional electronics circuits.

Here, we experimentally demonstrate that that a MQCA gate and a MQCA shift register can operate at room temperature. The MQCA gate is composed of four elliptical dots, and a magnetization of each dot represents a bit of digital information (“0” or “1”). A MQCA shift register is composed of two types of dots; data dots and buffer dots.

As a MQCA element, elliptical Ni-20at.%Fe dots with long/short axis of 100 nm/50 nm, thickness of 20 nm, were fabricated on a thermally oxidized Si(100) substrate by electron-beam lithography, ion beam sputtering, and a lift-off technique. All experiments were performed in vacuum condition at room temperatures with a commercial atomic force microscopy (SII-A300) and originally developed manipulation system by LabVIEW. To read or write digital information on to the dots, we developed a magnetization manipulation method based on magnetic force microscopy (MFM).

Figures 1 show the MFM images of the MQCA gate (a-p) before and (a’-p’) after the NAND/NOR logical operation. Each dot produces a dark-bright pair in MFM signal, which correspond to a single-domain state. After the clock-field were applied, the direction of the magnetization of output Z were changed into the direction which correspond to the truth table of NAND/NOR logic gate[3]. Note that the logical operations are independent of the output Z initial binary states. By creating an arrayed MQCA gate with the MQCA shift register, highly functional circuits based on a cellular automaton theory can be realized.

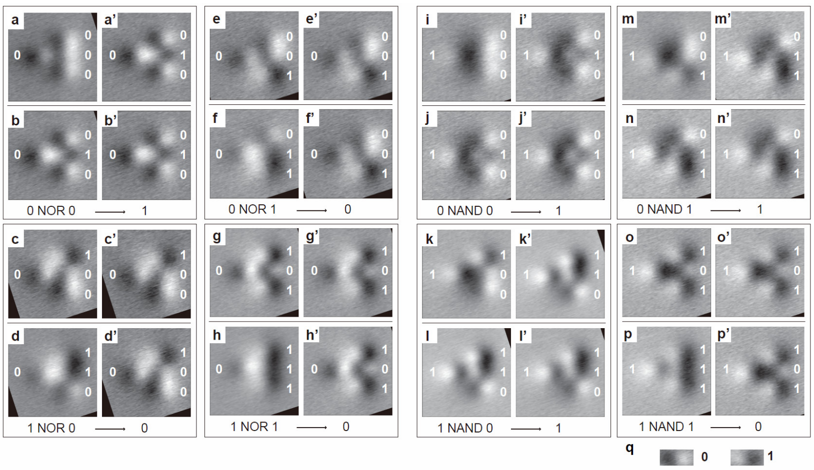

Figure 1. Experimental results of NAND/NOR logical operation with a MQCA gate. MEM image of the (a-p) initial states and (a’-p’) operational results of the MQCA gate with a scanning area of 650 ×650 nm^2 are shown. The MQCA gate shows the correct NAND/NOR logical operation by changing the binary state of the input dots[3].

[1] S. A. Haque, M. Yamamoto, R. Nakatani, Y. Endo, *J. Magn. Magn. Mater.* **282** (2004) 380.
[2] R. P. Cowburn, M. E. Welland, *Science* **287** (2000) 1466.
[3] H. Nomura and R. Nakatani, *Appl. Phys. Express* **4** (2011) 013004.

Metamaterials with Multiple Plasmonic Resonances towards Complex Optical Functionalities

Ta-Jen Yen*

Department of Materials Science and Engineering, National Tsing Hua University, Hsinchu 300, Taiwan
Email: tjyen@mx.nthu.edu.tw

Metamaterials attract much attention owing to their notable electric or magnetic properties, which originated from their specially designed architecture rather than their constitutive compositions. In this talk, I will share three kinds of non-conventional plasmonic responses by means of electromagnetic metamaterials. First is the plasmonic resonance with a greater quality factor, realized by hybridizing plasmonic resonances within two engineered resonating systems.[1,2] Next, we significantly reduced the intrinsic loss of the by exciting plasmonic-like resonance in the designed dielectric metamaterials. With these dielectric metamaterials, we can provide both negative permittivity and negative permeability, and even negative refractive index media.[3] Finally, we successfully delivered a two-handed metamaterials metamaterial that enables right-handed and left-handed passbands simultaneously, which can be readily employed for high-speed wireless transport and others.[4-6] By exciting multiple plasmonic resonances in the designed metamaterials, one can achieve complex optical functionalities for practical applications.[7]

(1). Chia-Yun Chen, Shich-Chuan Wu, and **Ta-Jen Yen***, "Experimental Verification of Standing-Wave Plasmonic Resonances in Split-Ring Resonators", ***Appl. Phys. Lett***., Vol. 93 (3), pp. 034110 (2008)

(2). Chia-Yun Chen, Ieng-Wai Un, Nyan-Hwa Tai and **Ta-Jen Yen***, "Asymmetric coupling between subradiant and superradiant plasmonic resonances and its enhanced sensing performance", ***Optics Express***, vol.17 (17), pp. 15372-15380 (2009)

(3). Yue-Jun Lai, C. K. Chen, **Ta-Jen Yen***, "Creating negative refractive identity via single-dielectric resonators", ***Optics Express,*** Vol. 17 (15), pp. 12960–12970 (2009) Y. J. Chiang and **Ta-Jen Yen*,** "A highly symmetric two-handed metamaterial spontaneously matching the wave impedance", ***Optics Express,*** Vol. 16 (17), pp. 12764-12770 (2008)

(4). Y. J. Chiang and **Ta-Jen Yen*,** "A highly symmetric two-handed metamaterial spontaneously matching the wave impedance", ***Optics Express,*** Vol. 16 (17), pp. 12764-12770 (2008)

(5). T.-Y. Huang and **T.-J. Yen***, "A high-ratio bandwidth square-wave-like bandpass filter by two-handed metamaterials and its application in 60 GHz wireless communication", ***PIER Letters***, Vol. 21, pp. 19-29 (2011)

(6). Yi-Ju Chiang, Chan-Shan Yang, Ci-Ling Pan and **Ta-Jen Yen***, "An ultrabroad terahertz bandpass filter based on multiple-resonance excitation of a composite metamaterial", ***Appl. Phys. Lett***. Vol 99, 191909, (2011)

(7). Yun-Tzu Chang, Yueh-Chun Lai, Chung-Tien Li, Cheng-Kuang Chen, and **Ta-Jen Yen***, "A multi-functional plasmonic biosensor", ***Optics Express***, Vol. 18, pp. 9561-9569 (2010)

Compact plasmonic resonators

Masanobu Haraguchi*, **Toshihiro Okamoto, Tetsuya Fukuita, Shuji Sato, and Naohiro Kamon**

Department of Optical Science and Technology, University of Tokushima, Tokushima 770-8506, JAPAN
Email: haraguti@opt.tokushima-u.ac.jp

Compact plasmonic resonators with sub-wavelength size are strongly noticed because they are expected to realize tiny optical devices for data processing and for sensing. And negative refractive index materials (NIM) may be also consisted by such resonators. Many research groups are working on demonstrations with various structures as resonators but it is still difficult to fabricate suitable resonators satisfying applications-level performance with low-cost method. In this paper, we propose two types of resonator: one is a cascade stub resonator (CSR) in a plasmonic waveguide with the focused-ion beam (FIB) direct processing and the other is a sprit-ring resonator (SRR) with the nanosphere lithography. The former and the latter are suitable for devices in a plasmonic waveguide and for sensors and NIM, respectively.

CSRs are consisting of two finite-length branches (stubs) in a plasmonic waveguide and are simple and easy to fabricate[1]. We fabricated CSRs in a gap plasmon and a V-groove plasmon waveguide on a silver film for near-infrared region: stub length was around 300 nm and the total length of the resonator was around the wavelength of the plasmon, i.e., area size is less than 1 square μm as shown in Fig.1. Silver SRRs are fabricated by employing the nanosphere lithography technique with spheres of 100 nm in diameter on a glass substrate[2]. As shown in Fig. 2, The typical diameter and gap of the SRR are approximately 130 nm and 55 nm, respectively. We measured the intensity of the light scattered from the resonators using a confocal microscope spectroscopy system and estimated the optical characteristics taking into account with the numerical results.

For a CSR, we observed a resonance in scattering spectra when the plasmonic wave was excited. The Q factor was estimated to be 20 from FWHM of the resonance peak that was much smaller than that expected by numerical result. For SRR, we observed two peaks in the light scattering spectra as shown in Fig. 3; the long wavelength peak corresponds to a fundamental LC resonance mode excited by an incident electric field considering numerical simulation results of the electromagnetic field distribution of the SRR. It was shown that a single structure can operate as a resonator and generate a magnetic dipole.

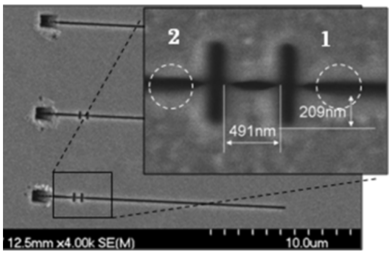

Fig.1 SEM image of Cascade stub resonaro

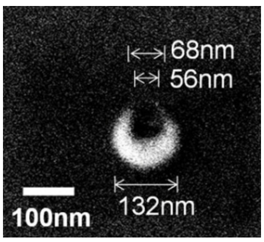

Fig. 2 SEM image of a SRR.

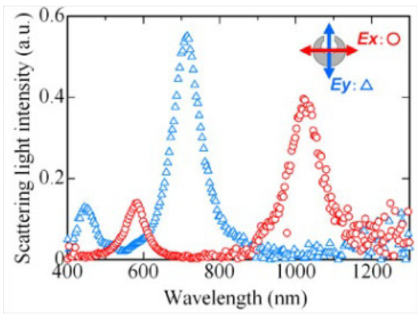

Fig. 3 light scattering spectra from a SRR.

(1). Matsuzaki, Y.; Okamoto, T.; Haraguchi, M.; Fukui, M.; Nakagaki, M. Optics Express **2008** 16, 16314.
(2). Okamoto, T.; Fukuta, T.; Satou S.; Haraguchi, M.: Fukui, M. *Optics Express* **2011**, 19, 7068.

Microcavity Laser with Efficient Data Transmission

Chao-Hsin Wu

Institute of Photonics and Optoelectronics, National Taiwan University, Taipei 106, Taiwan
Email: chwu@cc.ee.ntu.edu.tw

Microcavity lasers (μCLs), reduced-size (≤ 3 μm aperture) vertical cavity surface-emitting lasers (VCSELs) defined by the buried-oxide process for current and field confinement (thus wide mode spacing), are demonstrated with wider mode spacing and faster spontaneous carrier recombination (enhanced Purcell factor), low threshold current, large side mode suppression ratio(SMSR), sharp turn-on L-I characteristics, and wide bandwidth operation[1-3]. The reduced cavity volume helps increase cavity quality factor and limits the number of available modes in μCLs, resulting in an enhanced Purcell effect and faster recombination rate. Due to the enhanced spontaneous recombination rate at reduced mode and improved photon density, μCLs exhibit lower charge-field resonance peaks at a modulation bandwidth f_{-3dB} = 18.7 GHz, thus permitting open-“eye” operation at 20 and 40 Gb/s data rates (I ≤ 3 mA). The energy efficiency for 20 Gb/s data transmission is measured to be 4.84 Gb/s per mW, which is eight times better than 7 μm aperture VCSELs. The modulation current efficiency factor is improved and a better quality eye diagram in high speed data transmission can be obtained.

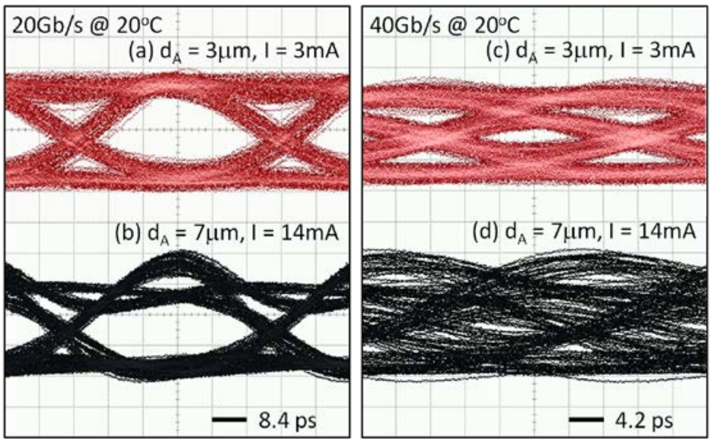

Fig. 1 Eye diagram of μCL and normal VCSEL operated at 20 and 40 Gb/s

(1). C. H. Wu, F. Tan, M. Feng, and N. Holonyak, Jr., *Appl. Phys. Lett.*, 97, 091103, 2010
(2). C. H. Wu, F. Tan, M. K. Wu, M. Feng, and N. Holonyak, Jr., *J. of Appl. Phys.*, 109, 05312, 2011
(3). F. Tan, C. H. Wu, M. Feng, and N. Holonyak, Jr., *Appl. Phys. Lett.*, 98, 191107, 2011

Design of a castle-like shape core plasmonic nanoantenna with wavelengths ranging from UV, visible light and IR light

Yuan-Fong Chau* **and San-Cai Jheng**

Department of electronic Engineering, Ching Yun University, Jung-Li 320, Taiwan
Email: yfc01@cyu.edu.tw

A plasmonic nanoantenna is proposed and investigated numerically by using the three-dimensional finite element method. Results show that the resonant wavelength of the proposed nanoantenna may be tuned over a broad spectral by considering the contour of a castle-like shape core antenna and introducing the design parameters, the gap distance and contour thickness. These new antennas allow for a threefold reduction in the antenna footprint and an increase in the gap enhancement.

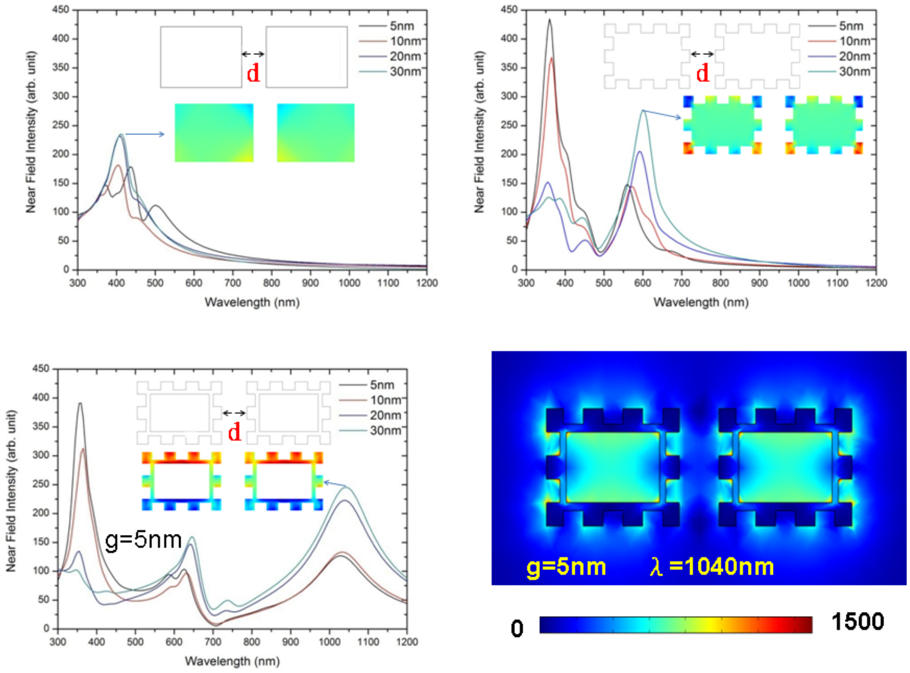

Fig. 1 Comparison of SPR effects on three patterns of optical nanoantenna

(1). Y.-F. Chau, H.-H. Yeh, and D. P. Tsai, J. Electromagn. Waves Appl. **2010**, 24 (8), 1005–1014 .
(2). Chau and H.-H. Yeh, J. Nanopart. Res. **2011**, 13(2), 637–644 .

Plasmon waveguide consisting of silver-shell nanorods in hexagonal lattice for subwavelength confinement and long-range propagation

Yuan-Fong Chau* and Ci-Yao Jheng

Department of electronic Engineering, Ching Yun University, Jung-Li 320, Taiwan
Email: yfc01@cyu.edu.tw

A two-dimensional plasmon waveguide in the form of rows of silver-shell nanorods distributed in a hexagonal lattice is proposed and compared to the solid-silver case. Transport of energy flow due to surface plasmon coupling is investigated using finite element method for visible range wavelengths. The proposed waveguide is divided into several sections with each section consisting of ten nanorods. Results show that the waveguide energy flow exhibits longranging propagation (>8 μm or more) by using series connection of each section, which plays the major role in coupling between them.

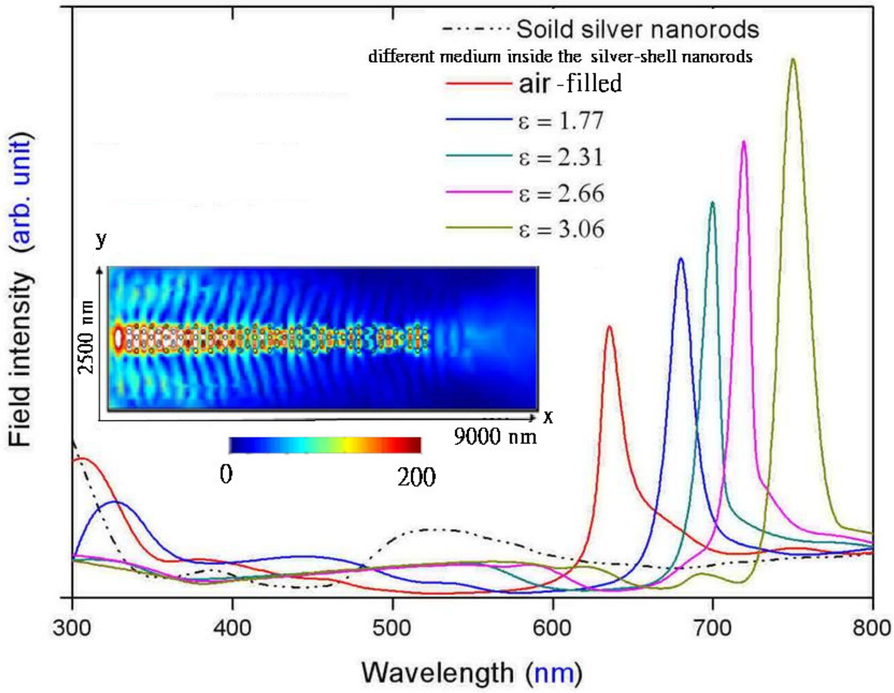

Fig. 1

Field intensities as a function of wavelengths for the solid-silver nanorods and different medium inside the nanorods for the silver-shell cases. Inset: Magnetic field component Hy of the propagating beam in the waveguide.

(1). P. B. Johnson, R. W. Christy, Phys. Rev. B **1972**, 6, 4370-4379.
(2). Y.-F. Chau, H.-H. Yeh, D. P. Tsai, Appl. Opt. **2008,** 47, 5557-5561.

Plasmonic Bloch-Zener Oscillations in Metal-Dielectric Waveguide Arrays

Ruei-Cheng Shiu and Yung-Chiang Lan*

Department of Photonics, National Cheng Kung University
Email: lanyc@mail.ncku.edu.tw

Plasmonic Bloch oscillations, an analog of electron Bloch oscillations in lattice, are periodic oscillations of optical beams that propagate in metal-dielectric waveguide arrays (MDWAs), which is caused by the alternating total internal reflection and Bragg reflection between the two boundaries of the waveguide arrays. When the electric field imposed on the lattice is increased, electron Zener tunneling will occur at the Brillouin zone boundary. However, plasmonic Zener tunneling has been never observed in MDWAs. Neither has the possibility that the optical beam tunneling into the next band will experience another Bloch oscillation been investigated. In this study, plasmonic Zener tunneling and the succeeding plasmonic Bloch oscillation in MDWAs are explored by performing both FDTD simulations and theoretical analyses. The MDWAs consists of alternative silver layers and dielectric layers. The relative permittivities of the dielectric layers have a constant gradient across the waveguide arrays. The plasmonic Zener tunneling is observed at the position of total reflection (Bloch wavevector kx = 0), which is caused by that the gap between the first and second equal-kz (longitudinal wavevector) bands is minimum at kx = 0, originated from the effectively (transverse) negative refraction index of the MDWAs. The relation between tunneling rate and permittivity gradient is elucidated. The FDTD-simulated contours of magnetic field intensity correlate well with the predicted ray trajectory using Hamiltonian optics. Furthermore, the tunneling beam is also observed to undergo Bloch oscillation in the FDTD simulation. This Bloch oscillation leads to beam's curling due to change of the direction of the energy flow. Depending on the material properties, the curling beam will move backward, move forward, or even be stationary.

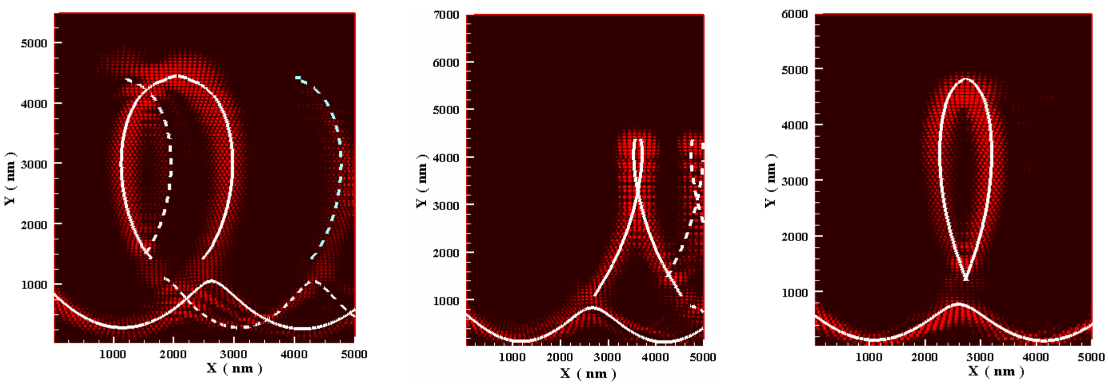

Figure 1 FDTD-simulated contours of magnetic field intensity $|H|^2$ for curling beam moving backward, moving forward and being stationary.

(1). R. C. Shiu and Y. C. Lan*, "Plasmonic Zener tunneling in metal-dielectric waveguide arrays," Opt. Lett. 36, 4179-4181, 2011.

Guided-mode resonance enhanced second- and third-harmonic generation in an azo-polymer waveguide grating structure

Jian Hung Lin[1*], **Hung-Chih Kan**[1], **and Chia Chen Hsu**[1,2,3]

[1]*Department of Physics, National Chung Cheng University, Ming Hsiung, Chia Yi 621, Taiwan*

[2]*Graduate Institute of Opto-Mechatronics, National Chung Cheng University, Ming Hsiung, Chia Yi 621, Taiwan*

[3]*Department of Photonics, National Sun Yat-sen University, Kaohsiung 804, Taiwan*

[*]*Email: phyjhl@ccu.edu.tw*

In this work, we demonstrate the enhancement of second- and third-harmonic generation (SHG and THG) in an azo polymer waveguide grating structure (WGS). Comparing with a sample without WGS, the SHG and THG output can be enhanced by 1000 times thanks to the guided-mode resonance (GMR) effect in the WGS. Figure 1(a) shows the SEM image of a one-dimensional (1D) WGS, which contains a 1D grating layer (TiO_2) and a buffer layer (SU8) on the top of a glass substrate. To produce second- and third-harmonic generation, an azo copolymer thin film, which was used as a nonlinear material, was spun-cast on the top of the TiO_2 layer with a thickness about 1.1 um. Finally, a corona electric field poling technique was employed to align azo copolymer to form non-centro symmetric distribution.

To measure THG and SHG generated from the azo copolymer WGS, a tunable wavelength optical parametric oscillator (OPO) laser beam with 10 ns pulse width, 10 Hz repetition rate and an average power of 5 mW was used as a fundamental beam. The collimated fundamental beam was normally transmitted through the WGS sample and the THG and SHG output were detected by a spectrometer. Figure 1(b) and (c) show the THG and SHG spectra, respectively, of the WGS covering with (red-color) and without covering (black-color) the electrically-poled azo copolymer layer. As shown in both figures, strong THG and SHG outputs appear at particular fundamental wavelengths where GMR occur. From a simulation, we found at GMR wavelength, strong localized electric field is generated at the azo copolymer and TiO_2 layers. The strong SHG and THG resonance are associated with the GMR related local field enhancement effect.

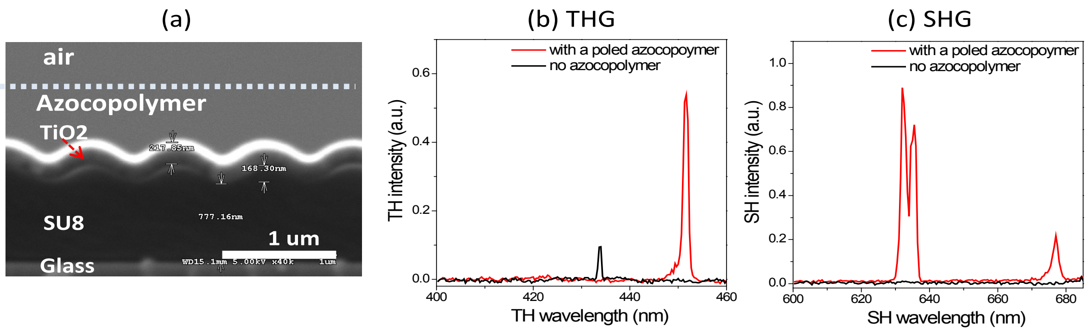

Fig.1. (a) SEM image of the 1D WGS. (b) THG and (c) SHG output spectra obtained from 1D WGS covering with and without covering an azo copolymer thin film.

Bilayer Graphene for Active Plasmonics and Metamaterials

Atsushi Ishikawa* **and Takuo Tanaka**

Metamaterials Laboratory, RIKEN, 2-1 Hirosawa, Wako, Saitama 351-0198, Japan
Email: a-ishikawa@riken.jp and t-tanaka@riken.jp

Graphene, densely-packed carbon atoms in a two-dimensional (2D) honeycomb lattice, has recently attracted much interest due to its superior electronic and optical properties[1,2]. One of the exceptions is that monolayer graphene exhibits ultra-high mobility (up to $\mu \approx 10^6$ cm^2 V^{-1} s^{-1}), which arises from the nature of charged massless carriers, so-called "Dirac fermions". Since ballistic transport of electrons over micrometers can be realized even at room temperature, a wide variety of graphene studies have been extensively explored, ranging from high-frequency electronics to relativistic condensed-matter physics[3].

Bilayer graphene, on the other hand, is even more interesting. While monolayer graphene has no bandgap, bilayer one exhibits band splitting due to the interlayer interaction and acquires a gate-voltage-controllable bandgap (Figure 1). Since the tunable range of the bandgap is 0 ~ 300 meV, corresponding to the mid-IR/THz region, this can be used for active devices utilizing interband transitions with absorption and emission of photons, especially, the population inversion under appropriate pumping. Such a unique material platform may open up new approaches for offering novel functionalities in plasmonics and metamaterials.

Here, we propose an active metamaterial that acts as a coherent IR/THz light source by embedding a nano-metallic resonator array onto bilayer graphene, which provides necessary optical gain (Figure 2)[4]. The resonators are designed to have the same resonant frequency as the interband transition (bandgap energy) of bilayer graphene. The resultant strong interaction of the metamaterial with graphene 2D electron system allows for efficient nonradiative energy exchange, leading to successive amplification of localized plasmon modes at the resonators. The proposed bilayer graphene-based light source could be important because of the lack of high performance lasers in this spectral region. In this presentation, fabrication and characterization of bilayer graphene device will be also discussed.

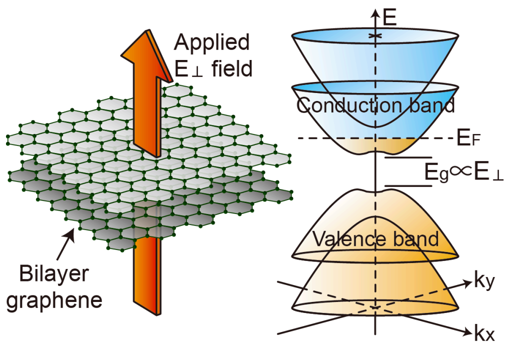

Fig. 1 Tunable bandgap E_g in bilayer graphene induced by applied gate electric field $E_\perp$.

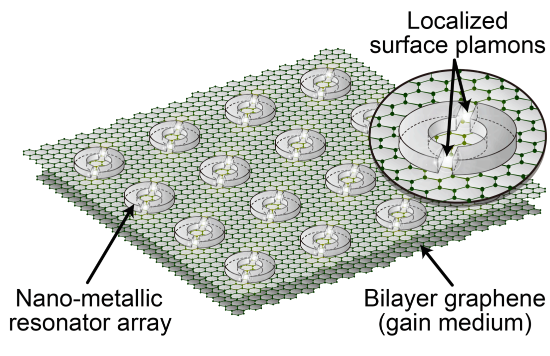

Fig 2. Bilayer graphene-based active metamaterial

(1). A. K. Geim and K. S. Novoselov, *Nat. Materials* **2007**, 6, 183.
(2). F. Bonaccorso, Z. Sun, T. Hasan, and A. C. Ferrari, *Nat. Photonics* **2010**, 4, 611.
(3). F. Schwierz, *Nat. Nanotech.* **2010**, 5, 487.
(4). N. I. Zheludev, S. L. Prosvirnin, N. Papasimakis, and V. A. Fedotov, *Nat. Photonics* **2008**, 2, 351.

Photovoltaic Properties of Organic Solar Cells utilizing Liquid Crystalline Phtalocyanine Derivative and Its Application for Tandem Solar Cell

Kaoru Fukumura*[1], Tetsuro Hori[1], Tetsuya Masuda[1], Dao Quang Duy[1], Takeshi Hayashi[1], Toshiya Kamikado[1], Fabien Nekelson[1,2], Hiroyuki Yoshida[1], Akihiko Fujii[1], Yo Shimizu[2], Masanori Ozaki[1]

[1]*Division of Electrical, Electronic and Information Engineering, Graduate School of Engineering, Osaka University, 2-1 Yamada-oka, Suita, Osaka 565-0871, Japan*

[2]*Research Institute for Ubiquitous Energy Devices, Kansai Centre, National Institute of Advanced Industrial Science and Technology (AIST), 1-8-31 Midorigaoka, Ikeda, Osaka 563-8577, Japan*

Email: kfukumura@opal.eei.eng.osaka-u.ac.jp

Organic thin-film solar cells based on a bulk heterojunction utilizing the soluble phthalocyanine derivative, 1,4,8,11,15,18,22,25-octahexylphthalocyanine ($C6PcH_2$) have been studied[1]. $C6PcH_2$ is a low-molecular-weight organic semiconductor with liquid crystallinity and high solubility to typical organic solvents, such as chloroform. Therefore, the blend uniform thin films with the $C6PcH_2$ and fullerene derivative (PCBM) can be fabricated by wet process, such as spin-coating. It is important to optimize an active layer thickness because the photovoltaic properties of the solar cells strongly depend on the active layer thickness. Thickness of active layers was changed 80-280 nm by controlling the concentration of mixed solutions with $C6PcH_2$ and PCBM. The absorption loss in the wavelength range of 400-600 nm is another problem in the organic thin-film solar cell utilizing $C6PcH_2$, therefore, it is effective to fabricate the tandem structure with poly(3-hexylthiophene) (P3HT).

Figure 1 shows the active layer thickness dependence of the short circuit current density (I_{sc}) and energy conversion efficiency (η_e). The I_{sc} linearly increased as the active layer thickness less than 140 nm, and then it was saturated in that of more than 140 nm. In the case of typical P3HT:PCBM bulk heterojunction solar cells, the I_{sc} was not saturated, but decreased with increasing of the active layer thickness. The generated carriers could be transported to the electrodes efficiently because of the high carrier mobility of $C6PcH_2$[2]. Therefore, the I_{sc} was maintained even in the solar cells with thick active layer. On the other hand, the fill factor was suppressed, because of increasing the internal series resistance of the thick active layer. As the results, the maximum energy conversion efficiency of 3.1% was obtained at the thickness of 120 nm.

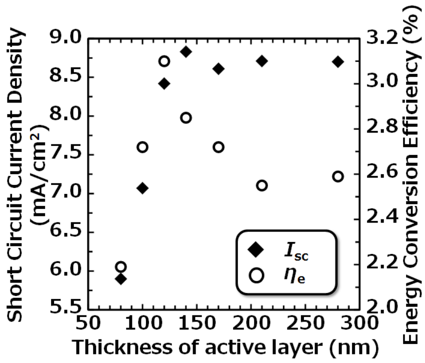

Fig. 1 Active layer thickness dependence of I_{sc} and η_e.

Figure 2 shows the current-voltage characteristics of the tandem cell, P3HT single cell and $C6PcH_2$ single cell. In the tandem cell, the high V_{oc} of 1.27 V was observed, and the small loss of 0.04 V compared with the sum of the V_{oc} of both single cells was observed. Therefore, it is considered that the interlayer of the tandem solar cell effectively behaved as an intermediate electrode and the both active layers were connected with the series.

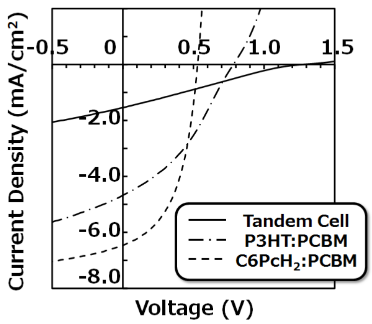

Fig. 2 I-V characteristics of the tandem cell, and single cells.

Acknowledgement

This work has been supported by Photonics Advanced Research Center at Osaka University.

[1] T. Hori *et al*., *Appl. Phys. Express*, 3, 101602, (2011)., *Sol. Energy Mater. Sol. Cells*, 95, 3087, (2011).

[2] Y. Miyake *et al*., *Appl. Phys. Express*, 4, 021604, (2011).

Excitation of surface plasmon polaritons by *s*-polarized light at an anisotropic dielectric-metal interface

Yasuo Kimoto and **Shinji Hayashi** *

Department of Electrical and Electronics Engineering, Graduate School of Engineering, Kobe University, Kobe 657-8501, Japan
Email: 105t220t@stu.kobe-u.ac.jp

Surface plasmon polaritons (SPPs) are coupled modes of electromagnetic waves and collective oscillations of free electrons localized at metal-dielectric interfaces. SPPs are transverse-magnetic (TM) waves, and only *p*-polarized light can excite them. Recently Li *et al*[1]. have predicted the polarization-hybridized nature of SPPs propagating at an interface between an anisotropic dielectric and a metal. In this work, from the calculation of the reflectance and the electric field pattern, we demonstrate that SPPs at such an interface can also be excited by *s*-polarized light.

We assume a Krerschmann configuration shown in Fig. 1. We calculate the reflectance as a function of the incident angle θ_{in} for several azimuthal angles φ. The angle φ is defined as the angle between the x axis and the optical axis of the anisotropic dielectric. Figure 2 shows calculated reflectance curves for *s*-polarized incident light. We clearly see the reflectance dips for the structure consisting of the anisotropic dielectric. We calculate the electric field pattern along the z axis for *s*-polarized incident light at the angles of reflectance dips in Fig. 2. As for Ex and Ez components, the pattern is very similar to that of SPPs at an isotropic dielectric-metal interface. Therefore, we conclude that the reflectance dip is derived from SPPs excitation. As for Ey component, the field is not zero unlike SPPs at an isotropic dielectric-metal interface. There is a strong correlation between the reflectance depth and a magnitude of Ey component of SPPs at an anisotropic dielectric-metal interface. These results suggest that excitation of SPPs at an anisotropic dielectric-metal interface is caused by the interaction between Ey component of such SPPs and *s*-polarized light.

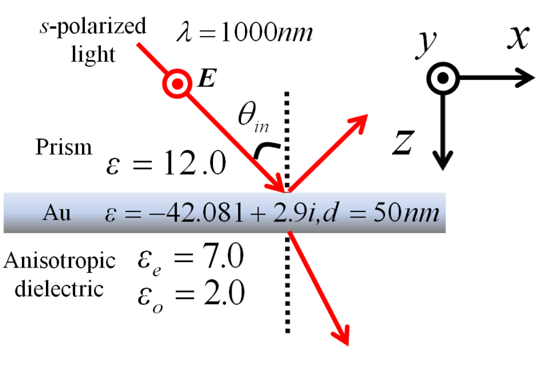

Fig. 1. Krerschmann configuration assumed for calculations.

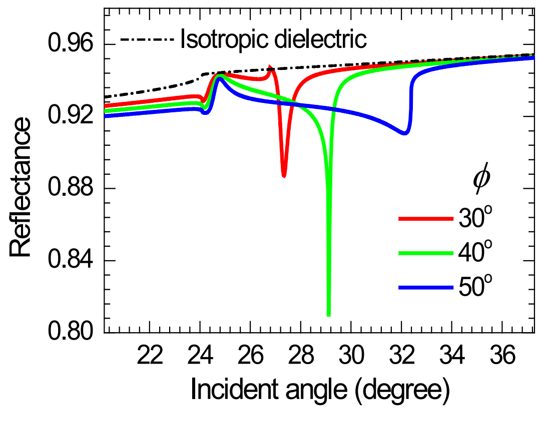

Fig. 2. Refrectance as a function of the incident angle θ_{in} for *s*-polarized incident light.

(1). Rui Li, Cheng Cheng, Fang-Fang Ren, Jing Chen, Ya-Xian Fan, Jianping Ding, Hui-Tian Wang, *Appl.Phys.Lett.* **2008**, 92, 14115.

Finite-Difference Time-Domain Analysis of Cholesteric Blue Phases Deformed by an Electric Field

Yasuhiro Ogawa[1], **Hiroyuki Yoshida**[1, 2], **Akihiko Fujii**[1] **and Masanori Ozaki**[1]

[1]Electrical and Electric Information Engineering, Osaka University, 2-1 Yamada-oka, Suita, Osaka, Japan
[2]PRESTO, Japan Science and Technology Corporation (JST), 4-1-8 Honcho, Kawaguchi, Saitama 332-0012, Japan
Email: yogawa@opal.eei.eng.osaka-u.ac.jp

Cholesteric blue phases (BPs) are liquid crystal phases which spontaneously form three dimensionally periodic helical structures with a periodicity of the order of a few 100 nms. BPs have attracted much attention due to their potential for tunable photonic crystal utilizing their sensitivity to external electric fields. However, the optical properties of BPs by deformed by an electric field have not been analyzed in detail. In this study, we calculated the photonic band structure and polarization dependence of the transmission properties of BPs deformed by an electric field using FDTD method[1]. Dielectric constant distributions of BPs calculated by Landau-de Gennes theory[2] was used in this calculation.

The unit cell of BPII was divided into 32 × 32 × 32 grids. Ordinary and extraordinary refractive index of liquid crystal were assumed to be $n_o = 1.5$ and $n_e = 1.7$, respectively, and the maximum order parameter in BPII unit cell was fixed to $S_{max} = 0.7$. Changes in the lattice constants of BPII caused by applying an electric field were implemented by changing the grid-size, which was set to $\Delta x = \Delta y = \Delta z = 4.25$ nm at zero electric field. Time difference was $\Delta t = 8 \times 10^{-18}$ sec. In photonic band calculation, Bloch's periodic boundary condition was imposed at each boundary of the BPII unit cell, and then eigenmodes for each wave vector in the brillouin zone was calculated. For the calculation of transmittance, 100 units of BPII were assumed to exist between two glass substrates ($n_s = 1.5$, d = 13.6 μm) aligned (100) plane. A gaussian pulse with linear and circular polarizations was excited at one of the glass substrates and the time dependence of electric field was observed at the other substrate.

Figure 1 shows the polarization dependence of transmission spectra of BPII (100) direction. Figure 1(a) shows the result at zero electric field ($\tilde{\varepsilon} = 0$), and (b) shows the result at $\tilde{\varepsilon} = 0.1$, where $\tilde{\varepsilon}$ is a proportional to the square of electric field. As the lattice structure was deformed by an electric field, the reflection band shifted towards longer wavelengths. However, the reflection was still polarization dependent.

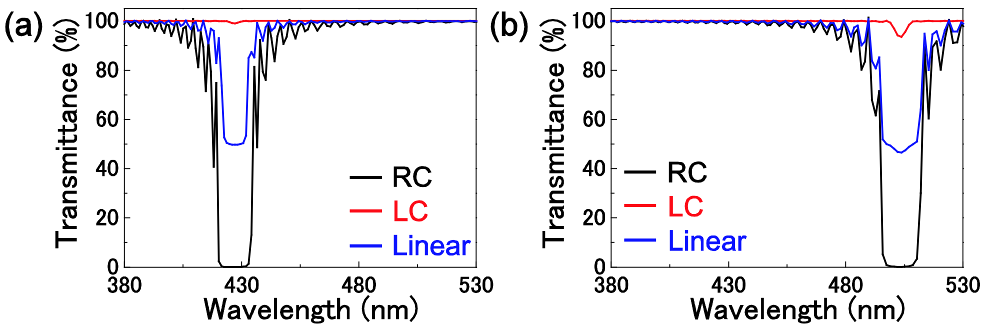

Fig. 1 Transmission spectra of BPII (100) direction at (a) $\tilde{\varepsilon} = 0$ and (b) $\tilde{\varepsilon} = 0.1$.

The author thanks Dr. Fukuda for providing the order parameter tensor of BPs calculated from Landau-de Gennes theory. This work was partly supported by Photonics Advanced Research Center at Osaka University

(1). M. Ojima, Y. Ogawa, R. Ozaki, H, Moritake, H. Yoshida, A. Fujii, and M. Ozaki, *Appl. Phys. Express.* **2010**, 3, 032001.
(2). J. Fukuda, M. Yoneya, and H. Yokoyama, *Phys. Rev. E* **2009**, 80, 031706.

Excitation of antisymmetric SPP modes in MIM structures by dye fluorescence

Shu Okada, Dai Nozaki, Minoru Fujii and Shinji Hayashi*

Department of Electrical and Electronics Engineering, Graduate School of Engineering, Kobe University, Rokkodai, 1-1, Nada, Kobe 657-8501, Japan

Email: hayashi@eedept.kobe-u.ac.jp

For a sufficiently thin insulator film sandwiched with metals, i.e., metal-insulator-metal (MIM) structure, it is well known that the coupling of surface-plasmon polariton (SPP) modes at the two metal-insulator interfaces results in two SPP modes, known as symmetric- and antisymmetric (AS) -SPP modes.[1] Theoretical analyses have shown that the AS-SPP mode has a waveguide mode character and persists even when the insulator thickness approaches zero; this means that there is no cutoff thickness. This mode is very much suited to make plasmonic slot waveguides with nanometer-size insulator cores and has been the subject of intensive theoretical and experimental investigation. However, because this mode is nonradiative mode, coupling devices, such as a grating, a prism and slits in one of the metal layers, are required for excitations by external light sources.

In this work, we succeeded in exciting AS-SPP modes in MIM structures by using fluorescence transition of an organic molecular layer as an excitation source. We embedded an organic dye (DCM) layer at the center of the MIM structure as shown in Fig. 1. Irradiating the MIM structure with a laser beam, SPP modes were excited via a fluorescence of the DCM molecules. The excited SPP mode was decoupled by a high refractive index prism and the emitted light spectra were measured as a function of detection angle. In Fig. 2, experimental dispersion curves obtained from emitted light spectra (square dots) are compared with theoretical dispersion curves (white regions in the grayscale map). The theoretical dispersion curves were calculated by CPS theory.[2] Figure 2 shows that the experimental results agree fairly well with the theoretical dispersion curve of the AS-SPP mode. The present results clearly demonstrate that the decoupled light from prism side was mediated by nonradiative AS-SPP mode. This excitation method has potential for applications in micro-MIM waveguides without coupling device.

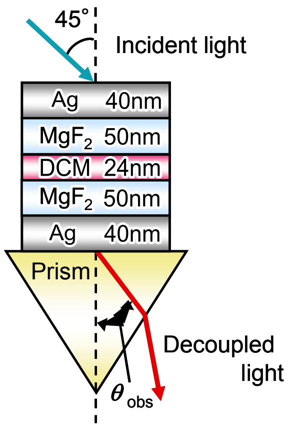

Fig. 1 Structures of MIM sample prepared.

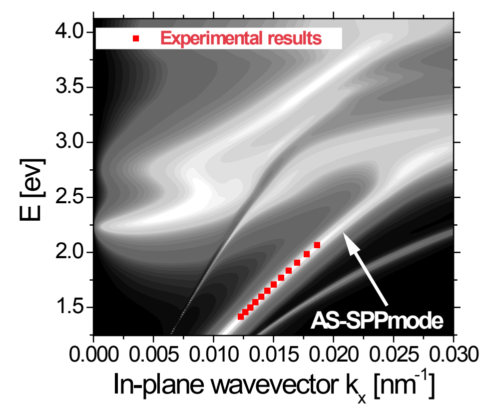

Fig. 2 Experimental dispersion curves obtained from emitted light spectra (square dots) and theoretical dispersion curves (grayscale map).

(1). Economou, E. *Phys. Rev.* **1969**, *182*, *2*, 539-554.

(2). Chance, R.; Prock, A.; Silbey, R. *Adv. Chem. Phys.* **1978**, *37*, 1-65.

Calculation of full band gaps for two-dimensional kagome photonic crystals

Ssu-Che Wang* and Sheng-D Chao

Institute of Applied Mechanics, National Taiwan University, Taipei 106, Taiwan, Republic of China
Email: r98543067@ntu.edu.tw

In this paper, we use the plane wave expansion(PWE)[1] method to calculate the band structures of two-dimensional high dielectric contrast photonic crystals, which are formed by kagome array[2] of solid or hollow dielectric rods[3] connected with dielectric rectangular rods. We scan the material parameter and geometric parameter to find the full band gaps.

First, increasing the number of dielectric rectangular rods in the structure can make the gap wider. The maximum full gap we have found is 42.6% in Fig.1(c)[4] when ε =77, r/a=0.07, w/a= 0.02 . Next, we also find that some structures of hollow dielectric rods can make the gap wider(Fig.1(d)(e)(f)). Follow these, we propose the structure in Fig.1(f) to have widest band gap.

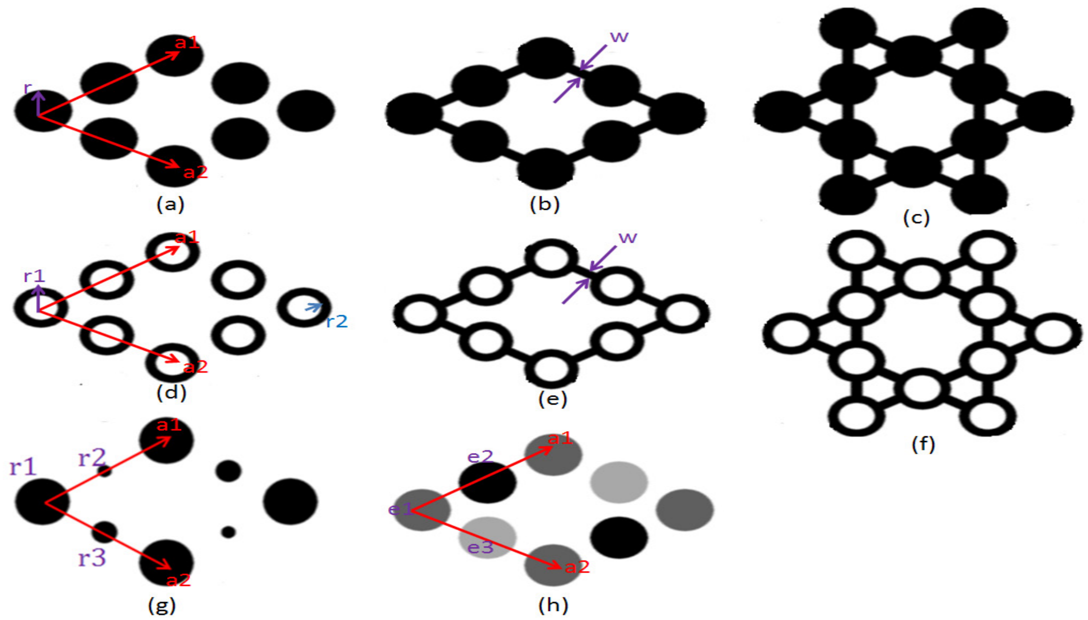

Fig. 1

On the other hand, we consider structure of kagome in different radius or dielectric constants without connected dielectric rectangular rods(Fig.1(g)(h)), which have wider gaps than the structure Fig.1(a) .

Finally, we investigate the relationship of parameters in each structure, and also discuss the relationship of the same parameters in different structures.

(1). K. M. Ho, C. T. Chan, and C. M. Souloulis, *Phys. Rev. Lett.* **65,** 3152 (1990)
(2). A.V. Dyogtyev, I. A. Sukhoivanov, and R. M. De La Rua, *J. Appl. Phys.***107**,013108(2010)
(3).Y. F. Chau, F. L. Wu, Z. H. Jiang, and H. Y. Li, *Optical Society of America*, 2011
(4). S. Sachdev , *Phys. Rev. B*.**45**.21(1991)

Plasmonic Silver Nanoparticles Deposited by a Focused Laser Beam for Biosensing

Takayuki Hironaka*, **Hiroyuki Yoshikawa, Masato Saito, Eiichi Tamiya**

Department of Applied Physics, Osaka University, 2-1 Yamada-oka, Suita, Osaka, Japan
Email: hironaka@ap.eng.osaka-u.ac.jp

Label-free biosensing is of great importance for both fundamental studies in biochemistry and applications in point-of-care diagnostics. Noble metal nanostructures are useful in development of label-free optical biosensors. Receptor biomolecules such as peptides, antibodies, and DNAs can be immobilized on the metal surface according to an easy protocol. Photons and molecules can strongly interact via localized surface plasmon resonance (LSPR) in the vicinity of metal nanostructures. These characteristics of metal nanostructures can be used in biosensing applications. We report novel fabrication methods of plasmonic silver nanostructures using a focused laser beam and its biosensing applications.

Silver nanoparticles (AgNPs) are deposited by focusing a visible laser beam in the silver nitrate solution including a reducing agent. Laser irradiation time necessary for AgNP deposition depends on the species and concentration of reducing reagent. This AgNP deposition by a focused laser beam can be applicable to the optical biosensing because some biomolecules or products due to biochemical reaction act on the reduction of silver ions. By detecting the backscattered light from AgNPs, the deposition process and the spectroscopic property are analysed. Plasmon resonance Rayleigh scattering spectrum of deposited AgNPs is measured by the dark-field microspectroscopy and refractive index dependence of plasmon band is evaluated. In addition, we succeed in fabricating Ag nanostructures in a glass micropipette tip and measuring surface enhanced Raman scattering (SERS) spectra of molecules sucked in the micropipette (Fig. 1). This SERS micropipette could be used for the single cell analysis of intercellular and intracellular signaling molecules.

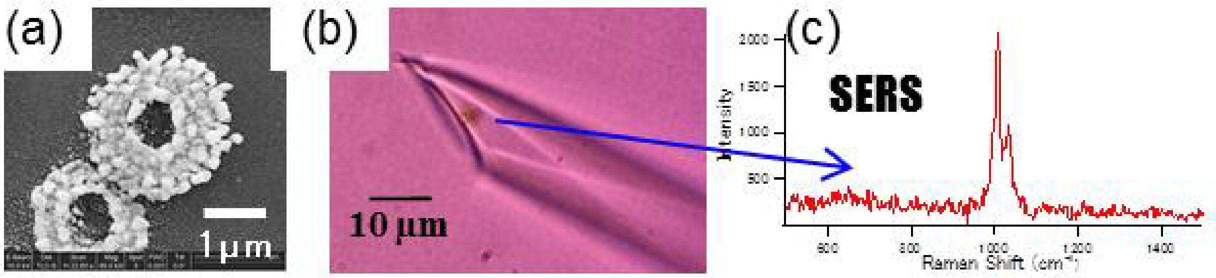

Fig. 1 (a) Ag nanoparticles deposited on a glass substrate. (b) Ag nanoparticles deposited in the end of a glass micropipette. (c) A SERS spectrum from a pyridine solution sucked in the micropipette.

Transmission Properties of Metal-insulator-metal Structure Arrays

Wakana Kubo[1,2]* and **Takuo Tanaka**[1]

[1]*Metamaterials Laboratory, RIKEN Advanced Science Institute, 2-1 Hirosawa, Wako, Saitama, Japan*
[2]*JST, PRESTO*
Email: wakana_kubo@riken.jp

Metal gap structures with a few-nanometer gap are attractive for plasmonic sensors owning to their strong electromagnetic field based on plasmon resonances with gap mode. We had reported the improvement of plasmon sensor sensitivity by using Au double nanopillars with gap, as so-called metal-insulator-metal structure (MIM) [1]. For further increase of sensor sensitivity, we should optimize MIM designs in respect to the gap widths, metal film thickness, and pitches between structures for effective enhancement of electromagnetic fields. In this report, we prepared MIM structure aligned on a flexible film and checked their transmission properties.

MIM structure arrays were simply constructed by laminating and etching thin films with metal and insulator based on the nanocoating lithography[2]. After the preparation of a polymer template (Fig,1(a)), 1st metal layer was coated on the surface (Fig.1(b)). After selective removal of the topmost layer, single nanofin arrays were formed (Fig.1(c)). After the coating and etching of the insulation layer and 2nd metal layer (Fig.1(d,e)), MIM structure arrays were obtained (Fig.1(f), 2). Transmittance of the MIM structure under polarized light was measured.

The MIM structure had several peaks in visible and near-IR region under the linear polarized light irradiation whose E-direction is perpendicular to the longitudinal direction of the MIM arrays (Fig.3). Some peaks shifted to longer-wavelength according to the gap width increase, while the peak around 1650 nm did not shift at all.

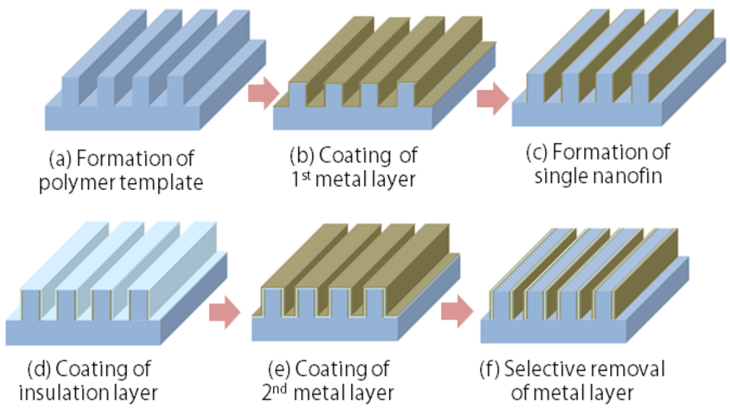

Fig.1 Schematic illustration of the nanocoating lithography technique.

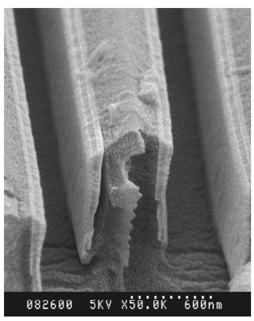

Fig.2 Scanning electron microscope image of MIM structure arrays with 26-nm gap

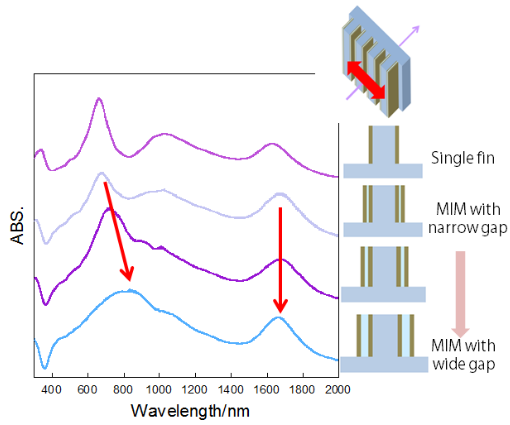

Fig.3 Transmission spectra of MIM structure arrays with various gap widths.

1. Kubo, W.; Fujikawa, S. *Nano Lett.* **2011,** 11, (1), 8-15.
2. Fujikawa, S.; Takaki, R.; Kunitake, T. *Langmuir* **2006,** 22, (21), 9057-9061.

Optimization of *s*-polarization Sensitivity in Apertureless Near-field Optical Microscopy

Yoshiro Ohashi, Yuika Saito and Prabhat Verma

Department of Applied Physics, Osaka University, 2-1 Yamadaoka, Suita, Osaka, 565-0871 Japan

It is a general belief in apertureless near-field microscopy that the so-called *p*-polarization configuration, where the incident light is polarized parallel to the axis of the probe, is advantageous to its counterpart[1,2], the *s*-polarization configuration, where the incident light is polarized perpendicular to the probe axis. While this is true for most samples under common near-field experimental conditions, there are samples which response better to the *s*-polarization configuration due to their orientations. Indeed, there have been several reports that have discussed such samples[4,5]. This leads us to an important requirement that the near-field experimental setup should be equipped with proper sensitivity for measurements with *s*-polarization configuration. This requires not only creation of effective *s*-polarized illumination at the near-field probe, but also proper enhancement of *s*-polarized light by the probe. In this article, we have examined the *s*-polarization enhancement sensitivity of near-field probes by measuring and evaluating the near-field Raleigh scattering images constructed by a variety of probes. We found that the *s*-polarization enhancement sensitivity strongly depends on the sharpness of the apex of near-field probes. We have discussed about the efficient value of probe sharpness by considering a balance between the enhancement and the spatial resolution, both of which are essential requirements of apertureless near-field microscopy.

(1). Moon, P.; Spencer, D.E.; *Van Nost. Reinhold* (1961).
(2). Kawata, S.; Inouye, Y.; Sugiura, T.; *Jap.J.Appl.Phys. PART 2-LETTERS* **33,** L1725-L1727 (1994).
(3). Hartschuh, A.; Sanchez, E.J.; Xie, X.S.; Novotny, L.; *Phys.Rev.Lett.* **90**, 095503 (2003).
(4). Yano, T.; Verma, P.; Saito, Y.; Ichimura, T.; Kawata, S.; *Nature Photo.* **3**, 473-477 (2009).

Optimization of *s*-polarization Sensitivity in Apertureless Near-field Optical Microscopy

Yoshiro Ohashi, Yuika Saito and Prabhat Verma

Department of Applied Physics, Osaka University, 2-1 Yamadaoka, Suita, Osaka, 565-0871 Japan

It is a general belief in apertureless near-field microscopy that the so-called *p*-polarization configuration, where the incident light is polarized parallel to the axis of the probe, is advantageous to its counterpart[1,2], the *s*-polarization configuration, where the incident light is polarized perpendicular to the probe axis. While this is true for most samples under common near-field experimental conditions, there are samples which response better to the *s*-polarization configuration due to their orientations. Indeed, there have been several reports that have discussed such samples[4,5]. This leads us to an important requirement that the near-field experimental setup should be equipped with proper sensitivity for measurements with *s*-polarization configuration. This requires not only creation of effective *s*-polarized illumination at the near-field probe, but also proper enhancement of *s*-polarized light by the probe. In this article, we have examined the *s*-polarization enhancement sensitivity of near-field probes by measuring and evaluating the near-field Raleigh scattering images constructed by a variety of probes. We found that the *s*-polarization enhancement sensitivity strongly depends on the sharpness of the apex of near-field probes. We have discussed about the efficient value of probe sharpness by considering a balance between the enhancement and the spatial resolution, both of which are essential requirements of apertureless near-field microscopy.

(1). Moon, P.; Spencer, D.E.; *Van Nost. Reinhold* (1961).
(2). Kawata, S.; Inouye, Y.; Sugiura, T.; *Jap.J.Appl.Phys. PART 2-LETTERS* **33,** L1725-L1727 (1994).
(3). Hartschuh, A.; Sanchez, E.J.; Xie, X.S.; Novotny, L.; *Phys.Rev.Lett.* **90**, 095503 (2003).
(4). Yano, T.; Verma, P.; Saito, Y.; Ichimura, T.; Kawata, S.; *Nature Photo.* **3**, 473-477 (2009).

GaAs nanowire/ PEDOT:PSS hybrid solar cells with incorporating electron blocking P3HT layer

Jiun-Jie Chao* **and Ching-Fuh Lin**

Graduate Institute of Photonics and Optoelectronics, National Taiwan University, Taipei 106, Taiwan
Email: f94943042@ntu.edu.tw

Organic-inorganic hybrid solar cells have attracted a great deal of interest because they combine both the beneficial properties of organic materials and inorganic semiconductors. Organic materials can provide good light absorption, mechanical flexibility and easy mass-production at a very low cost. Inorganic semiconductors can provide high carrier mobilities and the favorable morphology. Among different morphology of inorganic nanostructures, vertically aligned nanowire array is the most attractive one for photovoltaic applications due to its beneficial properties- anti-reflection ability and light-trapping capability. To date, a variety of vertically aligned nanowires have been studied on the hybrid photovoltaic applications. However, relatively few hybrid solar cells involving III–V inorganic nanowires have been investigated. H Bi et al. firstly report the MBE-grown GaAs nanowire/ poly(3-hexylthiophene) (P3HT) hybrid solar cell[1]. Later, Giacomo Mariani et al. report the MOCVD-grown GaAs nanopillar/ P3HT hybrid solar cell[2]. Both achieved energy conversion efficiency of only less than 1.5 %.

In this report, we demonstrate a new type of hybrid solar cell based on a heterojunction between vertically aligned GaAs nanowires and poly(3,4-ethylenedioxythiophene): poly(styrenesulfonate) (PEDOT:PSS) with incorporating electron blocking P3HT layer. The cell structure is shown in Fig. 1(a). Instead of using bottom-up approach, the fabrication of GaAs nanowire in our work adopts the top-down approach, which combines low-cost nanosphere lithography and dry etching with high quality bulk single-crystal wafer. As shown in Fig. 1(b), the results reveal that the fabricated cell exhibits a PCE of 9.1 % with short circuit current density (J_{sc}) of 20.2 mA cm^{-2} and open circuit voltage (V_{oc}) of 0.65 V under 1 sun simulated AM1.5 G solar illumination.

(a)

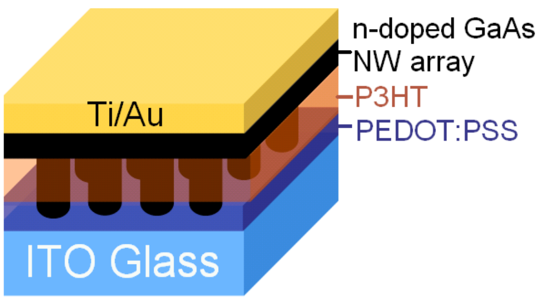

(b)

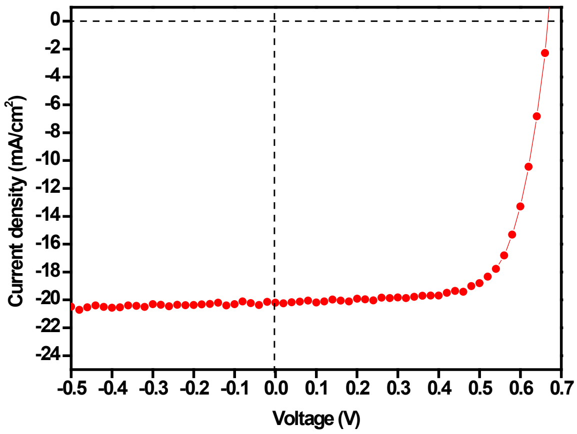

Fig. 1 (a) The cell structure of GaAs nanowire/ PEDOT:PSS hybrid solar cells with incorporating electron blocking P3HT layer;

Fig. 1 (b) The J-V characteristics measured under 1 sun simulated AM1.5 G solar illumination.

(1). Bi, H. et al. *Nanotechnology* **2009**, *20*, 465205.
(2). Mariani, G. et al. *Appl. Phys. Lett.* **2010**, *97*, 013107.

Nano-spectroscopy with plasmonic antennas

Prabhat Verma*

Department of Applied Physics, Osaka University, Suita, Japan
Email: verma@ap.eng.osaka-u.ac.jp

Optical spectroscopy in the visible region is a very important approach, not only to characterizing various kind of samples, but also to understand many basic physical or chemical properties of these sample. This is because most of the naturally existing samples that we interact with in day-to-day life have electronic and vibrational energies that are similar to the energies carried by visible light (from near-UV to near-IR). Therefore, visible light can interact efficiently with the intrinsic properties of the sample, and spectroscopy in visible range can fetch rich information about the sample. However, interaction of light with matter is usually a weak phenomenon. For example, when a sample is illuminated with a particular light source, only one in a million photons undergoes Raman scattering. This is particularly important for nanomaterials with extremely small sample volumes, where the strength of optical scattering becomes very weak. Hence, in order to observe scattering from nanomaterials, one of the important requirements is to enhance the scattering, so that even weak scattering can become observable under usual experimental conditions.

Another issue in spectroscopy at nanoscale is that the wave nature of light prevents it to get focused in a space smaller than half of its wavelength, a phenomenon known as the diffraction limit. Therefore, visible light cannot be focused into a space smaller than about 200~300 nm. This size is much larger than most of the nanomaterials that one would like to study. Therefore, another important requirement for optical nano-spectroscopy is to confine the light field into nanoscale, so that one may obtain nano-sized spatial resolution. Both enhancement and confinement of light field can be achieved by utilizing plasmonic antennas, which are nothing but metallic nanostructures with specific shapes and sizes. Here, we will discuss about optimization of the antenna for better confinement and enhancement of light, and will show some results of enhanced and confined spectroscopy at nanoscale. We will also show some examples of optical imaging through plasmonic antennas, where we can achieve very high spatial resolution, far beyond the diffraction limit.

(1). Saito, Y.; Ohashi, Y.; Verma, P. *Int. J. Optics.* **2012**, *(in Press)*.
(2). Verma, P.; Ichimura, T.; Yano, T.; Saito, Y.; Kawata, S. *Laser & Photonics Rev.* **2010**, *4*, 548.
(3). Yano, T.; Verma, P.; Saito, Y.; Ichimura, T.; Kawata, S. *Nature Photon.* **2009**, *3*, 473.
(4). Kawata, S.; Inouye, Y.; Verma, P. *Nature Photon.* **2009**, *3*, 388.

Directional Thermal Radiation at Terahertz Region by Using Spoof Surface Plasmon

Yosuke Ueba*[1] **and Junichi Takahara**[1,2]

[1]*Department of Applied Physics, Osaka University, Osaka 565-0871, Japan*
[2]*Photonics Advanced Research Center, Osaka University, Osaka 565-0871, Japan*
Email: ueba@ap.eng.osaka-u.ac.jp

For the terahertz fingerprint of 1~3 THz, continuous wave sources with a simple structure are needed. In this paper, we report a terahertz thermal radiation emitter from a metamaterial by using the spoof surface plasmon (spoof SP). A thermal radiation source such as an incandescent bulb has a broad spectrum depending only on Planck's law. However, thermal radiation can be controlled by means of various modes on the surface structure[1,2,3]. Effective surface waves in a metamaterial called spoof SP can be controlled artificially in the metal microcavity array[4]. Thus, it is possible to expand the idea of surface plasmon polaritons to the low-frequency such as terahertz or mid-infrared region, without limitations of material properties.

We theoretically studied the thermal radiation from metal microcavity arrays by using finite-difference time-domain method according to Kirchhoff's law. Typical simulated result is shown in Fig. 1. We achieved that the spoof SP on the metal microcavity array selectively enhanced the thermal radiation at 3 THz with the full width at half maximum of Δf = 70 GHz[5]. As shown in Figs. 2(a) and 2(b), the sidelobe of the thermal emission was much smaller than the vertical emission. We stress that the angular distribution of the radiation was highly directional to normal direction with an angular width of 0.6°. Moreover, we found the coupling mechanism between vertical thermal radiation and the spoof SP in non-radiation mode. It was expected to achieve terahertz sources with simple structures compared to the other sources, such as quantum cascade laser. The thermal radiation source is a good candidate as a new terahertz emitter for spectroscopy or medical and environmental applications.

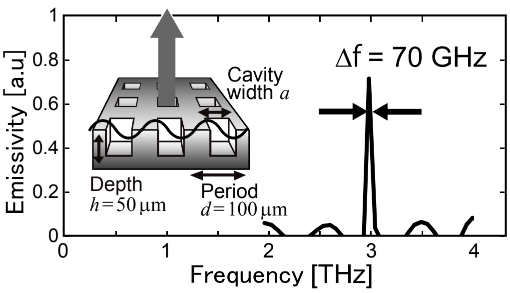

Fig. 1. Vertical emittance spectrum.

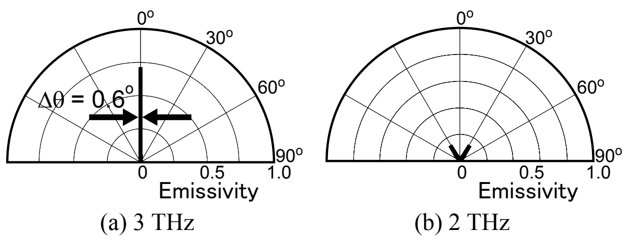

Fig. 2. Polar plots of the emissivity.

(1). P. J. Hesketh; J. N. Zemalr; B. Gebhart, *Nature* **1986,** *324*, 549.
(2). J.J. Greffet; R. Carminati; K. Joulain; J.P. Mulet; S. Mainguy; Y. Chen, *Nature* **2002,** *416*, 61-64.
(3). F. Kusunoki; T. Kohama; T. Hiroshima; S. Fukumoto; J. Takahara; T. Kobayashi, *Jpn. J. Appl. Phys.* **2004,** *43*, 5253.
(4). J. B. Pendry; L. Martin-Moreno; F. J. Garcia-Vidal, *Science* **2004,** *305*, 847.
(5). Y. Ueba; J. Takahara; T. Nagatsuma, *Opt. Lett.* **2011,** *36*, 6.

Gap-enhanced silver substrate for efficient SERS detection

Yu-Chun Lu, Yi-Ming Jiang, Jhe-Yi Liao, Yu-Ju Hung*

Department of Photonics, National Sun Yat-Sen University, Kaohsiung 804, Taiwan
Email: yjhung@ mail.nsysu.edu.tw

Surface-Enhanced Raman Scattering (SERS) on silver island film has been investigated for a long time. The main issues delved are in the different film process parameters and different nano-strucutures[1,2,3]. In order to clarify the mechanisms of SERS on the gap-enhanced silver substrate, we propose a new technique with substrate bending during thermal evaporation. In this case the fractal film forms different gap sizes and density under the same evaporation operation. The target of SERS detection here is the surface carbonation. We take the characteristic Raman peaks of amorphous carbon in 1340 and 1580(cm^{-1}) as the reference position[4]. Since we have compared the 30nm-thick Ag film with fractal surface and smooth formation, only the island surface one has carbon signal in a short exposure period. While the carbon contamination of these two studied by energy dispersive spectrometer (EDS) are in the same level. Therefore, the carbon signal we measured here is mainly caused by gap-enhanced SERS.

Substrates with different dimensions of glass pads underneath show different degree of bending situations and possess different island gap distributions. Here we show three sizes of glass pads：0.4×0.4, 0.8×0.8 and 1.2×1.2(cm^2), the film morphology under different bending status has been investigated by SEM shown in Fig. 1. The optical measurement system used here is 3D confocal Raman microscope (Nanofinder 30). Fig. 2(A) is the Raman spectrum of 30nm Ag island film without glass pad. The average Raman intensity ratio $I_{with\ pads}/I_{flat}$ between the bending samples over the controlled one (fractal surface without bending) is shown in Fig. 2(B). The result has shown that the Raman intensity has direct relationship with the gap area. For the sample on the 0.8×0.8(cm^2) pad, the film morphology looks similar to the one on 1.2×1.2(cm^2) pad. Although the film morphology in Fig. 1(B) looks similar to the status on the film without bending, the Raman intensity showed a lower level, which somehow indicates that the bending might causes stress which affects the Raman scattering efficiency. One thing for sure is that the film stress doesn't cause Raman peaks shift to other values.

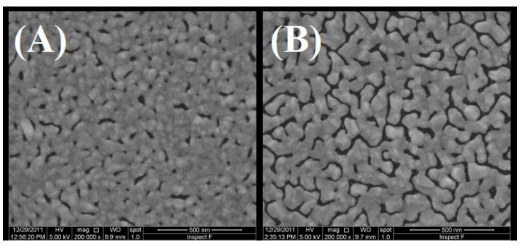

Fig. 1 : SEM image of 30nm silver island film deposited with glass pad area (A) 0.4×0.4(cm^2), (B) 1.2×1.2(cm^2). The image of 0.8×0.8 is similar to 1.2×1.2, not shown.

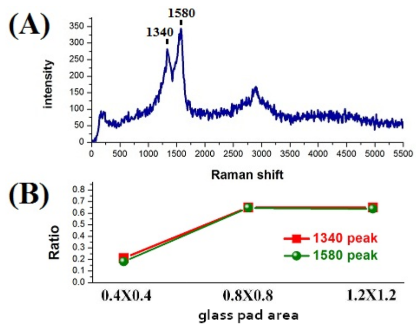

Fig.2 : (A) Raman spectrum of 30nm Ag island film without glass pad . (B) The average Raman intensity ratio between the bending samples over the controlled one (fractal surface without bending).

(1)Vicki L. Schlegel and Therese M. Cotton*, *Anal. Chem.*1991 , 63,241-247
(2)D. A. Weitz, S. Garoff, and T. J. Gramila, *Opt. Lett*. 7, 168-170 (1982)
(3)Huigao Duan, Hailong Hu, Karthik Kumar, Zexiang Shen, Joel K.W.Yang*, *ACS Nano*, *5*(9), 2011, 7593–7600
(4)Paul K. Chu, Liuhe Li, *Mater. Chem. Phys.* 96 (2006) 253–277

Fabrication of multiple crystalline Si thin films via metal-assisted chemical etching

Tzu-Ching Lin[1], **Shu-Chia Shiu**[2], **and Ching-Fuh Lin**[1, 2, 3]

[1]*Graduate Institute of Electronics Engineering,* [2]*Graduate Institute of Photonics and Optoelectronics,*
[3]*Department of Electrical Engineering, National Taiwan University, Taipei 106, Taiwan (R.O.C.).*
E-mail address: cflin@cc.ee.ntu.edu.tw

Saving materials is important to reduce cost in photovoltaic industry. In crystalline silicon photovoltaic industry, high wafer cost has driven the study of thin film or ultra-thin film crystalline silicon materials. One way people usually apply for the absorber silicon is by CVD [1]. However, the CVD machines for mass production are still very expensive. In 2011, Shiu et al. fabricates crystalline thin films by low-cost all-solution process [2]. Nevertheless, the substrate reusing was not demonstrated. In this paper, we propose a substrate-reusing method by metal–assisted etching to achieve multiple single-crystalline thin-film lift-offs. Substrates can be reused for another crystalline thin film. The process is done in solution process and in room temperature. Last but not least, nanoholes are formed in the fabricated crystalline thin films, giving much more excellent light-trapping than planar Si [2], so additional anti-reflection coating is not needed.

The experimental process was as follows. N-type (100) silicon wafer was used during the process. The wafer was cleaned under ultrasonic treatment in ACE and IPA. There were three main steps for fabrication of crystalline thin film. First, the surface of wafer was deposited with Ag nanoparticles in AgNO3/HF aqueous solution. Second, vertical nanoholes were formed on top of the Si wafer when the wafer was immersed into HF/H_2O_2 aqueous solution. Third, the entire crystalline thin film was formed and lifted off from Si wafer in a solution with a different etching condition from that of the second step. This was the first fabrication of our crystalline thin film. Afterwards, we cleaned the used wafer from the first thin film fabrication by ultrasonic cleaning in ACE and repeated the same steps in first thin film fabrication. The second crystalline thin film was then obtained from the same substrate.

Fig.1 (a) shows the result of the first thin film lift-off from silicon wafer. In the picture we can see a uniform crystalline thin film with thickness about 6.5 μm. Fig.1 (b) shows the result of the second thin film lift-off from silicon wafer. The thin film resembles the results of the first thin film in Fig. (a). There are numerous nanoholes on the cross-section of the thin film. A gap between the thin film and the wafer leads to the lift-off of the crystalline thin film. Our experiment demonstrates the possibility of multiple lift-offs from a single Si wafer without any epitaxial layer grown by vacuum apparatuses. It is done using very low-cost all-solution process. The material consumption can be reduced to less than 1/10 of current crystalline-Si photovoltaic devices, giving the promise of very low-cost Si-based solar energy comparable to fossil energy in the future.

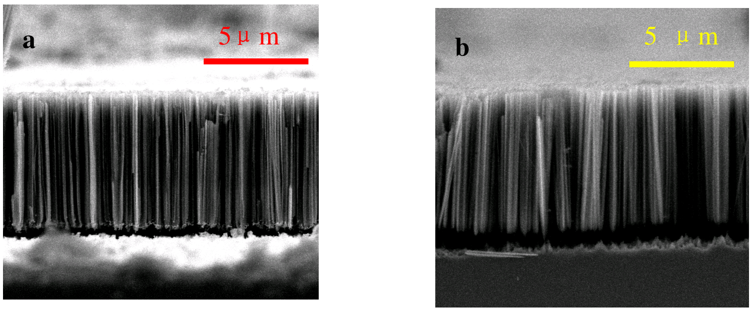

Fig.1 SEM cross-sectional view of: (a) the first crystalline Si thin film lift-off from Si wafer (b) the second thin film lift-off

(1). Petermann, J. H.; D. Zielke, et al. Prog. Photovolt: Res. Appl. 2012, 20, 1, 1-5.

(2). Shiu, S.-C.; Hung, S.-C., et al. J. Electrochem. Soc., 2011, 158, 2, D95-D98.

Vertical magnetization manipulation method for magnetic nanodot withmagnetic force microscopy

Kei Maehara, Kentaro Toyoki, Hikaru Nomura and Ryoichi Nakatani

Department of Materials Science and Engineering

Graduate School of Engineering, Osaka University, 2-1 Yamada-oka, Suita, Osaka, Japan

Email: nomura@mat.eng.osaka-u.ac.jp

Logic devices based on magnetic nanodots has advantage of low dissipation energy, high integration density, and high-speed operation. Recently, we proposed NAND/NOR magnetic logic gate (MLG)[1]. In these devices, magnetizations of the dots are assumed to be a single domain state. If both of single domain state and vortex state can be used, we can fabricate highly functional circuit. However, it is difficult to change between each state without using a local magnetic field. Recently, a magnetization manipulation method based on magnetic force microscopy (MFM) was proposed by X. Zhu, et al [2]. With a localized stray field from a MFM tip, the magnetization states of the nanodots are switched depending on the scanning direction of the MFM tip. However, a threshold position of the tip to switch the magnetization state is not clarified yet. In this study, we perform force mapping measurement with MFM to clarify the threshold position of the magnetization manipulation with various sizes of nanodots.

As a cylindroid nanodots, various size of Ni-20at.%Fe dots with thickness of 20 nm were fabricated on a Si(100) substrate by electron-beam lithography, ion beam sputtering, and a lift off technique. All experiments were performed in a vacuum condition at room temperature with a commercial MFM (SII-A300). To control the tip position, we developed original MFM controller with LabVIEW FPGA/Real time OS. In force mapping measurements, the MFM tip height was vertically moved (force curve measurement) at various lateral positions. Before the force curve measurements, the magnetizations of the nanodots were initialized to take a single domain state with external magnetic field.

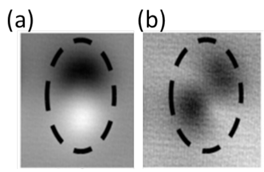

Fig. 1 MFM images of (a) initial state and (b) after the magnetization manipulation

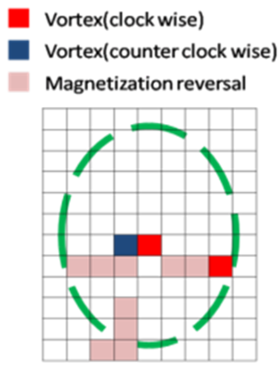

Fig. 2. Dependence of magnetic domain state on lateral tip positions.

Figure 1 shows one of the magnetization manipulation results. After the force curve measurements, the magnetization state of the dot was changed from single domain state to vortex state. Fig. 2 shows dependence of the magnetic domain state on lateral tip positions. From these results show that we can control the magnetic domain state of nanodots with appropriate lateral tip position. With these methods, we can increase functionality of magnetic devices such as MLG.

[1] S. A. Haque, M. Yamamoto, R. Nakatani, Y. Endo, *J. Magn. Magn. Mater*. **282** (2004) 380.

[2] Xiaobin Zhu, P.Grutter, V.Metlushko and B.llic. *J.Appl.Phys.***91** (2002) 7340 .

Simulation study of magnetic quantum dots cellular automata shift register

Soichiro Miura, Hikaru Nomura and Ryoichi Nakatani

Department of Materials Science and Engineering

Graduate School of Engineering, Osaka University, 2-1 Yamada-oka, Suita, Osaka, Japan

Email: nomura@mat.eng.osaka-u.ac.jp

Magnetic Quantum dots Cellular Automata (MQCA)[1] consists of elliptic nano-magnets, which is small enough to take a single domain state. Digital information of "0" and "1" are stored as a magnetization direction. The MQCA can transfer and calculate digital information[2] via magneto-static interactions between the nano-magnets. In this study, we propose a MQCA shift register, which can operate with a uniform magnetic field, by using micromagnetic calculation.

Figure 1 shows a schematic diagram of MQCA shift register. D_n and B_n are data dots and buffer dots, respectively. When an alternating external magnetic field is applied to be parallel to the easy axis of the D_n or B_n, the data are transfered from D_n to B_n or B_{n-1} to D_n, respectively. Thus by switching external magnetic field directions, the data can be shifted. The micromagnetic calculation is performed by OOMMF. The intrinsic parameters used in the simulations are: satureation moment Ms = 800 kA/m, cell size of 5 × 5× 5 nm^3, damping constants α = 0.5 and exchange constant A = 13 $\times 10^{-12}$ J/m. The geometry of the shift register are: a = 30 nm, b = 60 nm, thickness 20 nm, r = 151.5 nm and θ = 0 deg.. The amplitude of the external magnetic field is 53 kA/m.

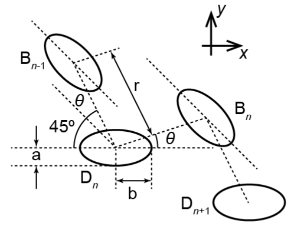

Fig. 1. Schematic of MQCA shift register

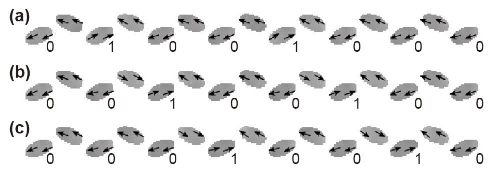

Fig. 2. Simulation results of 8-bit MQCA shift register. (a) initial states and (b,c) bit shift operation results.

Figure 2 shows simulation results of the 8-bit shift register. From these results, we can say that the MQCA shift register can be feasible. To consider the suitable geometry for the bit shift operation, we perform simple numerical simulation with macro-spin model. Fig. 3 shows a range of the external magnetic field amplitude (solid line) and suitable position of the buffer dots (dotted line), depending on the stray field strength h_s normalized with anisotropy field of the dots. With $h_s \sim$ 0.1 and $\theta \sim$ 10, we can get a maximum range of the external magnetic field. With these methods, we can define a distance and direction of the data transfer.

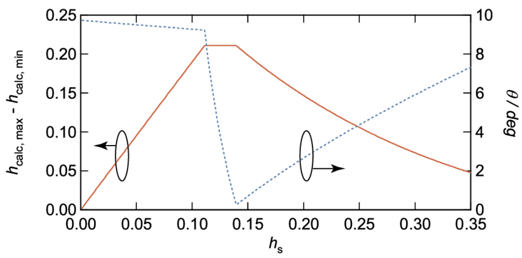

Fig. 3. The dependence of range of the external magnetic field amplitude and the suitable position of the buffer dots on the stray field strength.

With the MQCA shift register, we can fabricate complicated circuits with multiple MQCA gates.

[1] R. P. Cowburn and M. E. Welland, *Science*, **287**, 1466-1468 (2000).

[2] S. A. Haque, et al., *J. Magn. Magn. Mater.* **282** 380-384 (2004).

Silicon Nanowire/Organic Hybrid Solar Cell with High Efficiency of 9.47%

Hong-Jhang Syu, Shu-Chia Shiu, and Ching-Fuh Lin

Graduate Institute of Photonics andOptoelectronics , National Taiwan University, Taipei 106, Taiwan
Graduate Institute of Electronic Engineering , National Taiwan University, Taipei 106, Taiwan
Department of Electrical Engineering , National Taiwan University, Taipei 106, Taiwan
Email: cflin@cc.ee.ntu.edu.tw

To reduce the high cost, high temperature, and high energy consumption manufacturing procedures of conventional silicon p-n junction solar cells, the solution process possible organic materials have been drawn into the photovoltaic devices to form inorganic/organic hybrid solar cells. For instance, n-type silicon (n-Si)/poly-(CH3)3Sicyclooctatetraene[1], n-Si/tetraphenylporphyrin[2], p-type silicon (p-Si)/4-tri-cyanovinyl-N,N-diethylaniline[3], amorphous silicon (a-Si)/poly(3-hexylthiophene)[4], n-Si/poly(3,4-ethylenedioxythiophene):poly(styrene-sulfonate)[5], n-Si/polyaniline[6], and n-Si/phthalocyanine[7]. However, all of them only generate efficiencies lower than 5%.

Here we fabricate n-type silicon nanowires (SiNWs) normal on n-Si wafer to make light bounce back and force between SiNWs to increase photon trapping[8], and produce more photo-current. Also, the silicon nanowires enlarge the junction surface to increase the probability of carrier separation. On the other hand, the organic material we used is poly(3,4-ethylenedioxythiophene): poly(styrene-sulfonate) (PEDOT:PSS), which has the function of both hole transport and electron blocking in the system. That is because PEDOT:PSS has highest occupied molecular orbital (HOMO) energy of 5.0 eV and lowest unoccupied molecular orbital (LUMO) energy of 3.5 eV. The HOMO level is near the valence band energy of Si. Contrarily, LUMO level of PEDOT:PSS is higher than the conduction band energy of Si of 4.05 eV. Thus PEDOT:PSS can transport holes to anode, and block electrons from transporting toward anode while combining with Si.

The fabricated SiNW/PEDOT:PSS solar cells with high power conversion efficiency (PCE) of 9.47%, current density (J_{sc}) of 26.81 mA/cm^2, and open circuit voltage (V_{oc}) of 0.540 V, while the control device of planar-Si/PEDOT:PSS solar cell only has PCE of 2.62%, J_{sc} of 13.62 mA/cm^2, and V_{oc} of 0.514 V.

(1) Sailor, M. J.; Ginaburg, E. J.; Gorman, C. B.; Kumar, A.; Grubbs, R. H.; Lewis, N. S. *Science*, **1990**, *249*, 1146–1149.
(2) El-Nahass, M. M.; Zeyada, H. M.; Aziz, M. S.; Makhlouf, M. M. *Thin Solid Films*, **2005**, *492* , 290–297.
(3) El-Nahass, M. M.; Zeyada, H. M.; Abd-El-Rahman, K. F.; Darwish, A. A. A., *Sol. Energy Mater. Sol. Cells*, **2007**, *91*, 1120–1126.
(4) Gowrishankar, V.; Scully, S. R.; McGehee, M. D.; Wang, Q.; Branz, H. M., *Appl. Phys. Lett.*, **2006**, *89*, 252102.
(5) Williams, E. L.; Jabbour, G. E.; Wang, Q.; Shaheen, S. E.; Ginley, D. S.; Schiff, E. A., *Appl. Phys. Lett.*, **2005**, *87*, 223504.
(6) Wang, W.; Schiff, E. A., *Appl. Phys. Lett.*, **2007**, 91, 133504.
(7) Lin, C. H.; Tseng, S. C.; Liu, Y. K.; Tai, Y.; Chattopadhyay, S.; Lin, C. F.; Lee, J. H.; Hwang, J. S.; Hsu, Y. Y.; Chen, L. C.; Chen, W. C.; Chen, K. H., *Appl. Phys. Lett.*, **2008**, *92*, 233302.
(8) Hu, L.; Chen, G.; *Nano Lett.*, **2007,** 7, 3249–3252.

Tip-enhanced Raman imaging and analysis of crossed nanotube junctions

Yoshito Okuno[1], Shota Kuwahara[2], Kazumasa Uetsuki[1,3], Takaaki Yano[1,3], Prabhat Verma[1,3], Satoshi Kawata[1,3,4]

[1]Department Of Applied Physics , Osaka University. Osaka 565-0871 Japan
[2]Department Of Applied Chemistry , Chuo University. Tokyo 112-8551 Japan
[3]CREST, Japan Science and Technology Agency, Department of Applied Physics, Osaka University, Osaka 464-8602, Japan
[4]RIKEN, Advanced Science Institute Nanophotonics Laboratory. Saitama 351-0198, Japan
Address 2-1 Yamadagaoka, Suita-shi, Osaka, Japan
Email: okuno@ap.eng.osaka-u.ac.jp

Tip-enhanced Raman spectroscopy (TERS) has been recognized as a powerful tool to optically analyze carbon nanotubes (SWCNTs) on a nanometer scale [1]. TERS has been so far utilized to characterize localized defects and change of chirality in nanotube, and even to measure local distribution of molecules encapsulated in nanotube [2]. In this time, we show TERS imaging and analysis of SWCNTs including a junction of two SWCNTs crossing with each other on their own structures. The crossed CNTs were formed in the process of dispersing alcohol-diluted solution of SWCNT onto a glass substrate, which was confirmed by the topographic image as is shown in Fig. 1(a). Tip-enhanced Raman spectroscopic image was performed on around cross part of SWCNTs with a silver-coated tip and excitation wavelength of 488 nm. Figure 1(b) shows the TERS image of the G-band intensity, revealing local intensity decreasing at the junction of SWCNTs which is arrowed. This was due to local change of the resonant Raman condition caused by local deformation of SWCNTs at the junction and bundle parts. And in our presentation, we will discuss deformation-induced frequency shift of the Raman bands (the radial breathing mode, the D-band and the G-band) as well.

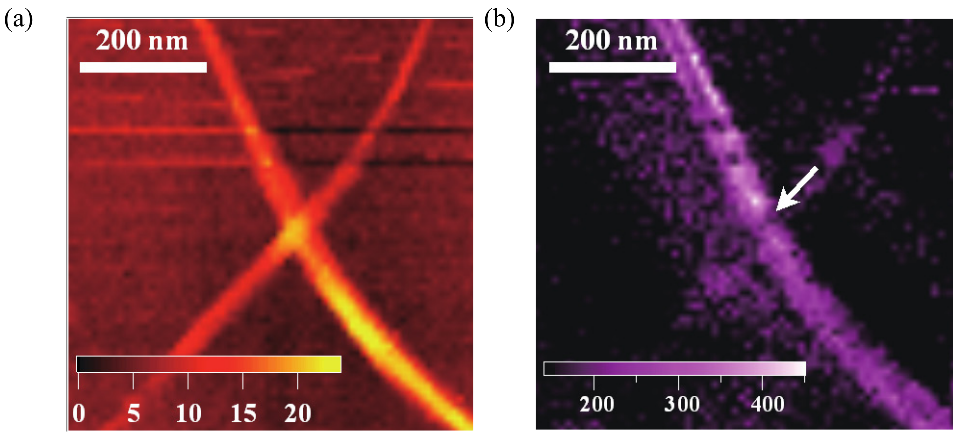

Fig.1

(a)AFM image of the crossed SWCNTs (b) simultaneously-obtained TERS image

Reference:
[1] Hayazawa et.al., Chem. Phys. Lett., Vol. 376, pp. 174-180, **2003**
[2] Neil Anderson et.al., Nano Lett., Vol. 7, No. 3, **2007**

Cascade stub resonator in V-groove Plasmon waveguide

Naohiro Kamon[*], Masanobu Haraguchi, and Toshihiro Okamoto

Department of Optical Science and Technology, University of Tokushima, Tokushima 770-8506, Japan
E-mail:kamon@opt.tokushima-u.ac.jp

Plasmonic waveguides have attracted much attention because they have a potential to guide light with a tiny beam size beyond the so-called diffraction limit. It is possible to develop a functional miniaturized optical device, such as a wavelength filter and optical modulator, by using a resonator structure in plasmonic waveguide. In this study, We have used stub structure[1] ; we have fabricated a kind of Fabry-Perot resonator in V-groove Plasmon waveguide with two stubs set in a separated position. Note that we named this structure cascade stub resonator. And we have evaluated its transmission characteristics.

A stub structure has a branch of the waveguide with a finite length. Transmission at a wavelength is controllable by adjusting the length of a stub, so that it can be employed as a mirror. When two stub structures are installed in plasmonic waveguide, it will work as a Fabry-Perot resonator. Compared with the case of single stub structure, We expect that Q value can be raised up to 400 times.

At first, we deposited Ag film with 2.5 μm thick on silicon substrate in vaccum. Next we formed the cascade stub resonator by FIB processing. In Fig1, a typical Scanning Ion Microscopy (SIM) image is shown as a plenary view. In order to excite a plasmonic wave, we employed the end-fire method as shown in Fig.2. As the light source, the linearly polarized LD was employed, and its wavelength was 1.31 μm in vacuum. We observed optical image of the light scattered from the plasmonic structure and evaluated the intensity of the light scattered at output port.

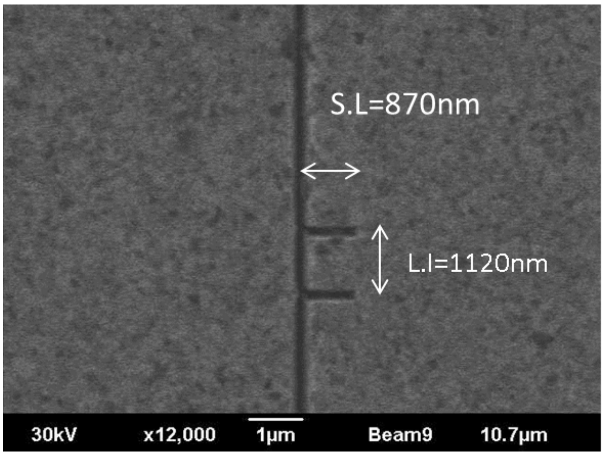

Fig1.SIM image of cascade stub resonator

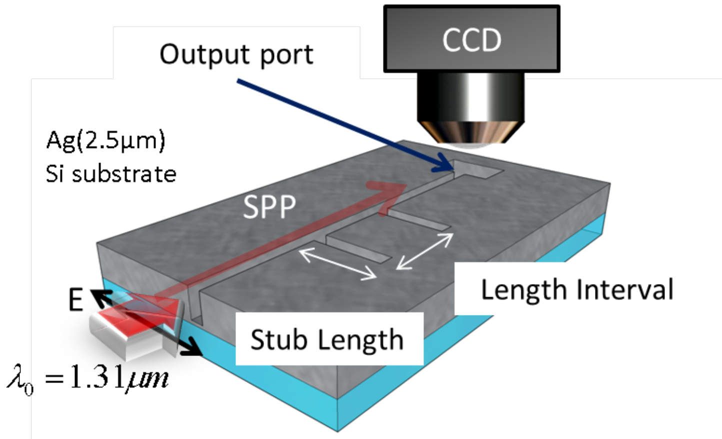

Fig2. Image of optical experiment

References

(1). Matsuzaki, Y.; Okamoto, T.; Haraguchi, M.; Fukui, M.; Nakagaki, M. Optics Express **2008** 16, 16314.

Investigations of carrier mobility and diffusion length through the impedance-voltage characteristics in organic light emitting diodes

I-Wen Wu[1], Po-Sheng Wang[1], Wei-Hsuan Tseng[1], and Chih-I Wu[2]

1. Graduate Institute of Photonics and Optoelectronics, National Taiwan University, Taipei 106, Taiwan.
2. Graduate Institute of Photonics and Optoelectronics and Department of Electrical Engineering, National Taiwan University, Taipei 106, Taiwan

The impedance versus voltage (Z-V) characteristics were used to investigate the carrier mobility and the diffusion length of cathode structures in organic light emitting diodes (OLEDs). With the existence of the accumulation charges at the organic layers interfaces, the Z-V characteristics present a particular transition before the device turns on and the voltage at where the transition occurs is dependent on the film thickness and the density of the accumulation charges. Devices with systematically varied film structures, including various cathode structures and different thicknesses of the electron transport layers (ETLs) were investigated. The results showed that the impedance transition happens at a higher voltage bias in the devices with an electron injection layer, which may result from the diffusion of the electron injection materials and the decrease of the effective thickness providing the electrical potential difference.

The devices with several combinations of hole transport layers (HTLs) and ETLs were also studied and the Z-V characteristics of the investigated devices are shown in Fig.1. The results indicate that there is an extra impedance transition only in the devices with the hole mobility in the HTL much larger than the electron mobility in the ETL. Thus the difference between the carrier mobilities in the HTL and the ETL can be surveyed through the Z-V characteristics of OLEDs, and this property makes the Z-V characteristics a potential tool to compare the hole and electron mobilities in the carrier transport materials.

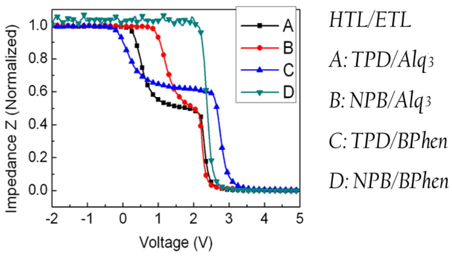

Fig. 1 The impedance-voltage characteristics of OLEDs with various HTL and ETL combinations.

(1). S. Berleb, W. Brütting, and G. Paasch, *Org. Elec.* **2000,** *1*, 41
(2). W. Brütting, S. Berleb, and A. G. Mückl, *Org. Elec.* **2001,** *2*, 1

Enhancement of Current Injection in Organic Light Emitting Diodes with Sputter-treated Molybdenum Oxides as Hole Injection Layers

Po-Sheng Wang[1], **I-Wen Wu**[1], **Wei-Hsuan Tseng**[1], **Mei-Hsin Chen**[2] **and Chih-I Wu**[1,*]

1. Department of Electrical Engineering and Graduate Institute of Photonics and Optoelectronics, National Taiwan University, Taipei, Taiwan 10617, Republic of China

2. Department of Opto-Electronic Engineering, National Dong Hwa University, Hualien 974, Taiwan

Email: f95941029@ntu.edu.tw

Molybdenum oxide (MoO_3) has been widely used in organic light emitting diodes (OLEDs) to provide superior hole injection efficiency. The origins of assistance in hole injection from MoO_3 hole injecting layers are the lowering of injection barrier and formation of gap states between valence band edge of MoO_3 and the Fermi level of electrodes when NPB molecules are deposited on MoO_3 layers[1]. These gap states enhance the conductivity of MoO_3 and provide transition paths of carrier to assist the injection of hole from indium tin oxide (ITO) anodes to NPB layers[2]. To enhance the metallic characteristics of MoO_3 and facilitate better hole injection directly, in-situ Argon ion sputter is incorporated with the fabrication process of OLEDs in this work. When treating the surface of MoO_3 with slight Argon sputtering, ion bombardment removes the bonding oxygen atoms in MoO_3 layers. As a result, the oxidation states of molybdenum atoms in MoO_3 are reduced. The enhancement of current density in OLEDs is effectively achieved by treating MoO_3 layers with slight argon sputtering. After sputter treatment for 10 seconds, the modified MoO_3 layers provide improved current injection efficiency, resulting in better current density which is about ten times higher than that of the reference devices A as shown in Fig.1. Ultraviolet and X-ray photoemission spectra provide evidences that molybdenum atoms are reduced to lower oxidation states after sputter treatment due to the removal of oxygen atoms.

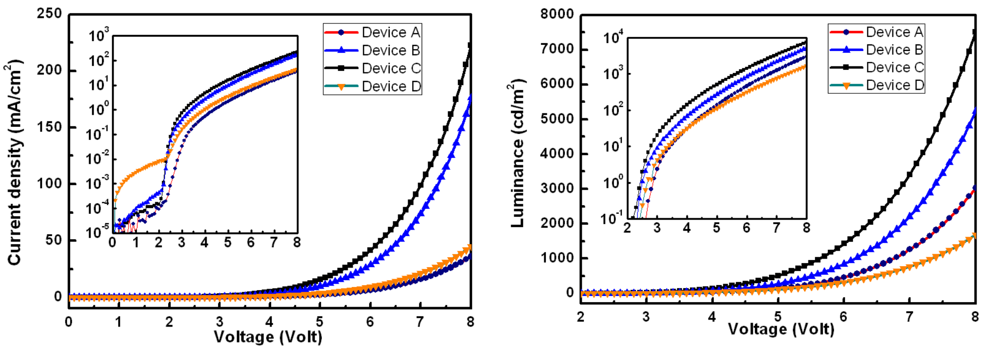

Fig. 1

(1). C. I. Wu, C. T. Lin, G. R. Lee, T. Y. Cho, C. C. Wu, and T. W. Pi, J. Appl. Phys. **105**, 033717 (2009)

(2). C. T. Lin, C. H. Yeh, M. S. Chen, S. H. Hsu, C. I. Wu, and T. W. Pi, J. Appl. Phys. **107**, 053703 (2010)..

Investigations of Efficiency Improvements in Poly(3-hexylthiophene) Based Organic Solar Cells Using Calcium Cathodes

Wei-Hsuan Tseng[a] , Mei-Hsin Chen[b*], Jeng-Yu Wang[a], Chun-Tse Tseng[a], and Chih-I Wu[a*]

[a]*Department of Electrical Engineering and Graduate Institute of Photonics and Optoelectronics, National Taiwan University, Taipei 106, Taiwan*

[b]*Department of Opto-Electronic Engineering, National Dong Hwa University, Hualien 974, Taiwan*

Email: chihiwu@cc.ee.ntu.edu.tw (C.I. Wu) and meihsinchen@mail.ndhu.edu.tw (M.H. Chen)

Bulk-heterojunction (BHJ) polymer solar cells using poly(3-hexylthiophene) (P3HT) as an electron donor polymer and [6,6]-phenyl-C61-butyric acid methyl ester (PCBM) as an electron acceptor have attracted tremendous attention due to the simple processing steps and relatively high power conversion efficiency (PCE)[1,2,3]. It has been reported that calcium (Ca) combined with the P3HT:PCBM active layer is one of the best candidates since it tends to develop an ohmic-contact at the active layer/cathode interface, which theoretically will perform better PCE value in devices.[4] However, in practical device fabrications, some reports indicate that the vapor deposition of high-energy alkaline earth metals like Ca on polymer surfaces might induce chemical reactions, which will also significantly affect the performance of devices.[5,6] Therefore, the mechanisms of improvements in devices are more chemically complex and have not been fully explored in the previous literatures.

In this work, we propose the mechanisms of the efficiency improvement in P3HT:PCBM based organic solar cells using Ca as cathode. The electronic properties and chemical interactions between P3HT:PCBM blend active layer and Ca cathode were studied via ultraviolet and x-ray photoemission spectroscopy (UPS and XPS). UPS results show that the HOMO level of P3HT is pulled down by 0.8 eV respect to the Fermi level after 1.5-nm Ca deposition, which implies that the electron transformation occurs at this interface. However, no such phenomenon is found between PCBM and Ca. In addition, the XPS investigations also indicate that electrons transfer from Ca to sulfur in P3HT, causing the increase of energy difference between P3HT and PCBM, and subsequently improving the V_{oc} in solar cell devices.

(1). S. Sista, M.-H. Park, Z. Hong, Y. Wu, J. Hou, W. L. Kwan, G. Li, and Y. Yang, *Adv. Mater.* **2010**, 22, 380-383 .

(2). G. Dennler, M. C. Scharber, and C. J. Brabec, *Adv. Mater.* **2009**, 21, 1323-1338.

(3). G. Xue, B. P. Rand, S. Uchida, and S. R. Forrest, *Adv. Mater. (Weinheim,Ger.)* **2005**, 17, 66-71.

(4). M. O. Reese, M. S. White, G. Rumbles, D. S. Ginley, S. E. Shaheen, *Appl. Phys. Lett.* **2008**, 92, 053307.

(5). F. Bebensee, M. Schmid, H-P. Steinrück, C. T. Campbell, and J. M. Gottfried, *J. Am. Chem. Soc.* **2010**, 132, 12163-12165.

(6). J. Zhu, F. Bebensee, W. Hieringer, W. Zhao, J. H. Baricuatro, J. A. Farmer, Y. Bai, H-P. Steinrück, J. M. Gottfried, and C. T. Campbell, *J. Am. Chem. Soc.* **2009**, 131, 13498-13507.

Hole transport improvement in GaN-based light-emitting diodes by graded-composition multiple quantum barriers

Chao-Hsun Wang*, **Shih-Pang Chang, Pu-Hsi Ku, Chien-Chung Lin, and Hao-Chung Kuo**

Department of Photonics and Institute of Electro-Optical Engineering, National Chiao-Tung University, Hsinchu, Taiwan

Email: josephwang.eo97g@nctu.edu.tw

GaN-based light-emitting diodes (LEDs) grown on c-plane sapphire substrate has recently become a favorable choice for applications in energy saving solid-state lighting[1]. One key feature that still needs to be solved is the so-called "efficiency droop". Despite the various arguments have been proposed and discussed, electron overflow out of the active region, Auger recombination, and insufficient transport of holes have been identified as the most possible reasons for droop[2, 3, 4]. Among these factors, poor transport of holes might be the most important one.

In our former research work, we have demonstrated that leveling the triangular barriers at valence band by using a graded-composition electron blocking layer can effectively enhance the transport of holes across the electron blocking layer[5]. In this paper, we have designed a graded-composition multiple quantum barriers (GQBs) for GaN-based LED to improve the hole transport in active region. The simulation results showed that the triangular barrier of multiple quantum barriers at valance band could be balanced by increasing the band gap of $In_xGa_{1-x}N$ along [0001] direction. As a result, the hole transport in multiple quantum wells was significantly enhanced at either low or high current density, which is beneficial for droop reduction. The GQB LED was realized by MOCVD, and the *I-V* curve showed that GQB LED has lower series resistance than the conventional one and the efficiency droop was reduced from 34% in conventional LED to only 6% in GQB LED, which is in agreement with our simulation results. Beyond these, the efficiency of GQB LED at 20 A/cm^2, was found to be only 70% of that in conventional LED.

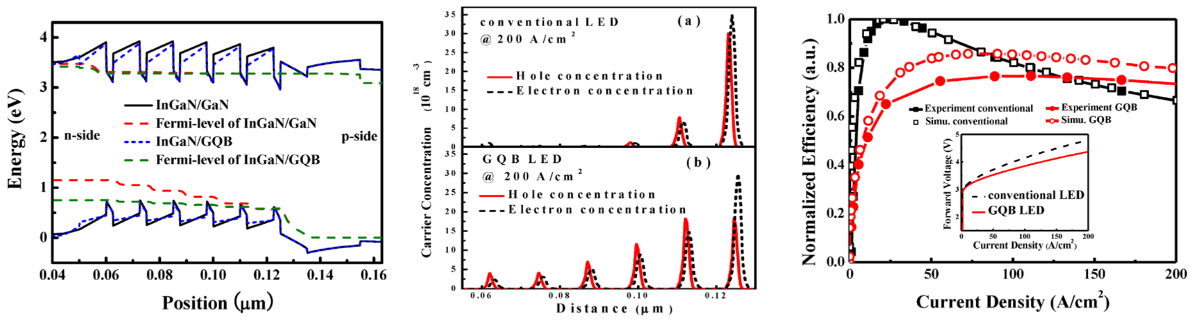

(1). Pimputkar , S.; Speck, J. S.; DenBaars, S. P.; Nakamura, S. *Nat. Photonics* **2009**, *3*, 180-182.

(2). Kim, M. H.; Schubert, M. F.; Dai, Q.; Kim, J. K.; Schubert, E. F.; Piprek, J.; Park, Y. *Appl. Phys. Lett.* **2007**, *91*, 183507.

(3). David, A.; Grundmann, M. J.; Kaeding, J. F.; Gardner, N. F.; Mihopoulos, T. G.; Krames, M. R. *Appl. Phys. Lett.* **2008**, *92*, 053502.

(4) Wang, C. H.; Chen, J. R.; Chiu, C. H.; Kuo, H. C.; Li, Y. L.; Lu, T. C.; Wang, S. C. *IEEE Photon. Technol. Lett.* **2010**, *22*, 236-238.

(5) Wang, C. H.; Ke, C. C.; Lee, C. Y.; Chang, S. P.; Chang, W. T.; Li, J. C.; Li, Z. Y.; Yang, H. C.; Kuo, H. C.; Lu, T. C.; Wang, S. C. *Appl. Phys. Lett.* **2010**, *97*, 261103.

The effect of CdSe/ZnS quantum dots in GaN-based light-emitting diodes

Kuo-Ju Chen[1], **Hsin-Chu Chen**[1], **Min-Hsiung Shih**[1], **Chao-Hsun Wang** [1], **Ming-Yen Kuo**[1], **Chien Chung Lin**[1],**and Hao-Chung Kuo**[1]

[1]*Department of Photonics and Institute of Electro-Optical Engineering, National Chiao-Tung University, Hsinchu, Taiwan*
[2]*Research Center for Applied Sciences, Academia Sinica 128 Academia Rd., Sec. 2 Nankang, Taipei Taiwan*
[3]*Institute of Photonic System, College of Photonics, National Chiao-Tung University, Tainan, Taiwan*
Email: mhshih@gate.sinica.edu.tw

Abstract:
In this work, thermal effect on CdSe/ZnS quantum dots (QDs) for GaN-based light-emitting diodes (LEDs) is investigated through phosphor conversion efficiency and junction temperature of LEDs. For the simulation, the temperature of blue chip and CdSe/ZnS QDs are almost similar due to the thin thickness. Higher junction temperature is observed with more volume of CdSe/ZnS QDs on LEDs.

Results and discussion:

Recently, the development of Light-emitting diodes (LEDs) has been widely studied in view of the practical application in the field of solid-state lighting, while the advantage of LEDs are longer lifetime, higher efficiency, and greater reliability [1-2]. The CdSe/ZnS QDs were spin-coated onto the top surface of blue LEDs. To investigate the thermal effect between LEDs and CdSe/ZnS QDs, we used both continuous-wave (CW) and pulse current sources to verify thermal effect on the PCE of QDs with LEDs. Fig. 1 demonstrates the relative PCE of LEDs with QDs measured by continuous -wave and pulse current source. The pulse width and the duty cycle was set of 1μs and 1% respectively. Assuming both of the LED and CdSe/ZnS QDs generate no heat under pulse operation, the relative PCE exhibited nearly the same value with various operation currents. This phenomenon excludes that the reduction of PCE was partially because the saturation of QDs, but mainly because of the thermal effect.

Moreover, the influence of CdSe/ZnS QDs on LEDs was presented in another way: junction temperature of LEDs with QDs with various volumes of QDs and operation currents are shown in Fig.2. The junction temperature of LEDs increased as the current increased. The reason for the higher junction temperature is attributed to the thermal conduction and non-radiative energy which would reduce the relative PCE. This indicated that the thermal quenching issue would be a great concern for LEDs using QDs as color converting material. In addition, more volume of QDs in LEDs has higher backscattering of light than others. Therefore, it is important to note that temperature would become an essential issue on CdSe/ZnS QDs for light-emitting diodes LEDs. A further study will be done on avoiding the temperature influence CdSe/ZnS QDs.

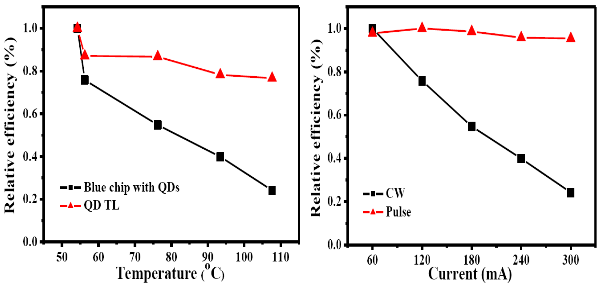

Fig. 1. Relative efficiency of (a) continuous-wave current source and CdSe/ZnS QDs with different temperature (b) continuous-wave current source and pulse source with different current

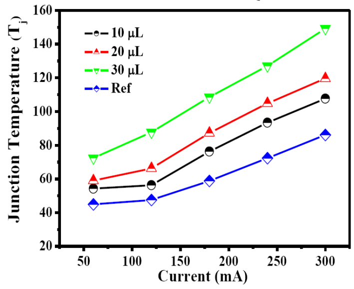

Fig. 2. Junction temperatures of different volume of CdSe/ZnS QDs at the current from 60mA to 300mA

Conclusion:

In this work, this study presents the influence of thermal effect on CdSe/ZnS QDs for light-emitting diodes (LEDs) by PCE and junction temperature. The result support that CdSe/ZnS QDs are easily influenced under thermal atmosphere. Higher junction temperature is attributed to the thermal conduction and nonradiative energy between the CdSe/ZnS QDs and blue chip. Therefore, it is important to note that temperature would become an essential issue on CdSe/ZnS QDs for light-emitting diodes LEDs. A further study will be done on avoiding the temperature influence CdSe/ZnS QDs.

Reference:

(1). T. Nishida, T. Ban, and N. Kobayashi, *Appl. Phys. Lett.* **2003**, 82, 3817-3819.
(2). E. F. Schubert, J. K. Kim, *Science* **2005**, 308, 1274-1278.

Highly Efficient CdS-Quantum-Dot-Sensitized Solar Cell for c-Si with Nanopillar Array

Hsin-Chu Chen[1], **Chien-Chung Lin**[2], **Hao-Chung Kuo**[1], **and Peichen Yu**[1]

[1]*Department of Photonics and Institute of Electro-Optical Engineering, National Chiao-Tung University, Hsinchu, Taiwan*

[2]*Institute of Photonic System, College of Photonics, National Chiao-Tung University, Tainan, Taiwan*

Email: chienchunglin@faculty. nctu.edu.tw

Abstract:

The enhanced efficiency of the crystalline silicon (c-Si) with nanopillar arrays (NPAs) solar cell by quantum dots (QDs) was demonstrated. The device with CdS quantum dots shows the higher power conversion efficiency about 33%.

Result and discussion:

In this experiment, we use colloidal lithography and dry etched methods to fabricate c-Si NPAs solar cell [1]. Then, a colloidal CdS QDs was spun on the surface of c-Si NPAs solar cell. For comparison, the one without the CdS QDs was also fabricated simultaneously as the reference. In the Fig. 1 (a) show the SEM image of c-Si NPAs that the periodicity is accurately transferred onto the Si substrate after RIE and the height of NPAs is about 550 nm. The TEM image taken near the edge of metal contact and the thickness of the CdS layer is ~6 nm, as shown in Fig. 2 (b). The Energy Dispersive Spectrometer (EDS) pattern of CdS QDs is also shown in (inserts of under corner) the image. Therefore, we can more confirm the elements of Cd and S to exist on the cell. Fig. 2(a) shows the measurement of total reflectance spectra by an integrating sphere at the normal incidence of light. The c-Si NPAs with CdS QDs exhibited superior antireflective properties for the c-Si solar cell absorption range, especially reduced reflectance in the range of wavelength from 450 nm to 1100 nm, compared with the without CdS QDs. Fig. 2(b) shows the photovoltaic I–V characteristics of the c-Si NPAs solar cell with and without CdS QDs. It is noticeable that power conversion efficiency can be improved effectively by surface spin-cast of CdS QDs. The main mechanism of enhancement includes photon down-conversion, antireflection, and current conductivity. As a result, the overall power conversion efficiency is improved by 33%, compared with the c-Si NPAs solar cell without CdS QDs. In EQE measurement, the spread of CdS QDs helped the electrical conduction and thus improve the overall fill factor, as shown in Fig. 3. This part can make up for about 90% of the enhancement in efficiency. Another part of 10% is from down-conversion of the quantum dots in the short-wavelength excitation and the anti-reflection in the longer wavelength range. Although it only takes 10% of the enhancement, the potential of using quantum dot as a down-conversion layer in solar cell should not be ignored.

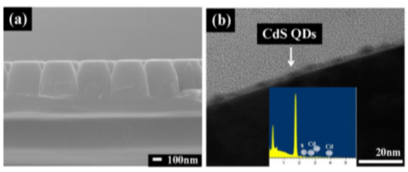

Fig.1. (a) The SEM image of the c-Si nanopillar arrays. (b) The TEM image after the integration CdS QDs layers, the size of CdS QDs layers is about 6 nm and EDS (insets of under corner).

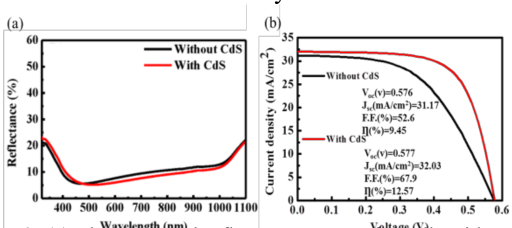

Fig. 2. (a) The measured reflectance spectra for cells with c-Si nanopillar arrays (NPA) with and without CdS QDs. (b) Photovoltaic I–V characteristics of the c-Si NPAs solar cell with and without CdS QDs.

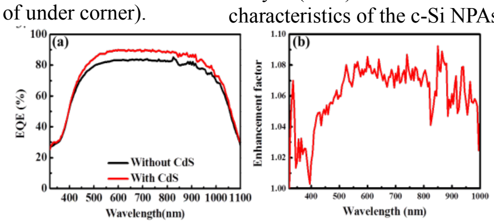

Fig. 3. (a) Measurement of EQE of the fabricated c-Si NPAs solar cell with and without CdS QDs. (b) Peak (at ~335 nm wavelengths) of short-wavelength enhancement of in EQE indicates photon down-conversion.

Conclusion:

In summary, the enhanced efficiency of the c-Si solar cell with NPAs via CdS QDs is demonstrated. It is noticeable that power conversion efficiency can be enhanced effectively by surface spin-cast of CdS QDs. The main mechanism of enhancement includes photon down-conversion, antireflection, and current conductivity. Finally, we believe that the CdS QDs layer is suitable for Si-based solar cells, and other related applications in the future.

Reference:

(1). M. A. Tsai, P. C. Tseng, H. C. Chen, and H. C. Kuo, *Opt. Express*. **2011**, 19, A28-A34.

LED Low and High Order Mode Light Extraction Using Composite Nanohole and Surface Photonic Crystals

<u>Yu-Feng Yin,</u> Szu-Chieh Wang, Yun-Wei Cheng and JianJang Huang

Graduate Institute of Photonics and Optoelectronics, National Taiwan University, No. 1, Roosevelt Road, Taipei, 10617 Taiwan

Email: jjhuang@cc.ee.ntu.edu.tw

LEDs are usually featured with weakly coupling between the laterally propagating light and the surface nanostructure. In this paper we employ Photonic Crystal (PhC) structure on the mesa surface and nanohole reflectors at the periphery of the mesa on GaN-based LEDs. It is found that this novel structure is provided with higher light extraction efficiency than the structure with only surface PhCs by the enhancement of low-order mode from the laterally propagating light. Accordingly, the diffraction between in-plane light and the nanoholes reflectors is much stronger than that with only surface PhCs, thus suggests high diffraction efficiency from nanohole reflectors.

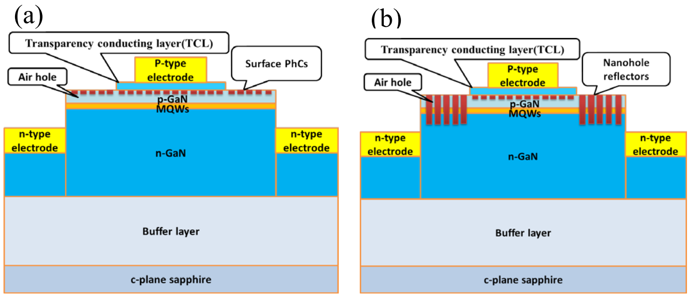

Fig. 1 The device profile of (a) Surface PhCs LED etched by 70nm (SLED) (b) Surface PhCs etched by 70nm and nanohole reflectors LED etched by 400nm (SHLED)

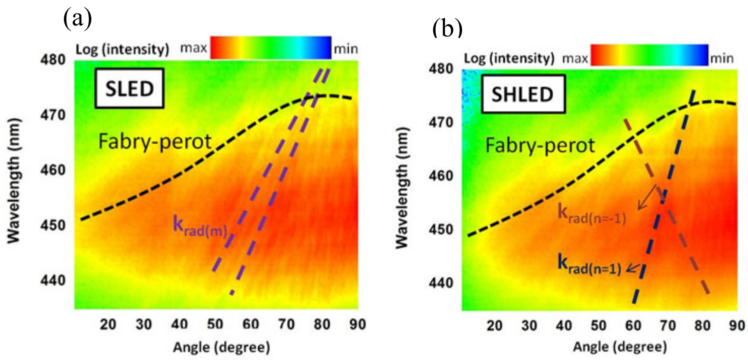

Fig. 2 (a) angular spectrum of SLED (b) angular spectrum of SHLED

(1). Y. W. Cheng, K. M. Pan, L. Y. Chen, M. Y. Ke, C. P. Chen, C. Y. Chen, C. C. Yang, and J. J. Huang, IEEE Electron Device Lett, vol. 30, No. 1060, 2009.

(2). Y. W. Cheng, S. C. Wang, Y. F. Yin, L. Y. Su, and JianJang Huang, Optics Letters, Vol. 36. Issue 9, pp. 1611-1613, 2011.

ZnO nanorod arrays as antireflection layers for III-V solar cells

Li-Ko Yeh*, Kun-Yu Lai, Guan-Jhong Lin, and Jr-Hau He

Institute of Photonics and Optoelectronics and Department of Electrical Engineering National Taiwan University Taipei, Taiwan

Email: jhhe@cc.ee.ntu.edu.tw

Syringelike ZnO NRAs synthesized by the hydrothermal method are demonstrated as an effective antireflection coating for GaAs solar cells. Taking advantage of the syringelike ZnO NRAs with favorable tip geometry, the abrupt interface between air and GaAs can be replaced with the engineered antireflection layers containing a smooth refractive-index transition, significantly suppressing the surface reflection on the device over a wide range of wavelengths, further confirming that the improved flatness f the refractive index profile near the air–nanostructure interface is the key to excellent antireflection performance. Under AM 1.5G illumination, the energy conversion efficiency of the device is significantly enhanced by up to 32%.

.

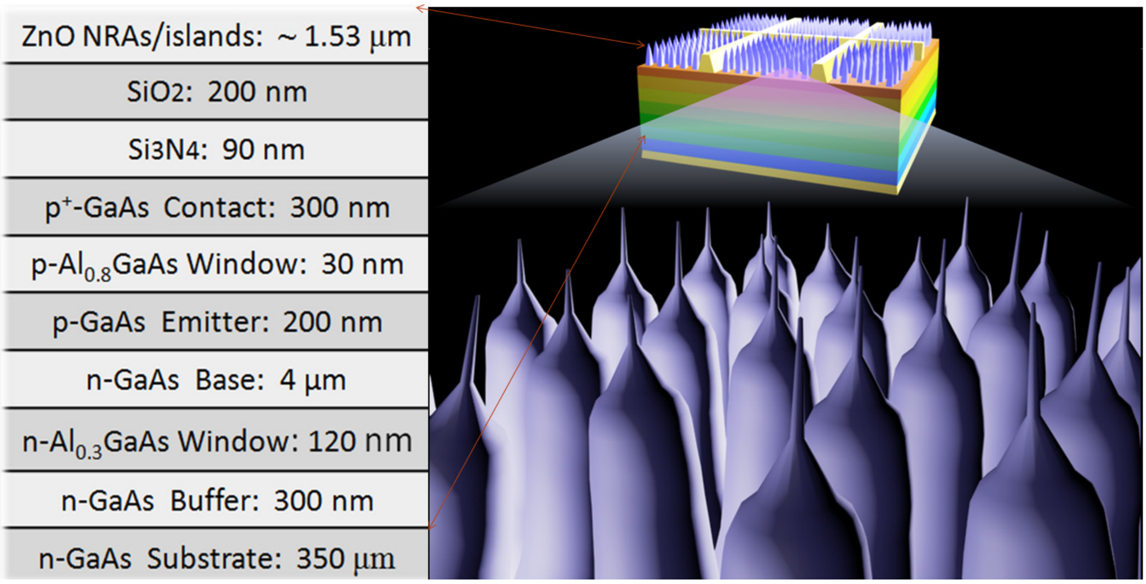

Fig. 1 . Layer structure of the single-junction GaAs solar cell.

Investigations of GaN-Based Photonic Crystal Surface Emitting Lasers with Localized Defects

Tzeng-Tsong Wu, Peng-Hsiang Weng, Yen-Ju Hou, Tien-Chang Lu*, Hao-Chung Kuo and Shing-Chung Wang

Department of Photonics and Institute of Electro-Optical Engineering, National Chiao Tung University, Hsinchu 300 Taiwan, R.O.C.
** E-mail address: timtclu@mail.nctu.edu.tw*

Abstract: The GaN-based Photonic crystal surface emitting lasers (PCSELs) with different central defects were fabricated and investigated. The characteristics for PCSELs with different central defects were calculated and matched well with experimental results.

Photonic crystal (PC) surface emitting laser (PCSEL) utilizing a 2D distributed feedback (DFB) mechanism has been widely researched because of their superior advantages such as high power emission, single mode operation and coherence oscillation over a large area[1]. By selecting the lattice and radius of PCs, it would satisfy the specific Bragg condition at the band edges and produce the surface emitting condition. Up to now, many groups have been demonstrated PCSELs with emission wavelengths from UV to IR bands[2, 3]. In this report, the GaN-based PCSELs with different central defects have been fabricated and measured to comprehend the effect of central defects on lasing characteristics of PCSELs. By tuning the central defect sizes, the Γ band edge mode could be disturbed. Different threshold energy density and lasing wavelength for different central defects were obtained by micro-PL system.

The GaN-based PCSEL was consisted of a 25-pair AlN/GaN DBR and a 560 nm-thick n-GaN layer, 10 pairs of InGaN/GaN multiple quantum wells (MQWs), a 24 nm-thick AlGaN electron blocking layer, and a 175 nm-thick p-GaN layer. Then we fabricated photonic crystal patterns on the as-grown structure to form the PCSELs. Figure 1(a) and (b) show the schematic diagram of our GaN-based PCSEL and the SEM images including H0, H3, H4 and H5, respectively. The number after H means short of the PC shell number.

The pumping energy density versus output intensity curves of PCSELs with different defect cavities of H0, H3, H4 and H5 are pumped by the 355 nm pulse Nd:YVO_4 laser and shown as Fig. 2(a). The threshold energy densities are measured to be 3.23, 3.3, 3.44 and 3.51 mJ/cm^2 for H0, H3, H4 and H5 defect structures, respectively. Fig. 2(b) shows the lasing wavelengths of H0, H3, H4 and H5 defect cavity. The lasing wavelengths are observed at 400, 398, 392 and 390 nm for H0, H3, H4 and H5 defect cavities. It indicate that the PCSELs with a larger defect size exhibits higher threshold power density and the lasing wavelength would blue shift when the defect size becomes larger.

In summary, we have fabricated and investigated the GaN-based PCSELs with different central defects. The threshold energy density shows a rising tendency from 3.23 to 3.51 mJ/cm^2 as the central defect size increases. In addition, the lasing wavelength of each defect cavity shows a blue shift from 400 nm to 390 nm due to the guided mode shifting in PCSELs with different central defects. The experimental results show that the PCSEL with a larger defect size would have a higher threshold, which could be due to the less distributed feedback provided by the less photonic crystal lattice. These observations can provide a better understanding of the band-edge photonic crystal lasers with central defects.

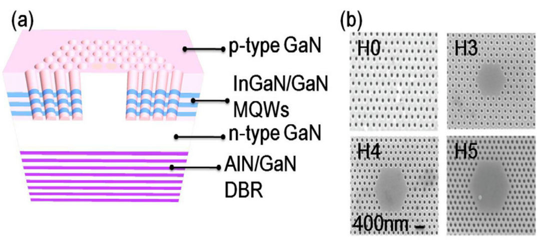

Fig. 1 (a) The overall device structure of GaN-based PCSELs. (b) The plan-view SEM images of no-defect (H0), H3, H4 and H5 central defect structures of GaN-based PCSELs.

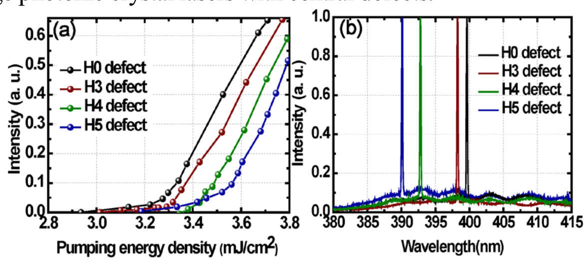

Fig. 2 (a) Measured output intensity versus input excitation energy density from the GaN-based PCSELs for H0, H3, H4 and H5 defect cavities (b) Lasing spectrum of different central defect structures including H0, H3, H4 and H5.

(1) M. Meier, A. Mekis, A. Dodabalapur, A. Timko, R. E. Slusher, J. D. Joannopoulos, and O. Nalamasu, Appl. Phys. Lett., **1999**, 74, 7-9.
(2) H. Matsubara, S Yoshimoto, H. Saito, Y. Jianglin, Y. Tanaka and S. Noda, Science., **2008**, 445-447.
(3) T. C. Lu, S. W. Chen, L. F. Lin, T. T. Kao, C. C. Kao, P. Yu, H. C. Kuo, S. C. Wang and S. H. Fan, Appl. Phys. Lett., **2008**, 92, 011129.

Optical Properties of InGaN Multiple Quantum Wells Grown on GaN Nanopyramid Arrays

Tzeng-Tsong Wu[1], **Ya-Yu Yang**[2], **Chiao-Yun Chang**[1], **Tien-Chang Lu**[1], **Wei-Chih Lai**[2], **Hao-Chung Kuo**[1] **and Shing-Chung Wang**[1]

[1] *Department of Photonic & Institute of Electro-Optical Engineering, National Chiao Tung University, Taiwan*
[2] *Department of Photonic, National Cheng Kung University, Taiwan*
** E-mail address: timtclu@mail.nctu.edu.tw*

Abstract: InGaN/GaN multiple quantum wells on GaN nanopyramid arrays have been fabricated and investigated. The optical characteristics of InGaN/GaN nanopyramid arrays have been investigated by photoluminescence and cathodeluminescence.

III-nitride materials have been drew much attentions and widely researched since it has great potential for many applications such as light-emitting diodes (LEDs) and laser diodes (LDs) [1, 2]. This can be expected grown on the non-polar and semipolar GaN facets are the solution to avoid the QCSE, increase the internal quantum efficiency and wavelength stability[3]. In this report, we have deposited the InGaN/GaN multiple quantum wells (MQWs) on the GaN nanopyramid arrays by selected area growth (SAG) of the GaN nanopyramid arrays and investigated their optical properties such as power dependent photoluminescence (PL) and cathodoluminescence (CL).

Fig. 1(a) shows the spectra of InGaN/GaN MQWs on the GaN nanopyramid arrays which were observed by power dependent micro-PL system. When the excitation power was increased from 0.02mW to 20mW, all of the PL peaks showed the invariant tendency during this range, as shown in Fig. 1(b). It indicates that the InGaN/GaN MQWs grown on the GaN nanopyramid arrays suffer very low internal piezoelectric field and could decrease the QCSE. The power index α is fitted to be around 1 of our sample which indicates that the radiative recombination dominate the optical transition[4].

Fig. 2 shows the CL spectrum, SEM image and CL spectrally resolved mappings of InGaN/GaN nanopyramid arrays, the broad emission can be observed from the InGaN/GaN nanopyramid arrays. On the other hand, the spectrally resolved mappings reveal that the different emission wavelength is in different location of nanopyramid. This could be attributed to indium diffusion on the facets of nanopyramid during quantum well growth.

In conclusion, we have fabricated and investigated the semi-polar InGaN/GaN MQWs grown on the GaN nanopyramid arrays by nanosphere lithography. This method provides the low cost technique for fabrication of the semi-polar GaN-based LEDs.

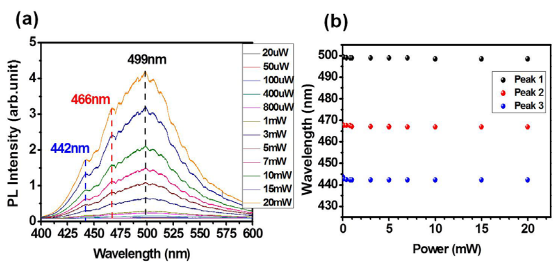

Fig. 1(a) Power dependent micro-PL spectra (b) The peak shift of with respect to the power of InGaN/GaN MQWs grown on GaN nanopyramid arrays.

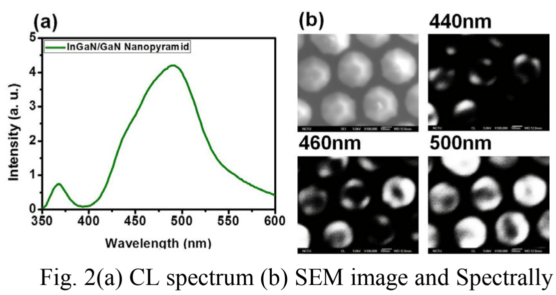

Fig. 2(a) CL spectrum (b) SEM image and Spectrally resolved CL mapping of InGaN/GaN MQWs grown on GaN nanopyramid arrays.

(1) S. Nakamura, M. Senoh, N. lwasa, T. Yamada, T. Matsushita, H. Kiyoku, Y. Sugimoto, T. Kozaki, H. Umemoto, M. Sano, K. Chocho, Jpn. J. Appl. Phys. **1997**, 36, pp. L1586,.
(2) S. Keller, R. Vetury, G. Parish, S.P. DenBaars, U.K. Mishra, Appl. Phys. Lett. **2001**, 78, pp. 3088.
(3) T. Takeuhi, H. Amano, I. Akasaki, Jpn. J. Appl. Phys. **2000**, 39, pp. 413,.
(4) C.H. Chiu, S.Y. Kuo, M.H. Lo, C.C. Ke, T.C. Wang, Y.T. Lee,1, H.C. Kuo, T.C. Lu, S.C. Wang, J. Appl. Phys. **2009**, 105, pp. 063105,.

Effect of Defects and Strains on the Internal Quantum Efficiency of GaN Nanorod Light Emitting Arrays

Li-Chuan Huang[1,3], Chun-Hsiang Chang[1], Liang-Yi Chen[1], and JianJang Huang[1,2,4]

1: Graduate Institute of Photonics and Optoelectronics, National Taiwan University, Taipei, Taiwan
2: Department of Electrical Engineering, National Taiwan University, Taipei, Taiwan
3: r99941011@ntu.edu.tw 4: jjhuang@cc.ee.ntu.edu.tw

In recent years, GaN based nano-structured light emitting diodes (LEDs) have attracted considerable attentions as they may have the potential of strain relaxation due to the vacant spaces among the rod arrays and better light extraction due to the increased sidewall areas that directly affect the light output power[1,2]. The total light output efficiency has also been a very popular topic for GaN based light emitting diodes, in which the effect of efficiency droop is known to be a severe issue. In our previous work, GaN based nanorod LED arrays with low reverse bias leakage was fabricated using the chemical mechanical polishing (CMP) process and characterized at room temperature[3,4]. The schematic diagram of the nanorod LED array was illustrated in Fig.1.

For InGaN/GaN based nanorod devices, the optical output power is affected by non-radiative recombination due to sidewall defects and mitigated quantum confined Stark effect (QCSE) due to strain relaxation. In this work, we explore the correlation between these effects by two samples with different length of nanorod LEDs. Longer nanorod may cause a stronger strain relaxation but more defect state distribution, resulting in a mildly increasing EQE with less droop.

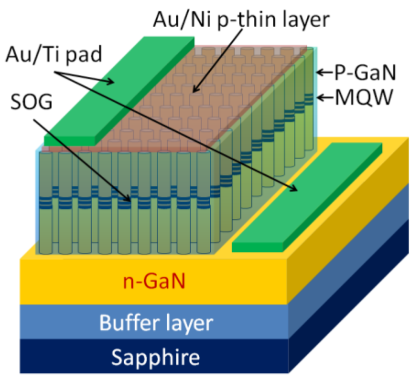

Fig. 1

(1). C. H. Chiu; T. C. Lu; H. W. Huang; C. F. Lai; C. C. Kao; J. T. Chu; C. C. Yu; H. C. Kuo; S. C. Wang; C. F. Lin; T. H. Hsueh *Nanotechnology, vol. 18,* p. 445201, **2007**.

(2). M. Y. Ke; C. Y. Wang; L. Y. Chen; H. H. Chen; H. L. Chiang; Y. W. Cheng; M. Y. Hsieh; C. P. Chen; J. J. Huang *IEEE Journal of Selected Topics in Quantum Electronics, vol. 15,* pp. 1242-1249, **2009**.

(3). Y. H. Sun; Y. W. Cheng; S. C. Wang; Y. Y. Huang; C. H. Chang; S. C. Yang; L. Y. Chen; M. Y. Ke; C. K. Li; Y. R. Wu; J. J. Huang *Electron Device Letters, IEEE, vol. 32,* pp. 182-184, **2011**.

(4). L. Y. Chen; Y. Y. Huang; C. H. Chang; Y. H. Sun; Y. W. Cheng; M. Y. Ke; C. P. Chen; J. J. Huang *Optics Express, vol. 18,* pp. 7664-7669, **2010**.

Nano-crystalline Silicon based Bottom Gate Thin Film Transistor Grown by LTPECVD with Ar diluted SiH_4

Chih-Hsien Cheng and **Gong-Ru Lin***

Graduate Institute of Photonics and Optoelectronics, and Department of Electrical Engineering, National Taiwan University, No. 1 Roosevelt Road Sec. 4, Taipei 106, Taiwan R.O.C.
Email: grlin@ntu.edu.tw

Hydrogenated amorphous silicon (a-Si:H) is a promising material usually applied to thin-film solar cells and thin-film MOS transistors, which are also an alternative to the poly-Si film grown at 550-650^{o}C with limited application in flexible optoelectronics. To prevent the exploitation of pure SiH_4 with dangerous hydrogen carrier as the fabricating gas for a-Si:H, we demonstrate the deposition of nano-crystalline silicon (nc-Si:H) within the a-Si:H film grown by using Ar diluted SiH_4 under extremely low RF plasma power in a low-temperature plasma enhance chemical-vapor deposition (LT-PECVD) system. The nc-Si based thin film transistor (TFT) on glass substrate grown with Ar diluted SiH_4 is characterized.

The nc-Si based TFT on glass is a bottom-gate inverted staggered structure with the channel length and width of 180 μm and 10 μm, respectively. First, the evaporated Cr gate electrode of 200 nm was coated on glass substrate. The 250-nm thick Si_3N_4 based gate layer was deposited by PECVD. Following the deposition of gate layer, the nc-Si:H channel layer of 200 nm grown by Ar diluted SiH_4 of 100 sccm was deposited at substrate temperature of 250^{o}C with the chamber pressure of 0.17 torr and the RF plasma power changing from 20 to 100 W at 20 W increment. Then, a phosphorus-doped n^+-Si film of 50 nm thickness was deposited. Finally, a 200-nm thick Cr drain and source electrodes were evaporated upon the n^+-Si layer.

The effective capacitance of nc-Si:H TFT devices on glass enhances from 14.9 to 17.8 nF/cm^2 with increasing RF plasma power as the faster deposition of nc-Si:H layer restricts the oxygen incorporation during the nano-crystalline Si systhesis and thus prevents the foramtion of SiO_2 in the nc-Si:H layer under the lower RF plasma power. The oxygen content of nc-Si:H films decreases from 6.7% to 3.9% when increasing the RF plasma power from 20 W to 100 W. The effective oxide trapped charge density is reducing from 3.7×10^{10} to 6.7×10^9 cm^{-2} by enlarging the RF plasma power. The decrement of effective oxide trapped charge density results in the reduction of threshold voltage and channel charge density. With enlarging RF plasma power, the nc-Si:H TFT on glass enhances its field mobility from 0.57 to 1.31 cm^2/V·s and decreases its threshold voltage from 4 to 2.7 V owing to the higer mobility of nc-Si:H film in contrast to that of a traditional a-Si:H TFT. Similarly, the ON/OFF ratio of nc-Si:H based TFT increases from 1.0×10^4 to 1.5×10^5 by growing at enhanced RF plasma environment. Nevertheless, the threshold voltage and the ON/OFF ratio of nc-Si:H based TFT grown at RF plasma power of 100 W decrease by 20% and 50% when increasing the operation temperature from 20^{o}C to 70^{o}C because of the increment of leakage current at the higher temperature. We successfully take the imcomplete decomposition of Ar duilted SiH_4 by dutuning RF plasma power to generate the nc-Si based TFT and to avoid using the hydrogen duilted SiH_4.

Ultrahigh Responsivity Broadband Detection of Si Metal-Semiconductor-Metal Schottky Photodetectors Improved by ZnO Nanorod Arrays

Dung-Sheng Tsai,[†‡] Chin-An Lin,[†] Wei-Cheng Lien,[†§] Hung-Chih Chang,[†]
Yuh-Lin Wang,[‡] Jr-Hau He[†*]

[†] *Institute of Photonics and Optoelectronics, and Department of Electrical Engineering, National Taiwan University, Taipei (Taiwan)*
[‡] *Institute of Atomic and Molecular Sciences, Academia Sinica, Taipei (Taiwan)*
[§] *Berkeley Sensor and Actuator Center, University of California, Berkeley, California (USA)*
**Email: jhhe@cc.ee.ntu.edu.tw*

This study describes a strategy for developing ultrahigh responsivity broadband Si-based photodetectors (PDs) using ZnO nanorod arrays (NRAs). The ZnO NRAs grown by a low-temperature hydrothermal method with large growth area and high growth rate absorb the photons effectively in the UV region and provide refractive index matching between Si and air for the long-wavelength region, leading to 3 and 2 orders of magnitude increase in the responsivity of Si metal-semiconductor-metal PDs in the UV and visible/NIR regions, respectively. Significantly enhanced performances agree with the theoretical analysis based on finite-difference time-domain method. These results clearly demonstrate that Si PDs combining with ZnO NRAs hold high potential in the next-generation broadband PDs.

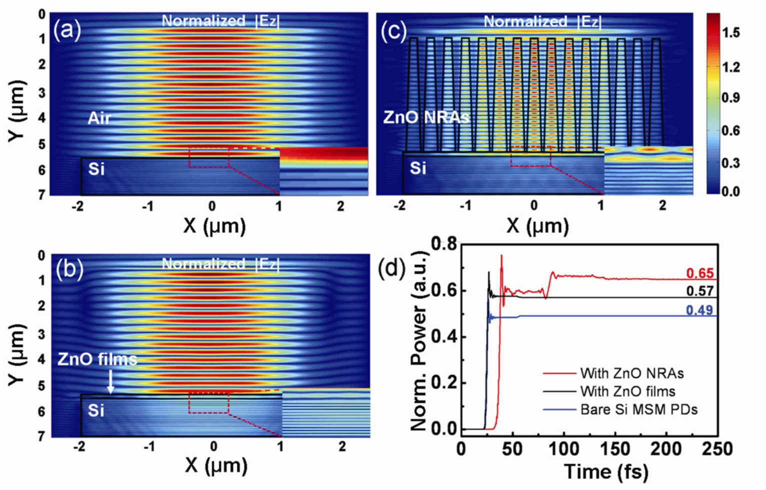

Fig. 1 Time-averaged and normalized TE electric field, |Ez|, distribution at 543 nm simulated by FDTD analysis within (a) the bare Si MSM PDs, (b) with ZnO films and.(c) with ZnO NRAs. (d) Normalized optical power, detected at 0.6 μm below the surface of Si, as a function of time. The insets in (a)-(c) are the enlarged images at the top Si surface.[1]

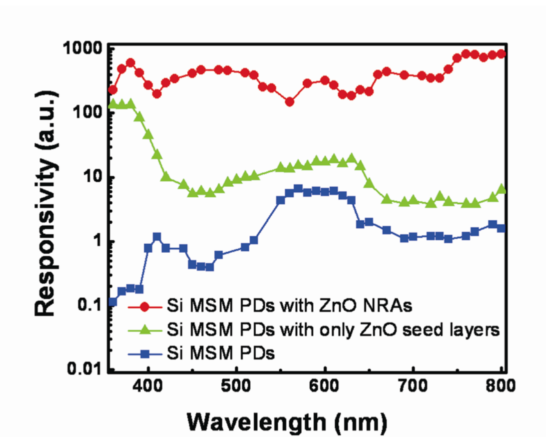

Fig. 2 A comparison of the spectral responsivity under 15 V bias.[1]

(1). Tsai, D.S.; Lin, C.A.; Lien, W.C.; Chang, H.C.; Wang, Y.L.; He, J.H. *ACS Nano* **2011**, 5, 7748-7753.

Fabrication of three dimensional split ring resonators by stress-driven assembly method

Chih Ting Hsiao[1, *], Che Chin Chen[2], Shulin Sun[1,3], Kuang-Yu Yang[4], Pin Chieh Wu[1], Wei Ting Chen[4], Lei Zhou[5], Guang-Yu Guo[1,6], and Din Ping Tsai[1,2,4,7]

[1]*Department of Physics, National Taiwan University, Taipei 10617, Taiwan*
[2]*Instrument Technology Research Center, National Applied Research Laboratory, Hsinchu 30076, Taiwan*
[3]*National Center of Theoretical Sciences at Taipei, Physics Division, National Taiwan University, Taipei 10617, Taiwan*
[4]*Graduate Institute of Applied Physics, National Taiwan University, Taipei 10617, Taiwan*
[5]*State Key Laboratory of Surface Physics and Key Laboratory of Micro and Nano Photonic Structures (Ministry of Education), Fudan University, Shanghai 200433, China*
[6]*Graduate Institute of Applied Physics, National Chengchi University, Taipei 11605, Taiwan*
[7]*Research Center for Applied Sciences, Academia Sinica, Taipei 11529, Taiwan*
[*]*Email: r99222063@ntu.edu.tw*

The split ring resonators (SRRs) are the most common meta-molecule adopted in constructing the sub-wavelength structures. In particular, the behavior of a single SRR can be approximately considered as a LC circuit, in which the capacitor is contributed by the charges accumulating near the gap and the inductor is contributed by the surface current flowing inside the split ring[1]. In previous works, most of the SRR structures were focused on the planar types, i.e. the SRRs plane is lay on the substrate, due to the limited fabrication methods and the LC resonance mainly obtained through capacitance response. The induction response in planar SRRs can be performed only with the applied external light having an off-normal direction with respect to the SRRs plane, which thus lowers the coupling efficiency. In this paper, we demonstrate a relative simple method by adopting metal stress driven assembly strategy to fabricate the 3D SRRs. This strategy is simply combined with electron beam lithography (EBL) and reactive ion etching (RIE) processes, providing a promising way for the applications of 3D SRRs.

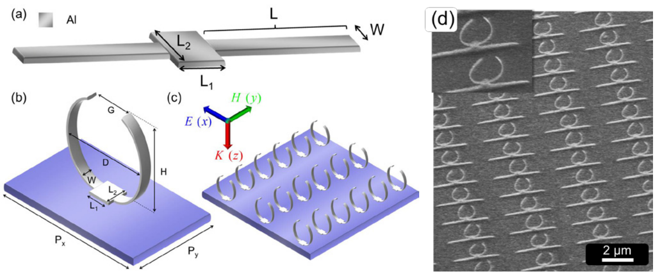

Fig. 1 The schematic diagram with the feature sizes of 3D SRRs before (a) and after (b) released from the substrate by dry etching method. The parameters of our designed SRRs are L_1 = 250 nm, L_2 = 300 nm, W = 125 nm, H = 2 μm, D = 1.8 μm, G = 600 nm, P_x = 8 μm and P_y = 3 μm respectively. (c) The fabricated sample is illuminated by an x-polarized light at normal incidence. (d) The oblique view of SEM micrographs with tilting angle of 40 degree for the 3D SRRs.

(1). Chen, W. T.; Chen, J. C.; Wu, P. C.; Sun, S.; Zhou, L.; Guo, G. Y.; Hsiao, C. T.; Yang, K. Y.; Zheludev, N. I.; Tsai, D. P. *Opt. Express* **2011** 19, 12837–12842.

Optical magnetic response in three-dimensional metamaterial of upright plasmonic meta-molecules

Pin Chieh Wu[1,*], Wei Ting Chen[2], Chen Jung Chen[1], Shulin Sun[1,3], Lei Zhou[4], Guang-Yu Guo[1,5], Chih Ting Hsiao[1], Kuang-Yu Yang[1], and Din Ping Tsai[1,2,6,7]

[1]*Department of Physics, National Taiwan University, Taipei 10617, Taiwan*
[2]*Graduate Institute of Applied Physics, National Taiwan University, Taipei 10617, Taiwan*
[3]*National Center of Theoretical Sciences at Taipei, Physics Division, National Taiwan University,Taipei 10617, Taiwan*
[4]*State Key Laboratory of Surface Physics and Key Laboratory of Micro and Nano Photonic Structures (Ministry of Education), Fudan University, Shanghai 200433, China*
[5]*Graduate Institute of Applied Physics, National Chengchi University, Taipei 11605, Taiwan*
[6]*Instrument Technology Research Center, National Applied Research Laboratory, Hsinchu, 300, Taiwan*
[7]*Research Center for Applied Sciences, Academia Sinica, Taipei 11529, Taiwan*
[*]*Email: r98222071@ntu.edu.tw*

Metamaterials are created as an array of artificial sub-wavelength structures, often exhibit unique optical properties which are not found in nature. Metamaterials composited with sub-wavelength split ring resonators (SRRs) have attracted a wide attention because of a number of extraordinary properties, optical chirality, negative refraction index and optical spectrum manipulation. The electromagnetic (EM) characteristics of SRRs such as negative index of refraction were first studied in microwave region in 2000. Since 2004, interest in them has extended to the optical frequency region in order to gain the boarder applications.

We used bouble electron beam lithagrophy to fabricate a photonic metamaterial—an array of erected (off-plane) gold SRRs on the nanometer scale—and studied their optical properties by both experiments and numerical simulations[1]. A special feature of our structure is that its magnetic resonance can be excited by electric field and magnetic field of normally incident light simultaneously. This optical response of off-plane SRR structure will open a way toward the research of molecule sensing, plasmonic hybridization, artificial magnetism and toroidal metamaterials[2].

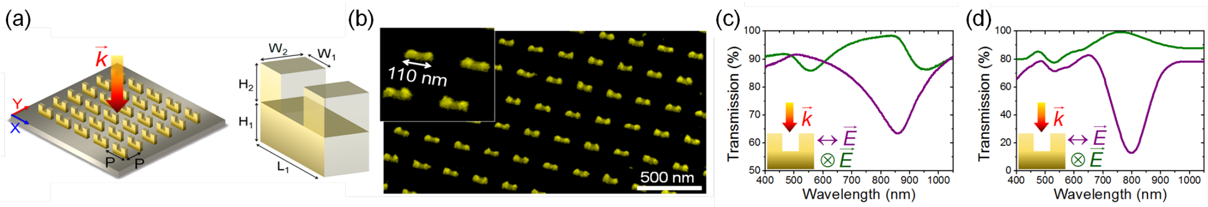

Fig. 1 (a) Schematic diagram showing the feature size of erected SRR structure, $L_1 = 110$ nm, $H_1 = 30$ nm, $H_2 = 30$ nm, $W_2 = 40$ nm, $W_1 = 40$ nm, respectively. The period P is 200 nm both in x and y direction. (b) SEM image of a small region from the fabricated sample. (c) Experimental and (d) simulation transmission spectra for x-polarized illumination (the purple curve) and y-polarized illumination (the green curve).

(1). Chen, W. T.; Chen, J. C.; Wu, P. C.; Sun, S.; Zhou, L.; Guo, G. Y.; Hsiao, C. T.; Yang, K. Y.; Zheludev, N. I.; Tsai, D. P. *Opt. Express* **2011** 19, 12837–12842.
(2). Kaelberer, T.; Fedotov, V. A.; Papasimakis, N.; Tsai, D. P.; Zheludev, N. I.; *Science* **2010** 330, 1510–1512.

High-sensitivity in vivo THz mammography of early human breast cancer in a mouse model

Tzu-Fang Tseng, Hua Chen, Te-Hsuen Chen, Jen-Tang Lu, Chung-Chiu Kuo, Shih-Chen Fu, Wen-Jeng Lee, Yuan-Fu Tsai, Yi-You Huang, Eric Y. Chuang, Yuh-Jing Hwang, and Chi-Kuang Sun

Institute of Photonics and Optoelectronics & Department of Electrical Engineering, National Taiwan University, Taipei 106, Taiwan
Email: f98941037@ntu.edu.tw

We performed *in vivo* THz transmission imaging study on a subcutaneous xenograft mouse model for early human breast cancer detection. With a THz-fiber-scanning transmission imaging system, we continuously monitored the growth of human breast cancer in mice. Our *in vivo* study not only indicates that THz transmission imaging can distinguish cancer from the surrounding fatty tissue, but also with a high sensitivity. Our *in vivo* study on the subcutaneous xenograft mouse model will encourage broad and further investigations for future early cancer screening by using THz imaging system[1].

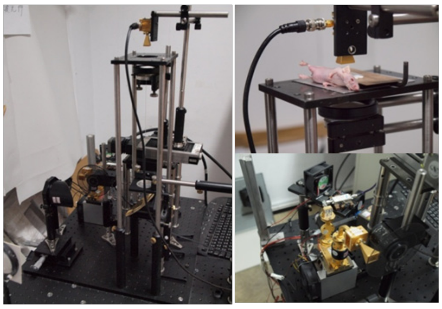

Fig. 1 Photograph of the fiber scanning system

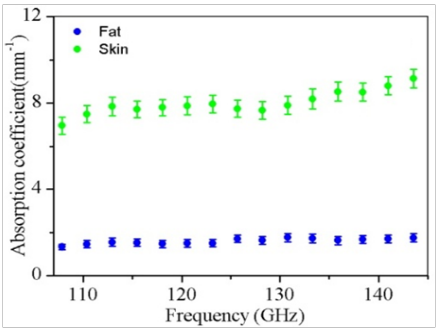

Fig. 2 The absorption coefficient of fat and skin

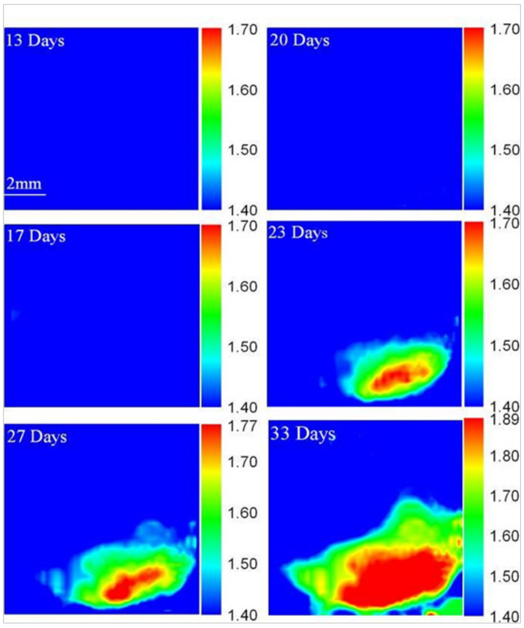

Fig. 3 The images of the early detection of breast tumor

(1). H. Chen, T. Chen, T. Tseng, J. Lu, C. Kuo, S. Fu, W. Lee, Y. Tsai, Y. Huang, E. Chuang, Y. Hwang, and C. Sun, Opt. Express **2011**,*19*, 21552-21562.

Histopathological diagnosis of oral cancer based on higher-harmonic generation microscopy

Ming-Rung Tsai,[1] **Da-Bin Shieh**,[2] **Pei-Jen Lou**,[3] **and Chi-Kuang Sun***[1,4,5]

[1] *Department of Electrical Engineering & Graduate Institute of Photonics and Optoelectronics, National Taiwan University, Taipei 10617, Taiwan*
[2] *Institute of Oral Medical & Institute of Basic Medical Sciences & Center for Micro/Nano Sciences and Technology, National Cheng-Kung University, Tainan 70101, Taiwan*
[3] *Department of Otolaryngology, National Taiwan University Hospital and National Taiwan University College of Medicine, Taipei 10051, Taiwan*
[4] *Molecular Imaging Center & Graduate Institute of Biomedical Electronic and Bioinformatics, National Taiwan University, Taipei 10617, Taiwan*
[5] *Institute of Physics & Research Center for Applied Sciences, Academia Sinica, Taipei 11529, Taiwan*
Email: d96941005@ntu.edu.tw

In vivo higher-harmonic generation microscopy (HGM) performed on healthy human oral mucosa has been reported to not only provide images with a <500nm lateral resolution at a 280 μm penetration depth, but also leave no energy or photodamages in the interacted tissues. These advantages suggest that HGM could serve as an ideal virtual biopsy tool for *in vivo*, *in situ*, and immediate histopathological diagnosis of oral cancer. It is thus critical to investigate if the endogenous contrast provided by the HGM enough to diagnose the differences between cancerous and normal tissues in human oral mucosa. In this paper, *ex vivo* HGM study was performed on the cancerous mucosa from 10 patients with oral squamous cell carcinoma (OSCC). We found that third harmonic generation can provide enhanced contrasts in the OSCC mucosa relative to the healthy mucosa due to the heterogeneity of cancerous tissues. Compared with histology, HGM revealed histopathological features including the cytological abnormalities (as shown in Fig. 1), loss of differentiation, interruption of basement membrane, and irregular epithelial stratification in all 10 specimens. In addition to gold standard features, HGM also observed the collagen anomaly and increased actin filament distribution.

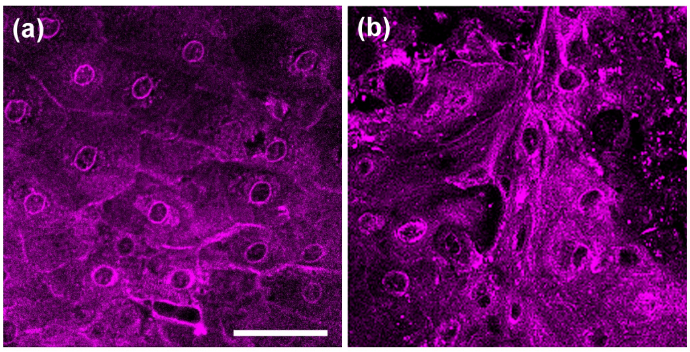

Fig. 1

The keratinocytes of human oral mucosa, including (a) normal tissues and (b) OSCC tissues. *Ex vivo* HGM image of OSCC mucosa shows the cytological abnormalities of keratinocytes. (Scale bar: 50 μm)

Performance of THz fiber-scanning near-field microscopy to diagnose breast tumors

Yuan-Fu Tsai,[1] Hua Chen,[1] Chui-Min Chiu,[1] Tzu-Fang Tseng,[1] Jen-Tang Lu,[1] Wei-Ling Lai,[2] Wen-Jeng Lee,[1,3] Hsin-Yi Huang,[4] and Chi-Kuang Sun,[1,5,6]

1Department of Electrical Engineering and Graduate Institute of Photonics and Optoelectronics, National Taiwan University, Taipei, 10617, Taiwan
2Center of Genomic Medicine, National Taiwan University, Taipei, 10055, Taiwan
3Department of Medical Imaging, National Taiwan University Hospital, Taipei, 10051, Taiwan
4Department of Pathology, National Taiwan University Hospital, Taipei 10051, Taiwan
5Molecular Imaging Center and Graduate Institute of Biomedical Electronics and Bioinformatics, National Taiwan University, Taipei, 10617, Taiwan
6Institute of Physics and Research Center for Applied Sciences, Academia Sinica, Taipei 11529, Taiwan
Email: r99941040@ntu.edu.tw

Based on the statistics of 20 female patients(mean age: 53 years; rang: 36-72 years), we demonstratethat thediagnostic sensitivity and specificityof the room-temperature-operated terahertz(THz)fiber-scanning near-field microscopy in examining sectionsof breast tissuesare as high as100%.The images acquired from the THz transmission-illumination mode can not only clearly distinguish breast tumor tissue from normal tissues(fatty and fibrous tissues) without H&E staining, but also identify the distribution region of breast tumor, which matches well with the identification with pathological examination.Due to its capability to perform quantitative analysis, our study indicates the potential of the THzfiber-scanning near-field microscopy for future automation on breast tumor pathological examinations and for quick definition of the tumor margins during the surgical procedure such as breast-conserving surgery.

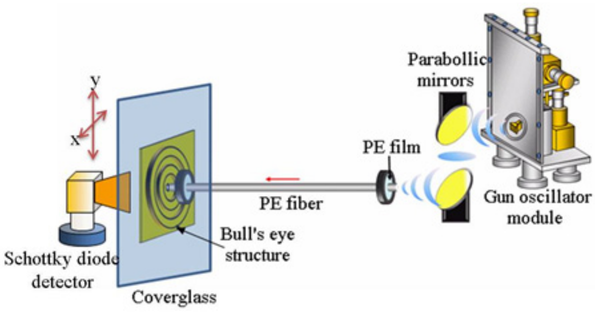

Fig. 1.Schematic of the THz fiber-scanning near-field microscopy.

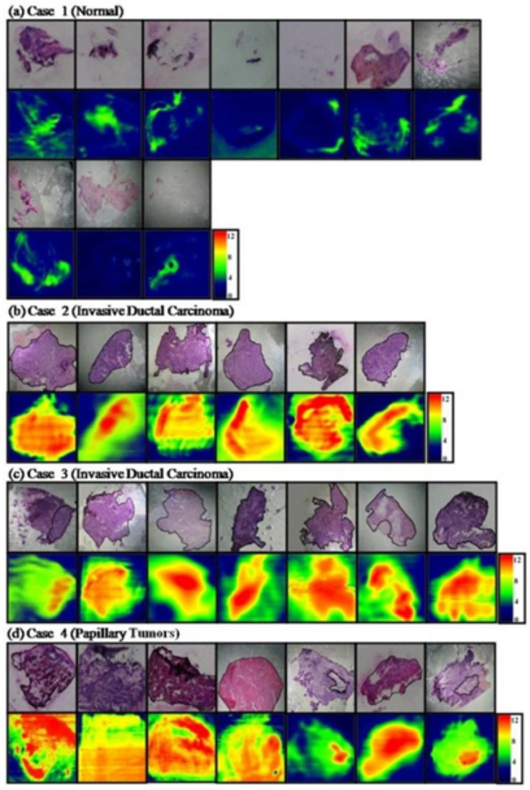

Fig. 2. The THz near-field microscopic images of Case 1-Case 4 and the corresponding pathologic photomicrograph of H&E stained sections.

Remote Destruction of Viral Envelopes through Virus-specific Low-order Microwave-acoustic Resonant Coupling

Jen-Tang Lu,[1*] Tzu-Ming Liu,[2,3] Chin-Jie Huang,[2] Huan-Chun Lin,[4] Chuan-Liang Kao,[4] Hui-Ping Yuan,[5] Yu-Li Lin,[5] Bor-Luen Chiang,[6] Chuan-Fa Chang,[7] Li-Tzu Wang,[7] Jen-Ren Wang,[7] Tang-Nian Luo,[8] Yi-Jan Emery Chen,[8] Hung-Pin Chen,[1] and Chi-Kuang Sun[1,3,8,9]

[1]*Graduate Institute of Photonics and Optoelectronics, National Taiwan University, Taipei 106, Taiwan;*
[2]*Institute of Biomedical Engineering, National Taiwan University, Taipei 106, Taiwan;*
[3]*Molecular Imaging Center and Graduate Institute of Bioelectronics and Bioinformatics, National Taiwan University, Taipei 106, Taiwan;*
[4]*Department of Clinical Laboratory Sciences and Medical Biotechnology, National Taiwan University, Taipei 100, Taiwan;*
[5]*Department of Medical Research, National Taiwan University Hospital, National Taiwan University, Taipei 100, Taiwan;*
[6]*Graduate Institute of Clinical Medicine, National Taiwan University, Taipei 10051, Taiwan;*
[7]*Department of Medical Laboratory Science and Biotechnology, National Cheng Kung University, Tainan 701, Taiwan;*
[8]*Department of Electrical Engineering, National Taiwan University, Taipei 10617, Taiwan;*
[9]*Institute of Physics and Research Center for Applied Science, Academia Sinica, Taipei 115, Taiwan.*
Email: r97941042@ntu.edu.tw and sun@cc.ee.ntu.edu.tw

We demonstrated that the influenza A viruses can be remotely destructed by the resonant illumination of ~13GHz microwaves. The degree of attenuation on the activity of flu viruses can exceed three orders of magnitude at the specific resonant microwave frequency. Validated with a real-time polymer chain reaction (RT-PCR) assay, large amounts of intact viral RNAs are released after illumination. These results evidenced a new mechanical envelope destruction mechanism through microwave-coupled collective vibrations confined in viral particles, whose resonant frequency is determined by its acoustic property and size. We anticipate this non-contact virus-specific method provides a practical and efficient ways to routinely and massively eradicate viruses in public spaces.

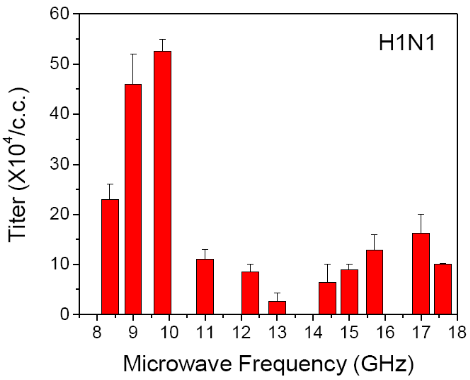

Fig. 1 Inactivation of H1N1 viruses through dipolar coupling of the [SPH, *l*=1] confined acoustic mode to microwaves. A population minimum of active H1N1 viruses occurs around 13GHz.

Differential diagnosis of pigmented skin lesions based on *in vivo* higher-harmonic generation microscopy

Ming-Rung Tsai,[1] **Yi-Hua Liao,**[2] **and Chi-Kuang Sun***[1,3,4]

[1]*Department of Electrical Engineering & Graduate Institute of Photonics and Optoelectronics, National Taiwan University, Taipei 10617, Taiwan*
[2]*Department of Dermatology, National Taiwan University Hospital and National Taiwan University College of Medicine, Taipei, 10051, Taiwan*
[3]*Molecular Imaging Center & Graduate Institute of Biomedical Electronic and Bioinformatics, National Taiwan University, Taipei 10617, Taiwan*
[4]*Institute of Physics & Research Center for Applied Sciences, Academia Sinica, Taipei 11529, Taiwan*
Email: d96941005@ntu.edu.tw

In clinical diagnosis, pigmented lesions are usually diagnosed using the naked eye and are with similar appearance. This may result in misdiagnosis and differential diagnosis of benign versus malignant lesions is thus important to ensure proper prognosis and treatment. Biopsy is currently the gold standard to make the definitive diagnosis, but this medical procedure is invasive and painful for patients. Recently *in vivo* harmonic generation microscopy (HGM) has been reported to have a superior performance on healthy human skin (1,2) and oral mucosa (3). With the noninvasive nature, high penetration capability, and a high resolution, HGM could serve as an ideal virtual biopsy tool for *in vivo*, *in situ*, and immediate differential diagnosis of pigmented skin lesions. It is thus critical to investigate if the endogenous contrast provided by the HGM enough to diagnose the differences between the pigmented skin lesions. In this paper, we summarize our current clinical trial to perform *in vivo* HGM on pigmented skin lesions, including pigmented basal cell carcinoma, seborrheic keratosis, nevocellular nevus and hemangioma. Our clinical trial indicates that HGM is capable of differentiating benign from malignant pigmented skin lesions non-invasively with sensitivity and specificity upto 100% and 94%, respectively, by using surgical biopsy and clinical diagnosis as the gold standard.

(1). Chen, S.-Y.; Wu, H.-Y.; and Sun, C.-K. *J. Biomed. Opt.* **2009**, 14, 060505.
(2). Chen, S.-Y.; Chen, S.-U.; Wu, H.-Y.; Lee, W.-J.; Liao, Y.-H.; Sun, C.-K. *IEEE J. Sel. Top. Quant.* **2010**, 16, 478-492.
(3). Tsai, M.-R.; Chen, S.-Y.; Shieh, D.-B.; Lou, P.-J.; Sun, C.-K. *Biomed. Opt. Exp.* **2011**, 2, 2317–2328.

Miniaturized nonlinear microscopy system with MEMS mirror and mini aspheric lens

Hsiang-Yu Chung[1,4], **Che-Hang Yu**[1], **Cheng-Yung Lin**[2], **Huai-Jen Tsai**[2], **and Chi-Kuang Sun**[1,3,4]

[1]*Graduate Institute of Photonics and Optoelectronics and Department of Electrical Engineering, National Taiwan University, Taipei, 10617, Taiwan*

[2] *Institute of Molecular and Cell Biology, National Taiwan University, Taipei 10617, Taiwan, R.O.C.*

[3]*Research Center for Applied Sciences, Academia Sinica, Taipei, 11529, Taiwan*

[4]*Molecular Imaging Center and Graduate Institute of Biomedical Electronics and Bioinformatics, National Taiwan University, Taipei, 10617, Taiwan*

Phone: +886-2-3393-8928, Fax: +886-2-3366-3614

Email: r99941075@ntu.edu.tw

For clinical use, miniaturized nonlinear microscopy imaging head which has a larger field of view and higher image frame rate is desired. In this paper, we report our design of a miniaturized nonlinear microscopy imaging head which has a much reduced dimension compared with our current system. The design focused on three parts: miniaturized imaging head[4], improved field of view[1], and higher image frame rate[2,3,5,6]. To miniaturize the dimension of the imaging head, we have recently integrated a 1:1 magnification tube lens pair with a millimeter-sized 0.8 NA aspheric lens. This imaging head provides a 170μmX220μm viewing area and up to 30/s frame rate when integrated with a MEMS scanning system. This current system can not only provide a miniaturized size, but also provide a hand-held solution to be integrated with fiber based light source.

(1). Ling Fu, et al.,, "Nonlinear optical endoscopy based on a double-clad photonic crystal fiber and a MEMS mirror," Opt. Express **14**, 1027-1032 (2006)

(2). Hongchun Bao and Min Gu, "A 0.4-mm-diameter probe for nonlinear optical imaging," Opt. Express **17**, 10098-10104 (2009)

(3). Hongchun Bao, John Allen, Robert Pattie, Rod Vance, and Min Gu, "Fast handheld two-photon fluorescence microendoscope with a 475 μm × 475 μm field of view for in vivo imaging," Opt. Lett. **33**, 1333-1335 (2008)

(4). Karsten Bahlmann, Peter T. So, Michael Kirber, Robert Reich, Bernard Kosicki, William McGonagle, and Karl Bellve, "Multifocal multiphoton microscopy (MMM) at a frame rate beyond 600 Hz," Opt. Express **15**, 10991-10998 (2007)

(5). Mon Thiri Myaing, Daniel J. MacDonald, and Xingde Li, "Fiber-optic scanning two-photon fluorescence endoscope," Opt. Lett. **31**, 1076-1078 (2006)

(6). Yicong Wu, Yuxin Leng, Jiefeng Xi, and Xingde Li, "Scanning all-fiber-optic endomicroscopy system for 3D nonlinear optical imaging of biological tissues," Opt. Express **17**, 7907-7915 (2009)

Polarization Anisotropy of Oblique-Aligned ZnO Nanowire Arrays

Cheng-Ying Chen, [1*] **Jun-Han Huang**,[2] **Kun-Yu Lai**,[1] **Yi-Jun Jen**,[3] **Chuan-Pu Liu**,[2] **and Jr-Hau He**[1,]

[1]*Institute of Photonics and Optoelectronics & Department of Electrical Engineering, National Taiwan University, Taipei, 10617 Taiwan*

[2]*Department of Materials Science and Engineering, National Cheng Kung University, Tainan, 701 Taiwan*

[3]*Department of Electro-Optical Engineering, National Taipei University of Technology, Taipei 10608, Taiwan*

Email: d94941017@ntu.edu.tw

ZnO has a direct band gap of 3.37 eV with a large exciton binding energy (60 meV) at room temperature. Due to the strong binding energy of excitons, ZnO are recognized as a promising material for optoelectronic applications in the UV region. One-dimensional nanoscale semiconductor materials, i.e., nanowires and nanorods, have attracted considerable attention due to a ultrahigh surface-to-volume ratio, which results in the tailored electronic and optical properties. However, *c*-axis of the well-aligned ZnO nanowire (/nanorod) arrays are normal to the substrate, so a lot of polarized optical properties are difficult to investigated by adjusting the angle between the direction of electrical field and c-axis(optical axis).

In this work, we demonstrated that a combined method of modified oblique-angle deposition and hydrothermal growth to grow a novel photonic metamaterial based on single crystalline ZnO nanowire arrays (NWAs) with highly oblique angles ($75^{o} – 85^{o}$), exhibiting large artificial in-plane birefringence and optical polarization degree in emission. The giant in-plane birefringence ($\Delta n \cong 0.11$), exceeding by a factor of 10 that of natural quartz. The strong optical anisotropic in emission due to the optical confinement was observed. Unlike the conventional oblique-angle-deposited thin films, the NWAs also showed light emitting ability, leading us to conclude that the oblique-aligned NWAs not only could be applied in passive photonic components, such as optical waveplates and optical isolators, but also can open up important technological applications in polarized light sensing and emission devices.

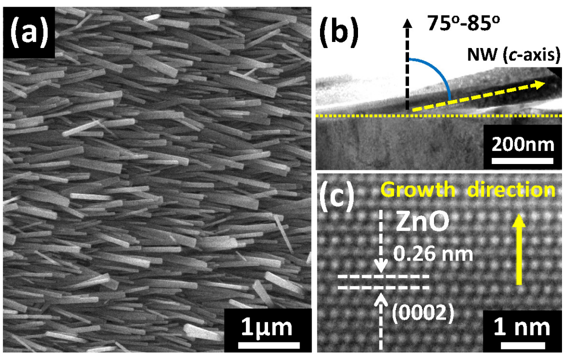

Fig. 1 (a) Top-view SEM image of the oblique-aligned ZnO NWAs. (b) Cross-sectional TEM image of the ZnO NWAs. (c) HRTEM image of a ZnO NW.

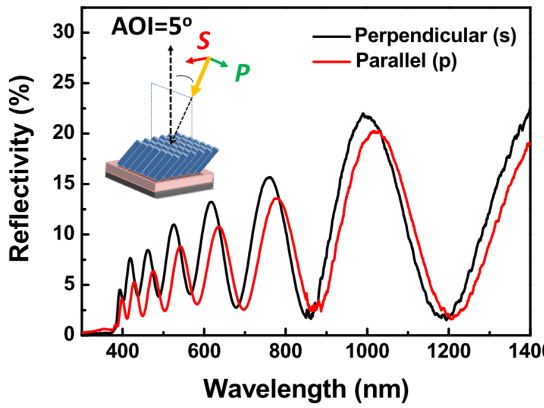

Fig. 2 Reflectivity spectra of the oblique-aligned ZnO NWAs for s- and p-polarization at the AOI of 5º. The plane of incidence is aligned to the orientation of NWs. The s- and p-polarization is perpendicular and parallel to the azimuthal direction of the long axis of oblique-aligned NWAs, respectivel

Plasmonic Toroidal Response of U-shaped Resonant Rings at Optical Frequencies

Yao-Wei Huang[1,*], **Wei Ting Chen**[1], **Pin Chieh Wu**[1,2], **Yuan-Fong Chau**[3], **Nikolay I. Zheludev**[4], **and Din Ping Tsai**[1,2,5,6]

[1]*Graduate Institute of Applied Physics, National Taiwan University, Taipei 106, Taiwan*
[2]*Department of Physics, National Taiwan University, Taipei 106, Taiwan*
[3]*Department of Electronic Engineering, Ching Yun University, Jung-Li 320, Taiwan*
[4]*Optoelectronics Research Centre and Centre for Photonic Metamaterials, University of Southampton, Southampton SO17 1BJ, UK*
[5]*Instrument Technology Research Center, National Applied Research Laboratories, Hsinchu 300, Taiwan*
[6]*Research Center for Applied Sciences, Academia Sinica, Taipei 115, Taiwan*
Email: r99245006@ntu.edu.tw

Toroidal resonance is created by currents flowing on a surface of a doughnut-shaped structure along its meridians first considered by Zel'dovich in 1957[1]. Different from the electric dipole and magnetic dipole, the toroidal multipoles are not included in the traditional multipole expansion[2]. Toroidal metamaterials were first theoretically proposed in 2007[3]. The toroidal response results in strong dependence on the dielectric permittivity, which can make negative index of refraction[3] and rotate polarization state of light[4]. In 2010, the toroidal metamaterials consisted by four three-dimensional resonant split metallic wire loops show toroidal response in microwave region[5].

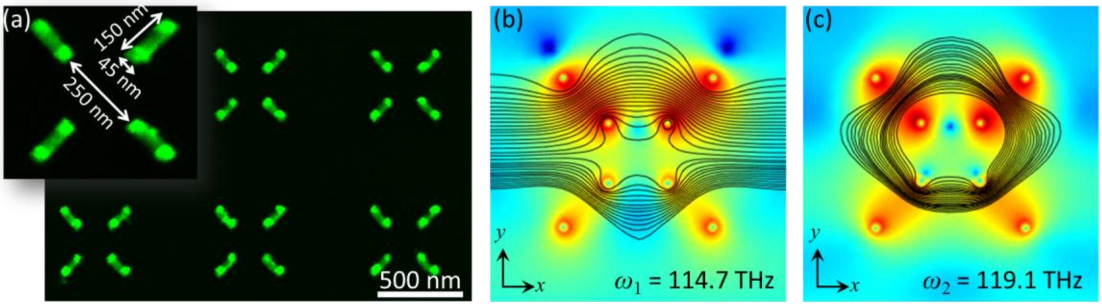

Fig. 1. (a) SEM image of three-dimensional gold resonant split rings. Distribution of magnetic field lines (black streamline) and magnetic energy (color map, in logarithm scale) of magnetic (b) and toroidal (c) resonances.

Simulation results show toroidal and magnetic dipole resonance at frequency ω_1 = 114.7 THz and ω_2 = 119.1 THz. Figures 1(b) and 1(c) show the magnetic energy density and field lines at magnetic and toroidal resonances, respectively. Incident light induced magnetic dipoles point in the same direction produced magnetic resonance. In contrast, four magnetic dipoles form a head-to-tail configuration which concentrates toroidal resonance[7].

(1). Zel'dovich, Ia. B. *Sov. Phys. JETP* **1958**, 6, 1184.
(2). Dubovik, V. M.; Tugushev, V. V. *Phys. Rep.* **1990**, 187, 145.
(3). Marinov, K.; Boardman, A. D.; Fedotov, V. A.; Zheludev N. *N. J. Phys.* **2007**, 9, 324.
(4). Papasimakis, N.; Fedotov, V. A.; Marinov, K.; Zheludev, N. I. *Phys. Rev. Lett.* **2009**, 103, 093901.
(5). Kaelberer, T.; Fedotov, V. A.; Papasimakis, N.; Tsai, D. P.; Zheludev, N. I. *Science* **2010**, 330, 1510-1512.
(6). Huang, Y.-W.; Chen, W. T.; Wu, P. C.; Fedotov, V.; Savinov, V.; Ho, Y. Z.; Chau, Y.-F.; Zheludev, N. I.; Tsai, D. P. *Opt. Express* **2012**, in press.

Electroluminescence of Si Quantum Dots Embedded SiN_x/SiO_x Superlattice

Yung-Hsiang Lin and **Gong-Ru Lin**

Institute of Photonics and Optoelectronics& Department of Electrical Engineering, National Taiwan University
Email: grlin@ntu.edu.tw

The Si quantum dots (Si-QDs) embedded in Si incorporated matrix have emerged to provide intensive visible photoluminescence (PL) and electroluminescence (EL) due to the quantum confinement effect. In comparison with Si-QDs embedded single layer, Si multilayer can promote the precise control on the size distribution and the volume density of Si-QDs. Carriers are facilitated to inject into Si-QDs to achieve large optical emission based on Fowler-Nordheim (F-N) tunneling effect. In this work, the PL/EL, and V-I/P-I characteristics of Si-QDs embedded 20-pair SiN_x/SiO_x stacked superlattice are demonstrated. The SiO_x film is typically a matrix for hosting Si-QDs, however, the electron transportation can be improved by adding the sandwiched SiN_x layers due to the lower tunneling barrier. In experiment, the SiN_x/SiO_x multilayer is deposited with SiH_4/NH_3 and SiH_4/N_2O at 350°C, the thickness of the SiN_x and SiO_x layers of 5 and 10 nm after annealing at 1050°C for 30 min are determined by using transmission electron microscopy (TEM). The volume density of Si-QDs in the SiN_x layer is larger than that in the SiO_x layer due to nitrogen ions are less reactant than oxygen ions, such a nonstoichiometric facilitates the stable Si-SiN_x interfaces.

The PL is performed under a He-Cd laser at 325 nm and is analyzed in a spectrometer combining monochromator and photomultiplier tube. The PL peaks of the as-grown stacked SiN_x/SiO_x multilayer at 410 nm and 530 nm are attributed to the neutral oxygen vacancy (NOV) defect and the nitrogen related defect (N_4^+, N_2^0). After annealing, the PL peak induced by nitrogen related defect is shifted to 519 nm and the other peak at 610 nm caused by Si-QD precipitation appears with enhanced intensity by three times, the corresponding diameter of Si-QD is about 2.9 nm. The results are demonstrated in Fig. 1. Afterwards, the ITO/SiN_x/SiO_x multilayer /p-type MOSLED is fabricated to investigate its EL characteristic. Two EL peaks at 435 nm and 570 nm are observed. The blue shift of the EL peak (570 nm) in comparison with the PL peak (610 nm) may result from the injection of carriers into small-size Si-QDs (Fig. 1). With the current increasing from 6 to 30 μA, the EL intensity (570 nm) linearly enlarges by 5 times without peak shift. From the V-I and P-I analysis, the turn-on voltage of the MOSLED is 200V with the P-I slope of 0.2 μW/A (Fig. 2). Such a high turn-on voltage is caused by the total thickness of 300 nm for the stacked multi-layer. The internal quantum efficiency, external quantum efficiency and the power conversion efficiency are determined as 1.8×10^{-4}, 8.98×10^{-5} and 10^{-6}. In comparison with SiO_x/SiO_2 multilayer structure, the SiN_x/SiO_x based MOSLED benefits from high volume density of Si-QDs, low carrier-tunneling barrier to improve the radiative recombination and the emission efficiency.

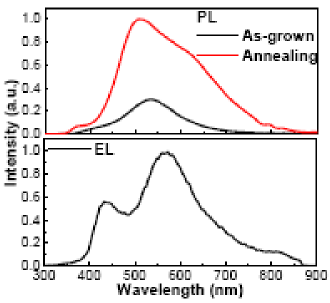

Fig. 1

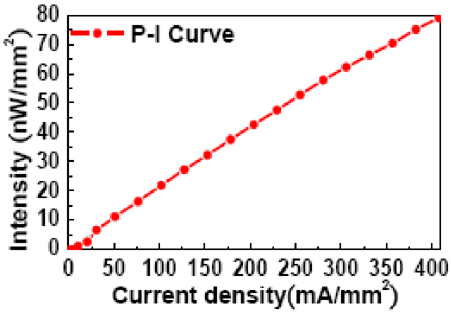

Fig. 2

Tumor detection strategy using ZnO light emitting nano-probes

Yi-Chun Shen[1], Sheng-Chieh Yang[1], Tsung-Lin Yang[2,3,*] , and Jian-Jang Huang[1,4,*]

Department of Chemistry, National Taiwan University, Taipei 106, Taiwan
[1]Graduate Institute of Photonics and Optoelectronics, National Taiwan University, Taipei 106, Taiwan,
[2]Department of Otolaryngology, National Taiwan University Hospital and College of Medicine, National Taiwan University, Taipei 100, Taiwan
[3]Research Center for Developmental Biology and Regenerative Medicine, National Taiwan University, Taipei 100, Taiwan
[4]Department of Electrical Engineering, National Taiwan University, Taipei 106, Taiwan
E-mail: yangtl@ntu.edu.tw, jjhuang@cc.ee.ntu.edu.tw

Since cancer is the primary of top ten causes of death, the detection of tumor have been an important issue. Traditional methods of detecting cancer cells, such as fluorescence, have their limits and can hardly be used for identification during tumor resection. Here we report an alternative tumor detection technology using ZnO nanorods bonded to antibodies as cancer cell probes. Our experiment shows that EGFR (Epidermal growth factor receptor) antibody can be connected to ZnO nanorods and to EGF receptors of SCC (squamous cell carcinoma). The cancer cell can be recognized by the optical microscope with the help of purple light emission from ZnO/EGFR antibody probes. On the other hand, for cells with less expression of EGFR, in our case HS-68, no purple light was observed as the probes were washed-off. From the photoluminescent spectra, the peak intensity ratio between the purple light (from ZnO at the wavelength 377nm) and the green band (from the auto-fluorescence of cells) is much higher with the presence of SCC, as compared with HS68. The ZnO/EGFR antibody probes have the potential to be applied to real time surgery for tumor cell identification. The cancer cells will be excised with the help of purple light emission.

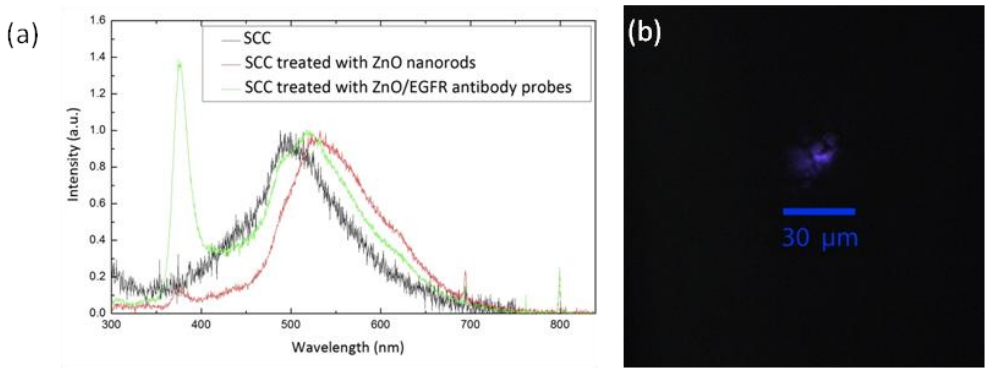

Fig. 1 (a) PL spectra of SCC without/with ZnO NRs/with ZnO/EGFR antibody probes. (b) PL image of SCC with ZnO/EGFR antibody probe filtered by 350-400nm band pass filter.

(1). Gopikrishnan R, Zhang K, Ravichandran P, Baluchamy S, Ramesh V, Biradar S, Ramesh P, Pradhan J, Hall J C, Pradhan A K, and Ramesh G T, Nano-Micro Lett. **2010**, 2, 31-36.
(2). Alaaldin M A, and Catherine J M, J Nanopart Res **2010**, 12, 2313–2333.
(3). Arnida A M, and Ghandehari H, J. Appl. Toxicol **2010**, 30, 212–217.
(4). Zhang W-Q, Lu Y, Zhang T-K, Xu W, Zhang M, and Yu S-H, J. Phys. Chem. C. **2008**, 112, 19872–19877.
(5). Cho E-C, Liu Y, and Xia Y, Angew. Chem **2010**, 122, 2020 –2024

Periodic Si nanowire arrays for broadband light harvesting

<u>Hsin-Ping Wang</u>[1], Kun-Tong Tsai[1,2], Kun-Yu Lai[1], Yi-Ruei Lin[1], Yuh-Lin Wang[2], Jr-Hau He[1]*

[1] *Institute of Photonics and Optoelectronics, National Taiwan University, Taipei, Taiwan*

[2] *Institute of Atomic and Molecular Sciences, Academia Sinica, Taipei, Taiwan*

*jhhe@cc.ee.ntu.edu.tw

Large-area controlled periodic Si nanowire arrays (NWAs) were fabricated by metal-assisted chemical etching, utilizing colloidal lithography or anodic aluminum oxide (AAO) as the patterned mask. The NWAs with desired diameters (fill factors) could be obtained by varying the sizes of the colloidal nanospheres or the pores of AAO templates. The periodicities of NWAs can also be tuned via controlling the pore densities of AAO templates.

Surface reflection on the NWAs was effectively eliminated over broadband regions; i.e., the wavelength-averaged total reflectance is decreased to 10.0 % at the wavelengths of 200-850 nm. The significantly reduced reflectance was also observed for the incident angles up to 60º. These excellent antireflection performances are attributed to light trapping effect and very low effective refractive indices, which can be modified by the fill factor of Si in the NWA layers.

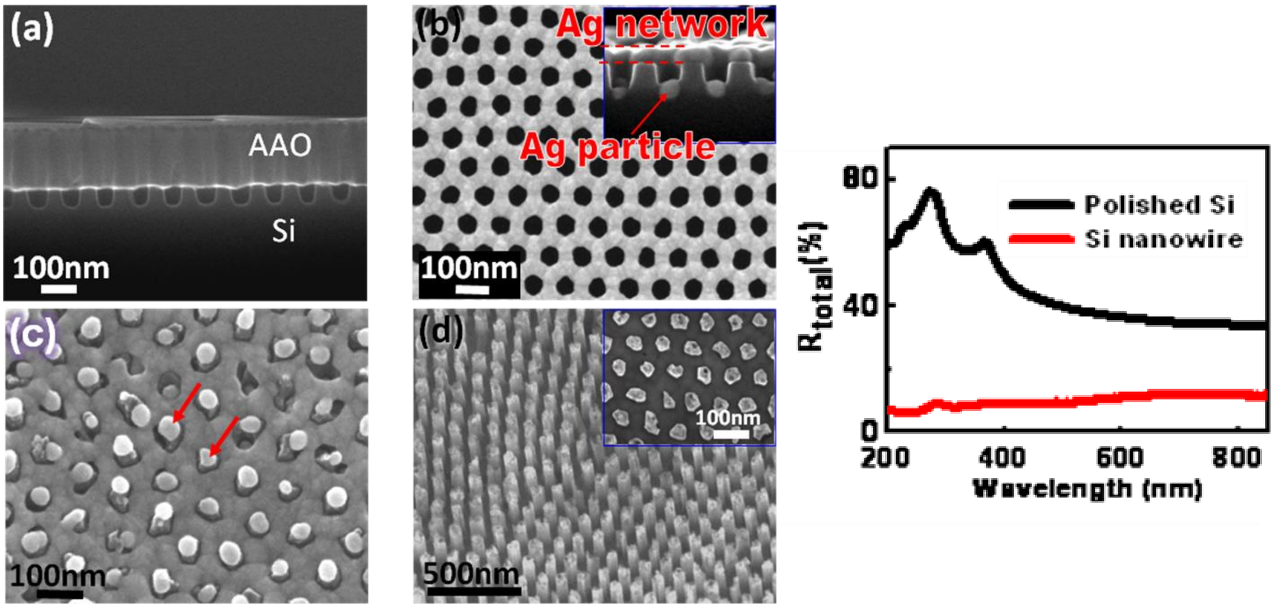

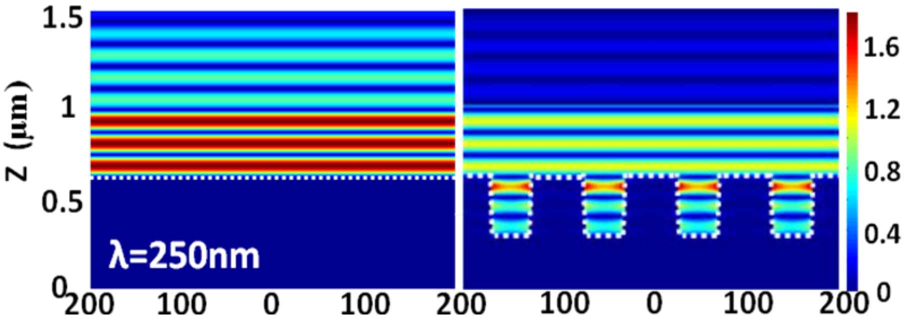

KEYWORDS

Anti-reflection, Subwavelength, Anodic Aluminum Oxide template, Metal-assisted chemical etching, Nanowire Arrays.

Tunable C/Si Composition Induce Si Nanocrystals Self-Assembled in Amorphous Si-rich SiC

Ling-Hsuan Tsai, Tzu-Chieh Lo, and Gong-Ru Lin*

Graduate Institute of Photonics and Optoelectronics, and Department of Electrical Engineering, National Taiwan University, No. 1, Roosevelt Road Sec. 4, Taipei 10617, Taiwan R.O.C.
E-mail: grlin@ntu.edu.tw

Silicon nanocrystals (Si-ncs) self-aggregated in silicon-rich silicon carbide are synthesized by growing with plasma-enhanced chemical vapor deposition on (100)-oriented Si substrate. Under the environment of Argon(Ar)-diluted Silane (SiH_4) and pure methane (CH_4), the substrate temperature and RF power are set as 350 ^oC and 120W, respectively, to provide the Si-rich SiC with changing fluence ratio (R = $[CH_4]/[CH_4]+[SiH_4]$). By tuning the fluence ratio from 50% to 70%, the composition ratio x of Si-rich $Si_{1-x}C_x$ film is varied from 0.27 to 0.34 as characterized by X-ray photoelectron spectroscopy (XPS), which reveals the component of Si_{2p} decreasing from 66.3 to 59.5%, and the component of C_{1s} increasing from 23.9% to 31% to confirm the formation of Si-rich SiC matrix. Annealing of the SiC sample from 650^{o}C to 1050^{o}C at 200^{o}C increment for 30 min induces the very tiny shift on the wavenumber of the crystalline Si (c-Si) related peak due to the precipitation of Si-ncs within the SiC matrix, and the Raman scattering spectra indicate a broadened Raman peak ranging from 410 to 520 cm^{-1} related to the amorphous Si accompanied with the significant enhancement for Si-C bond related peak at 980 cm^{-1}. From the high resolution transmission electron microscopy images, the critical temperature for Si-ncs precipitation is found to be 850^{o}C. The self-assembly of the crystallized Si-ncs with the size of 3±0.5 nm and the volume density of $(3\pm1)\times10^{18}$ (#/cm^3) in Si-rich SiC film with R=70% are observed after annealing at higher temperature.

Silicon carbide (SiC) is an attractive material for fabricating versatile optoelectronic devices owing to its relatively high electrical resistivity and low dielectric constant. The superior optical characteristics of SiC such as high power handling efficiency and the high-absorption coefficient ($\alpha > 10^5$ cm^{-1}) makes it applicable on light-emitting diodes (LEDs) or solar cells. Recently, many researches emphasize on utilizing the non-stoichiometric nano-scale $Si_{1-x}C_x$ film as the host matrix for self-aggregating the Si nanocrystals (Si-ncs) under specific recipe. The Si-rich $Si_{1-x}C_x$ with tunable wide bandgap were successfully synthesized with versatile methods such as Si and SiC co-sputtering, ultrahigh-temperature plasma enhanced chemical vapor deposition (PECVD) with complex fluence mixture of H_2 carried SiH_4 and $Si(CH_3)_3H$ or $Si_2(CH_3)_6H_2$. In this study, we propose the synthesis of non-stoichiometric $Si_{1-x}C_x$ by PECVD with the hydrogen-free mixture gas using Argon(Ar)-diluted Silane (SiH_4) and pure Methane (CH_4). The fluence ratio of R = $[CH_4]/[SiH_4]+[CH_4]$ is detuned to obtain the variable composition ratio of C/Si in Si-rich $Si_{1-x}C_x$. By increasing the annealing temperature, the excessive Si atoms in non-stoichiometric Si-rich $Si_{1-x}C_x$ start to diffuse and to self-aggregate within the $Si_{1-x}C_x$ matrix. The experimental results on growing the non-stoichiometric Si-rich $Si_{1-x}C_x$ films is briefly explained and the data of composition ratio of the Si-rich SiC films measured are provided by using the XPS analysis. A micro-Raman spectroscopic analysis is employed to elucidate the formation of Si-Si and Si-C bonds and the presence of amorphous Silicon (a-Si), Si-nc, and amorphous SiC (a-SiC) phases within the $Si_{1-x}C_x$ films annealed at different temperatures. The quantity of Si-ncs is determined by high-temperature transmission electron microscopy (HRTEM) and their size distribution is fitted by Gaussian function.

TRANSFORMING OF THE NANO-PILLAR FROM THE POROUS ALUMINA MOLD USING NANOIMPRINTING TECHNOLOGY AND APPLICATION TO THE PLASMONIC BIOSENSOR

Akito KITAMURA, Masato SAITO, Keiichiro YAMANAKA, Yoshinori YAMAGUCHI, Eiichi TAMIYA

Department of Applied Physics, Osaka University
2-1 Yamada-oka, Suita, Osaka 565-0871, JAPAN
Phone: +81-6-6879-7839, Fax: +81-6-6879-7840
e-mail: saitomasato@ap.eng.osaka-u.ac.jp

ABSTRACT

Nanoimprinting technology has been remarked in the area of micro-nano-fabrication technology because the nanostructure can be formed in the large area with exceptionally high reproducibility. The porous alumina which has the honeycombed nanostructure, also has been attractive in the nano devices field. Therefore, we think that this substrate is applicable to use as the nanoimprint mold. On the other hand, the plasmonic biosensor has highly applicability to the life science based on its ability of the label free detection. Taking into account all the above mentioned points, we had fabricated the gold-capped nano structures in different sizes by applying the alumina porous substrate as a nano-mold for the nanoimprinting technology, and then applied to the plasmon biosensing. The nano-porous mold was formed by the alumina anodizing processes. The size of porous structures was successfully controlled by varying the applying voltages and anodizing time. Next, these nano-porous structures were transferred to the Cyclo olefin polymer (COP) film surface from the porous mold by the thermal nanoimprinting process. A plasmonic substrate was fabricated by sputtering thin layer of gold on this nano-villus polymer structure and evaluated the response of the refractive index in a variety of solutions. Finally, we carried out the measurement of antigen-antibody reactions as a biosensing model on this plasmonic substrate and successfully detected the molecular specific reactions.

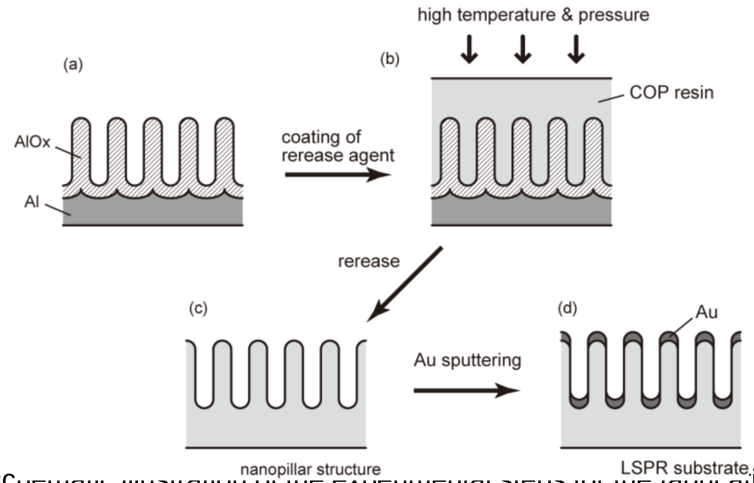

Figure 1. The schematic illustration of the experimental steps for the fabrication of LSPR substrate by nanoimprinting.